ABSTRACT

Title of Dissertation: QUANTUM ENHANCED IMPULSE MEASUREMENTS AND THEIR APPLICATIONS IN SEARCHES FOR DARK MATTER

Sohitri Ghosh
Doctor of Philosophy, 2023

Dissertation Directed by: Professor Jacob Taylor, Professor Peter Shawhan
Department of Physics

Optomechanical systems have enabled a variety of novel sensors that transduce an external force on a mechanical sensor to an optical signal which can be read out through different measurement techniques. Based on recent advances in these sensing technologies, we suggest that heavy dark matter candidates around the Planck mass range could be detected solely through their gravitational interaction. After our understanding of the possibility of direct gravitational detection of dark matter, a coalition of researchers came together to form a lasting collaboration — Windchime — to explore the potential implementation and impact of this approach. With this ultimate goal in mind, the Windchime collaboration is developing the necessary techniques, systems, and experimental apparatus using arrays of optomechanical sensors that operate in the regime of high-bandwidth force detection, i.e., impulse metrology. One of the key challenges in achieving more sensitive measurements is to mitigate the noise which arises due to the fundamental uncertainty principle while trying to precisely measure the variable of interest.

Today's state-of-the-art sensors can be limited by this added noise due to the act of measurement itself. One of the techniques to go beyond this limit involves squeezing of the light used for measurement. The other technique is using backaction evading measurements by estimating quantum non-demolition operators — typically the momentum of a mechanical resonator well above its resonance frequency.

In our work, we have explored various backaction evading techniques based on this principle. In the first part of the thesis, we present the impulse metrology task in the context of gravitational detection of dark matter. In the next part, we present a practical way to achieve backaction evading measurements in the optical domain. In the subsequent part, we analyze the theoretical limits to noise reduction while combining different quantum enhanced readout techniques for these mechanical sensors. In the last part of the thesis, we explore the possibility of a microwave domain readout for maximizing the energy efficiency and noise reduction while having a scalable system for our dark matter detection purpose.

QUANTUM ENHANCED IMPULSE MEASUREMENTS AND THEIR APPLICATIONS IN SEARCHES FOR DARK MATTER

by

Sohitri Ghosh

Dissertation submitted to the Faculty of the Graduate School of the
University of Maryland, College Park in partial fulfillment
of the requirements for the degree of
Doctor of Philosophy
2023

Advisory Committee:
Prof. Peter Shawhan, Chair/Advisor
Prof. Jacob M. Taylor, Co-Chair/Advisor
Dr. Daniel Carney
Prof. Ronald L. Walsworth (Dean's representative)
Prof. Christopher J. Lobb

Acknowledgments

This PhD journey would not have been possible without the support from a lot of people around me. I don't know if I would be able to do justice in acknowledging all the people here in this short span but I will still give it a try!

First and foremost I would like to thank my advisors Prof. Jacob Taylor and Prof. Peter Shawhan. I was hoping to work with Jake even before I started as a graduate student at the University of Maryland and I am so glad that Jake agreed to advise me. I have learned so many things from him and obtained tremendous support in my career goals over the last few years and I am really grateful for this reason. Peter also agreed to be my co-advisor very early on and always helped me in the research projects by steering me towards the right directions and teaching me a lot of things. I am truly indebted to him for the overwhelming support I got over these years.

I would like to especially thank Dr. Daniel Carney. Dan has supervised me from the very beginning of my graduate studies and helped in shaping my research interests which also resulted in the particular topic of this thesis. I am really fortunate to have the chance to be his collaborator and to obtain his support both in and outside of research. I would also like to acknowledge the contribution of the committee members, Prof. Ronald Walsworth and Prof. Christopher Lobb in reviewing my thesis work and supporting my disseration defense.

I owe a lot of gratitude to my current group members Brittany Richman, Jonathan Kunjummen and Gayathrini Premawardhana and also the past members of the group including

Shangjie Guo, Minh Cong Tran, Andrew Glaudell, Chiao-Hsuan Wang and Justyna Zwolak. I would like to especially mention Brittany for her incredible support in our shared project as well as in life in general, Jon for being a wonderful collaborator and friend, and Gaya for helping me in various ways.

My thesis would be incomplete without acknowledging the Windchime collaboration and its members. I have been immensely fortunate to be part of this amazing collaboration based on our dark matter detection proposal and have been enriched by all the conversations I had with the collaboration members both through teleconferences and in-person, which have had direct and fruitful impacts on our ongoing research projects. I would like to especially thank the team at Oak Ridge National Laboratory including Dr. Matthew Feldman, Dr. Seongjin Hong, Dr. Claire Marvinney, Prof. Alberto Marino and Prof. Raphael Pooser for directly collaborating with us on the combined backaction evasion and squeezing work. I would like to also mention Prof. Rafael Lang, Dr. Gerard Higgins and Juehang Qin with whom I have had many constructive conversations about our works.

Broadly I am also grateful to many members at the Joint Quantum Institute (JQI), Joint Center for Quantum Information and Computer Science (QuICS) and the Physics department for many enriching conversations and interactions I had and for the supportive environment they created for everyone. I am also thankful for the help I have received from the administrative staff here especially Melissa Britton, Josiland Chambers and Andrea Svejda throughout these years.

My life here at College Park and USA in general, thousands of kilometers away from my family, would have been impossible without the few friends who were responsible for my well-being for all these years. I would miss all the long drives, hikes and impromptu plans with Arinjoy De, Spandan Pathak, Kishalay Mahato, Arunav Bordoloi, Rajat Roy, Sanchita Pal, Kanika Kalra,

Tamoghna Barik and Shibajyoti Das. I thoroughly enjoyed cooking and chatting with Abu Saleh Musa Patoary, Amitava Banerjee, Aritra Das, Gautam Nambiar and attending numerous house-parties with Naren Manjuanth, Subhayan Sahu, Arushi Bodas, Arghya Sadhukhan, Papia Bera, Xiaozhen Fu, Anshuman Swain, Prakhar Gupta, Riya Samanta, Amit Anand, Prashant Pandey and Girishma Grover. I am also thankful for all the good advices from Aniruddha Bapat, Amit Nag, Soubhik Kumar and Swarnav Banik. My friends from my undergraduate days and some from my school days have been a constant source of motivation and support even though they were living geographically far apart. I would like to thank Ravi Kiran Koorapati, Rajashik Tarafder, Akanksha Singh, Tanmoy Biswas, Sarnava Datta, Shankar Menon, Shouvik Ghorai, Suman Mondal, Payel Mukhopadhyay, Ananya Chakraborty, Shataki Guha, Anusree Gupta, Debadrita Dutta for always supporting me.

Even after this long list, some friends require a special mention. Thanks to Ankita Biswas and Simanti Das for being the pillars of support through all these years. Thanks to Saurav Das, for being a wonderful friend, an amazing roommate and for being so patient with me through all the diffcult times, I can not imagine my life here at UMD without your support. And thanks to Aravind Ravi for being the constant confidant for a full decade and for supporting me through thick and thin.

The last paragraph is dedicated to my family. My grandparents were a constant source of inspiration for me from the very beginning. My cousins and my uncles and aunts have always cheered me on to pursue my dreams. I can not thank them enough. Last but most importantly I want to acknowledge my parents and my sister. Their inspiration is what has shaped my aspirations and their love and support is the reason for me being able to pursue my goals. Thank you for everything!

Table of Contents

List of Figures

Chapter 1: Introduction

1.1 Introduction to Dark Matter Searches

The standard model of particle physics developed over the twentieth century has been extremely successful in describing the fundamental constituents of nature and their interactions. The standard model is a description of three fundamental interactions: strong, weak and electromagnetic. The particle content of the standard model is made up of the elementary particles: leptons and quarks, and the forces are mediated by gauge bosons [3].

Even though the standard model has been able to explain many basic phenomena and predict the elementary particles such as top quark, Higgs boson etc., it has failed to explain a few key cosmological phenomena [4, 5] and many astrophysical observations. The galactic rotation curve [1, 6] is such an observation which traces the orbital speeds of the visible matter in a disc galaxy as a function of the radial distance from the galactic center as in fig. 1.1b. It is seen that the best estimates of the amount of ordinary matter inferred from the matter to luminosity ratios, are always significantly smaller than the inferred gravitational mass as per Newtonian gravity. Another famous example is that of the bullet cluster [2]. As the two clusters collide and move past each other, we observe that the dominant form of visible matter, the intercluster medium, has fused together (inferred from X-ray observations) whereas the gravitating matter inferred by gravitational lensing is well separated. Thus it can be seen that the gravitational contours in these

systems do not match with the spatial center of the visible matter as in fig. 1.1c.

Scientists have pondered over how to possibly explain these observations. One approach scientists took was postulating some modification of Newtonian dynamics (MOND) to explain these observations [7]. Even though still under consideration, it has been somewhat less successful in explaining all the observations like Cosmic Microwave background (CMB) power spectrum, which is a primordial black-body radiation coming from all possible directions [8]. The second approach is the more popular one. Before the era of CMB, photons and matter particles (electrons and nucleus) were strongly coupled to each other as a primordial soup. On the other hand, if there were other forms of gravitating matter that do not interact with light, they will only interact with this primordial soup through gravitational interactions. From the observation of CMB and large scale structure formation, we know that our universe contains matter which doesn't interact with photons (or interacts extremely weakly) but nevertheless gravitates. This matter is called Dark Matter.

For decades scientists have been searching for the candidates which would fit in to this category of matter which makes up about 25% of the energy density of our universe [9]. From various astrophysical probes, the energy density of the dark matter in the solar neighbourhood has been determined to be around 0.3 $\mathrm{GeV/cm^3}$, which is roughly the mass of a proton in every cubic centimeter [10, 11]. The dark matter is distributed over a larger volume compared to the visible matter in a halo like structure which is not co-rotating with our galaxy and the solar system is moving through this halo around the galactic center at a velocity of roughly 220 $\mathrm{km/s}$ [12].

However the exact mass of the dark matter is still unknown to us along with its nature i.e. how it interacts with the visible matter or with itself or other dark matter. Roughly the mass of a dark matter particle can lie anywhere in between 10^{-22} eV (assuming $c = 1$ as in particle

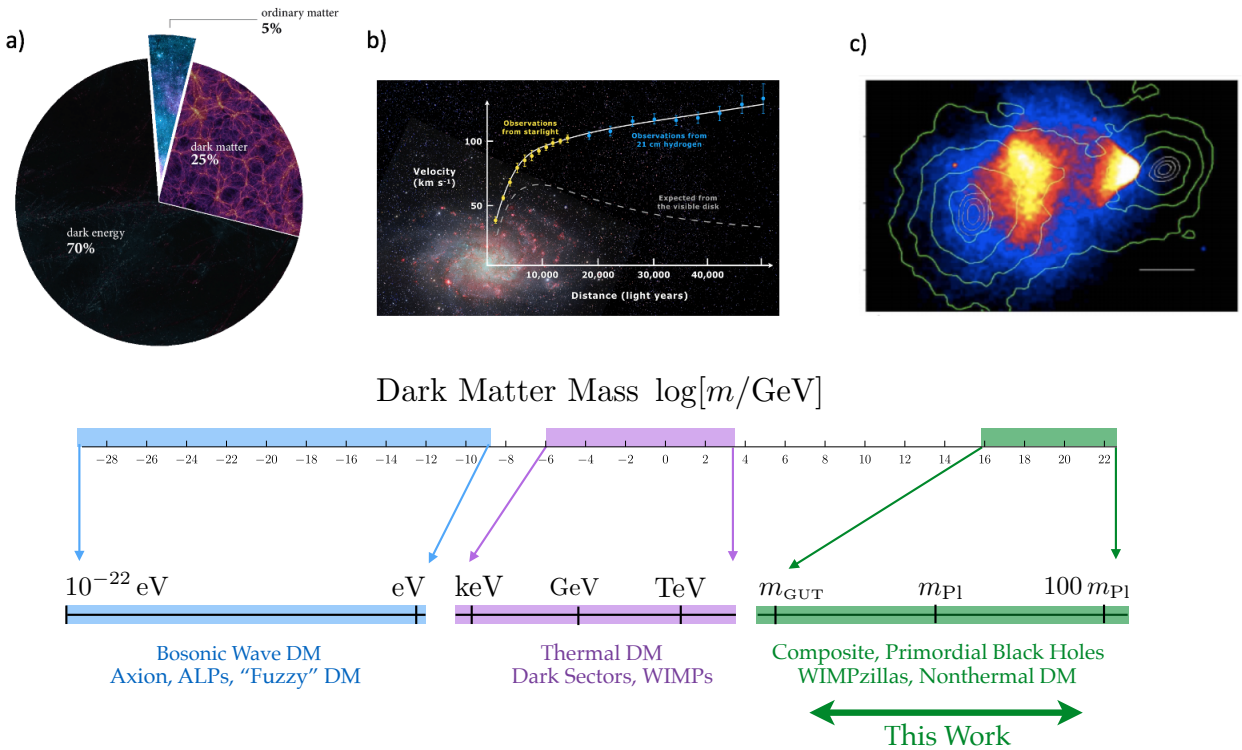

Figure 1.1: Top: a) Energy content of universe (Sources: Max-Planck-Institute for Astrophysics Garching and Pixabay) ; b) Galactic rotation curve [1] ; c) Bullet Cluster [2]; Bottom: Broad classification of dark matter (DM) theory classes according to mass.

physics convention) in the lower range to some 100 solar masses at the higher end as can be seen in fig. 1.1. For masses below $\sim 10^{-22}$ eV, the dark matter (DM) wavelength is too large to fit inside dwarf galaxies [13]. For DM with mass roughly below 10 eV, the number density of DM is sufficiently high that a volume (cube of Compton wavelength) contains more than one DM. The large number of wavefunctions interfere with each other and the resulting configuration can be thought of as a classical superposition of coherent oscillations. On the other hand, above 10 eV, the individual wavefunctions do not interfere with each other and they can be thought of as individual particles. For masses above Planck scale $m_{\mathrm{Pl}} \sim 10^{19}$ GeV , the candidate must also be a composite state, primordial black hole, or an extended object (e.g a topological defect) [14–16].

Scientists have postulated a plethora of models in this huge mass range that dark matter can

reside in. In most of the models, it has been assumed that the dark matter candidates would be able to interact with the visible matter with some form of non-gravitational interaction which we will be able to detect with ultra-sensitive devices. If these particles interact with standard model particles, they can be produced when standard model particles collide with each other at high energies. This particular way of producing dark matter and then detecting them is being pursued at high energy experiment facilities like the Large Hadron Collider (LHC) etc.

To understand the properties of these candidates, researchers have not just looked into the high-energy large-scale experiments, but have also proposed relevant smaller-scale experiments which would be able to probe specific possible interactions of the dark matter candidates with visible matter. Some of the popular models include WIMPs (Weakly Interacting Massive Particles) in the GeV range where we are hoping to observe the weak interaction of these particles with nuclei of noble gas [17, 18]. Another well-motivated candidate being searched for is axions, especially in the $\mu\mathrm{eV} - \mathrm{meV}$ range which could interact with the electromagnetic field to generate some detectable signatures in microwave cavity set-ups [19, 20].

However, until now no dark matter candidate has been directly detected through any laboratory based experiment. Even though researchers have been able to tighten the bounds on these possible interaction strengths between dark matter and visible matter, the particle physics community is yet to discover any direct experimental signature of dark matter.

One characteristic of dark matter which is guaranteed to exist, is its gravitational interaction with the visible matter. Until now, it has been extremely difficult to directly probe the gravitational interaction of any dark matter candidate because of the extremely small strength of gravitational force and for the lack of sufficiently sensitive technology. But recent advancements in quantum sensing technologies have pioneered a way to do ultra-sensitive force measurements.

This has set the stage for a promising new avenue to probe the gravitational interaction with heavy dark matter candidates, which can ultimately lead to a direct detection or a conclusive exclusion of dark matter, in the particular heavy mass regimes as pointed out in fig. 1.1 [21,22].

1.2 Noise Limits to Force Measurements Using Quantum Sensors

Ultra-sensitive force measurement is an ubiquitous problem in physics. Its applications range from research in basic science like looking for particle physics targets or new kinds of forces to more commercial applications with scopes from the tech sector to medical industries. Over the decades, through improvements in devices and technologies associated with it, scientists have been able to achieve an outstanding sensitivity, expressed in terms of attainable force measurement over square root of bandwidth, in the range of $10^{-18} - 10^{-22}\ \mathrm{N}/\sqrt{\mathrm{Hz}}$ [23–27] with the state-of-the-art sensors in existence.

However, sensing an external force suffers from fundamental noise limits because of the act of the measurement on the sensors itself. In most of the force measurement experiments, researchers continuously monitor the position of the system to infer the forces acting on it. In quantum mechanics, Heisenberg's uncertainty principle puts a constraint on how well we can resolve the position of the system if we know the momentum of the system precisely, as they are conjugate variables to each other. Thus we will find that if a non-trivial correlation is not present between these conjugate variables and if the system Hamiltonian is dependent on the variable which is conjugate to the observable we are interested in, we will not be able to measure the desired observable with unbounded precision because the minimal uncertainty principle forbids us from doing so [28].

It is an instructive exercise to work through the example of a free particle Hamiltonian and to look at the evolution of the position and momentum respectively [28]. Let us first assume that we are going to monitor the position of the system. The uncertainty in position and momentum measurements are related by the fundamental Heisenberg's uncertainty relation leading to $\Delta x \Delta p \geq \hbar/2$. The free particle Hamiltonian is $H_{\text{free}} = p^2/2m$. Let us consider that we start with an initial spread in the position state equivalent to Δx and let the system evolve for time Δt. During the evolution time the system evolves under the influence of the unitary operator $U_{\text{free}} = e^{-iH_{\text{free}}\Delta t}$. This leads to the position observable incurring an additional term $|[H, x]| = p\Delta t/m$ during the evolution period. For a subsequent measurement after time Δt, the uncertainty in the position will then acquire an extra term proportional to $\Delta p \Delta t/m$. Thus the uncertainty in momentum gets fed back into the uncertainty of position and increases the overall position uncertainty.

We can optimise this quantity with respect to the initial spread of the system to investigate the limit of precision for this position measurement. If we do so, we would end up with,

$$\Delta x_{\text{SQL}} \geq \sqrt{\hbar \Delta t/m} \tag{1.1}$$

i.e. we would not be able to resolve the position of the free particle better than the quantity $\sqrt{\hbar \Delta t/m}$. This is the standard quantum limit (SQL) benchmark of position measurement as is illustrated in fig. 1.2. If we are continuously monitoring the position of a system and then trying to infer the external forces acting on it, we will end up with an impulse SQL

$$\Delta I_{\text{SQL}} \geq \sqrt{\hbar m/\Delta t}. \tag{1.2}$$

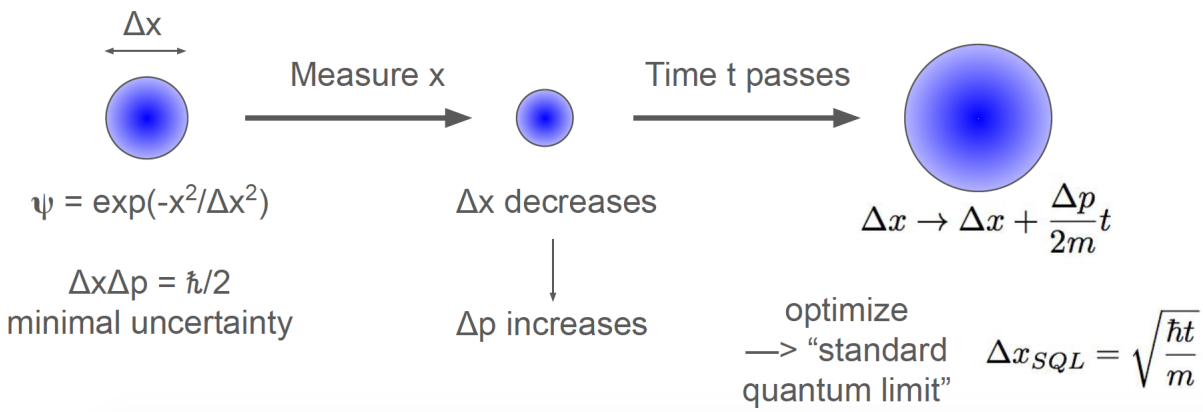

Figure 1.2: Standard Quantum Limit (SQL) description for continuous position measurements where we start from a initial spread in the position as Δx and optimize the subsequent uncertainty with respect to the initial spread to obtain the SQL.

1.3 Noise in Optomechanical Systems

In this section, we will discuss noises in an interferometric measurement in the case of the simplest optomechanical system: a single-sided optical cavity which consists of a fixed partially transparent mirror on one side and a movable perfect mirror on the other side as can be seen in fig. 1.3. The movable mirror acts as the desired mechanical system whereas the fixed mirror serves as the input and output port. The basic principle of operation of these optomechanical systems is the measurement of position dependent phase shift of the probing light through interferometry. In general, a coherent source of light like a laser is used to probe the system. In more detail, the length of the optical cavity is a function of the position of the mirror. Hence the cavity resonance frequency changes as a function of the position of mirror, which results in accumulation of a position dependent phase-shift of the probing light. This phase can be measured at the output port by interfering the output field from the cavity with a local oscillator field of known phase reference. More detailed description of the system can be found in section 2.2 and for reviews

please refer to [29, 30].

1.3.1 Shot Noise and Backaction Noise

Here we will discuss the two sources of noise in an optomechanical system because of the act of measurement [31, 32]. The first one is the shot noise which arises because of the statistical counting error of photons at the output port. This is due to the fluctuations of the probing laser power which gives rise to uncertainty in the number of photons N as big as $\Delta N \sim \sqrt{N}$. For an electromagnetic field, the phase and the photon number follow a minimal uncertainty principle i.e. $\Delta\phi\Delta N \geq 1/2$. So we will not be able to resolve the phase better than $\Delta\phi \sim 1/\sqrt{N}$ and this is the source of shot noise. We note that this noise decreases with increase in power i.e. number of photons as we should expect in case of any kind of statistical error.

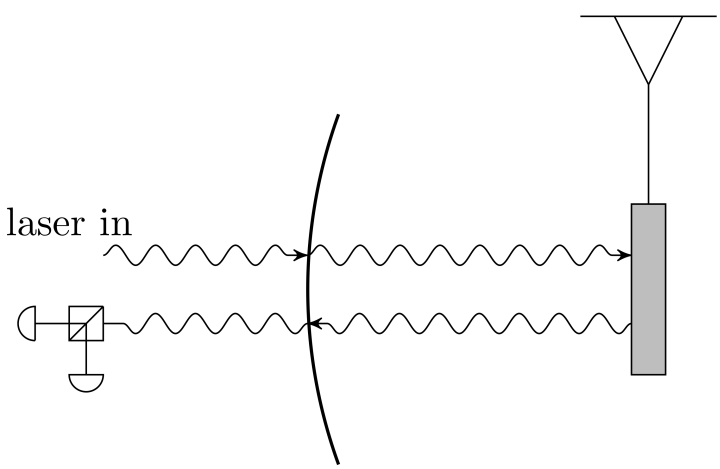

Figure 1.3: Schematic of a single-sided cavity optomechanics experiment. The cavity is driven by a laser from outside. The light picks up a phase $\phi \propto x(t)$ proportional to the position of the moving end mirror, which is then read out through an interferometer after the light exits the cavity.

On the other hand, the random fluctuations in the probing laser power generate random

momentum kicks onto the mechanical system. This gives rise to radiation force noise or backaction noise on the system. This effect is directly proportional to the number of photons in the probing light and hence it increases with an increase in power. Now we can see that these two sources of noise have opposite kinds of dependence on the power of the probing light, hence a balance can be struck between them by optimising the laser power which gives rise to the standard quantum limit (SQL) benchmark in the optomechanical measurement as shown in fig 1.4.

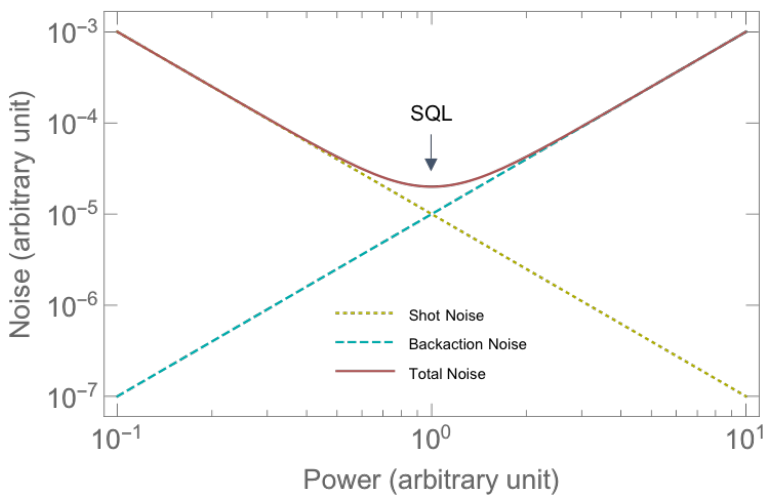

Figure 1.4: Figure depicting the dependence of shot noise and backaction noise on power (both axes plotted in arbitrary units). Also represented here is the Standard Quantum Limit (SQL) noise floor.

We can now briefly discuss how the SQL benchmark in the interferometric measurement relates directly to the SQL discussed in the context of position measurement of a free particle. If we are measuring a position dependent phase shift in an optomechanical system interferometrically, then the position uncertainty relates to the phase uncertainty mentioned above as [31],

$$\begin{aligned}\Delta x_{\text{shot}} &\sim \Delta\phi \frac{c}{2n\omega} \\ &\sim \frac{c}{2n\omega\sqrt{N}},\end{aligned} \tag{1.3}$$

where the ω is the angular frequency of light, c is the speed of light and n is the number of reflections which determines the path length. On the other hand, because of backaction noise, the momentum uncertainty takes a form $\Delta p \sim 2\hbar\omega n\sqrt{N}/c$, which leads to the following form of position uncertainty in subsequent measurements,

$$\begin{aligned}\Delta x_{\text{BA}} &\sim \Delta p \frac{\Delta t}{2m} \\ &\sim \frac{\hbar\omega n \Delta t}{mc}\sqrt{N}.\end{aligned} \tag{1.4}$$

Now we can optimize the sum of these two noises with respect to the number of photons. If we substitute back the optimized power in the expression of Δx, we will obtain an optimal value of the initial spread in position leading to $\Delta x_{\text{opt}} \sim \sqrt{\hbar\Delta t/m}$ which gives us back the position measurement SQL discussed in the previous section.

1.4 Quantum Noise Reduction

The good news is that the standard quantum limit benchmark mentioned in the previous section can be circumvented with some ingenious techniques. The first point to be noted is that we did not assume any non-trivial correlation between the conjugate quadratures when we derived this limit in the last section. Here we will see how introducing correlations between the

quadratures of the probing light and then measuring the appropriate quadrature, helps in reducing the overall measurement-added noises for these systems.

1.4.1 Backaction Evasion

The measurement probes act back on the systems being measured which gives rise to the backaction (BA) noise, as we have previously discussed. Backaction Evasion is a particular resource through which we can negate or substantially reduce the backaction noise from measurements. One of the ways to evade backaction noise is measuring a quantum non-demolition (QND) variable like that of momentum of a free particle as we will discuss in detail in the next section. Even in absence of a QND variable sensing protocol, we can measure an appropriate combination of quadratures at the output port to get rid of the backaction noise arising from the radiation pressure force. Alternatively we can build a device where the probing light has the opportunity to interact with the oscillator from opposite sides, to make the net effect of the random momentum kicks onto the oscillator sum up close to zero, thus nullifying the effect of backaction noise. In Chapter 4 and 5 we will discuss such devices where because of the optimised designs of the systems and readout techniques, we can evade the backaction noise in the optomechanical measurements.

1.4.2 Quantum Non-demolition Measurements

The essence of quantum non-demolition (QND) measurement lies in being able to measure an observable repeatedly without feeding back noise to the system from the conjugate quadrature [28, 33]. This means if we only care about one particular observable of the system and it is a

QND variable, then we will be able to measure this observable precisely repeatedly over time without any additional error being introduced due to the measurement itself. Mathematically, if a variable Z is a QND variable, then it must commute with the system Hamiltonian as $[H, Z] = 0$, so that the observable dynamics remains unaffected during the evolution of the system.

In a previous section 1.2, we observed how position of the system accumulates additional noise during the evolution of the system as it does not commute with the free particle Hamiltonian. On the contrary, if we start our measurement with monitoring the momentum of the system which has an initial spread of Δp, then during a subsequent measurement after time Δt, it will not suffer any additional uncertainty fed from position as the momentum observable commutes with the free particle Hamiltonian, $[H, p] = 0$ where $H = p^2/2m$. This leads to the uncertainty in momentum variable staying constant during subsequent measurements. This is an example of a QND measurement of momentum in a free particle system.

We can now address a key objective of our works on noise reduction techniques. If our quantity of interest is the momentum of a system, then we can design the measurement probes in such a way, so that the probes can directly access the momentum or velocity of the system. If this can be satisfied, then the evolution of the system arising from the system-probe interaction in between subsequent measurements, will not lead to an additional noise fed from the position variable of the system. This can effectively give rise to a QND like measurement of the momentum of a mechanical oscillator. Even though a mechanical oscillator has a trapping potential which is dependent on the position variable, we can essentially consider a free particle regime if we are working well above the mechanical resonance frequency. In our works, we show how a velocity/momentum sensing protocol for a mechanical oscillator while considering measurements at much higher frequencies than its natural resonance frequency, leads

to backaction evasion by exploiting the QND structure of the momentum variable.

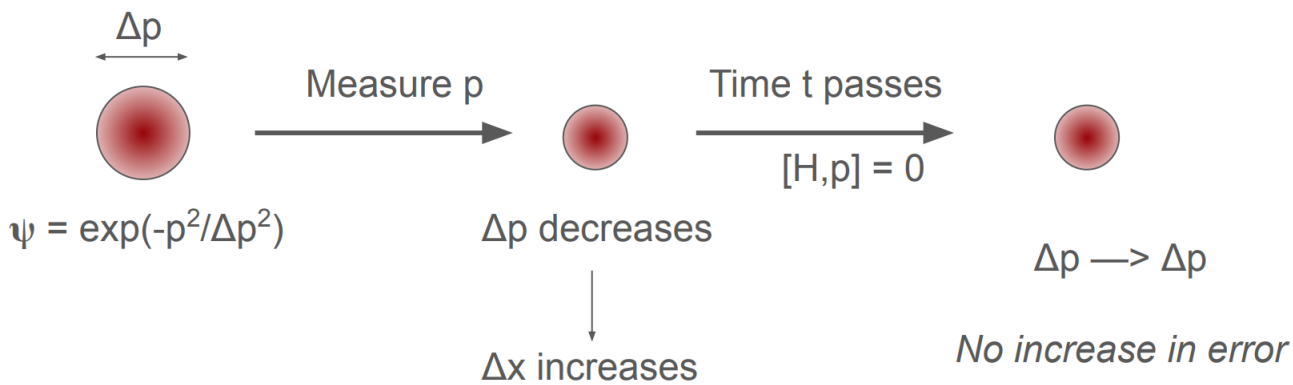

Figure 1.5: Schematics of continuous momentum measurement : the uncertainty in the momentum variable does not increase over subsequent measurements for a free particle.

1.4.3 Squeezing

Previously, we have seen that the phase and number of photons of light obey the minimal uncertainty principle where we can not determine any one of them with unbounded precision. In the quantum mechanical operator description, light can be described by two conjugate quadratures namely the phase (Y) and the amplitude (X) quadratures which follow similar uncertainty relation $\Delta X \Delta Y \geq 1$. For coherent source of light these uncertainties are equally distributed among the two quadratures. However, that need not be the case for every scenario. For squeezed source of light, this uncertainty is unevenly distributed among the two quadratures [32] as described in the fig 1.6. Because of this uneven distribution and non trivial correlation, if we tune the squeezing strength r and squeezing angle ϕ properly and measure in the squeezed direction, we can reduce the overall measurement added noise.

Squeezing has been studied and extensively used in the context of gravitational wave (GW) detection. The first large GW detector to demonstrate squeezing was GEO600 [34]. The

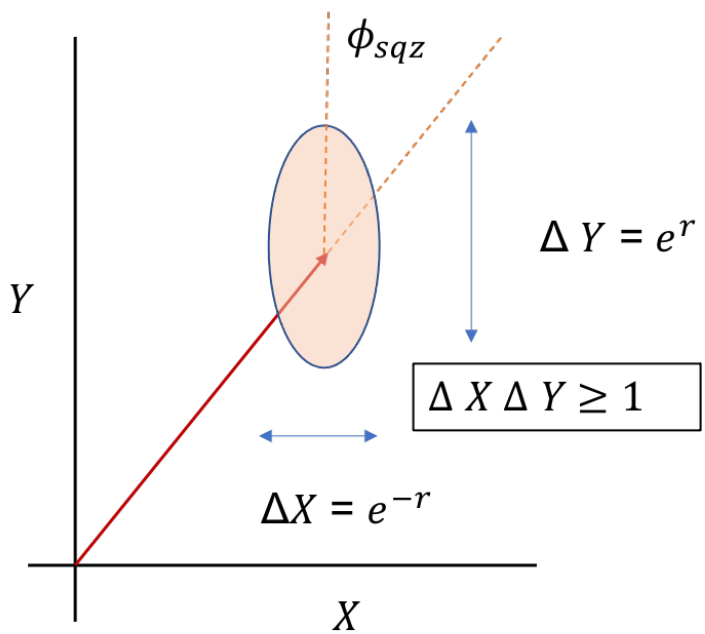

Figure 1.6: Figure depicting the phase space ellipse in the conjugate quadrature space. Here the ellipse is squeezed in the X direction with squeezing strength r and ϕ_{sqz} depicts the angle of squeezing. The area of the ellipse must obey the minimum uncertainty.

advanced LIGO detectors also made use of squeezing as one of the ways to reduce the overall noise floor in order to be sensitive to gravitational waves [35].

1.5 Outline of This Thesis

In this thesis, we discuss how the advancements in quantum technologies aid in ultrasensitive force measurements, especially in the context of searches for dark matter candidates. The introduction gives an overview of the force sensing and noise limits concepts that will be relevant for the subject matter discussed in this thesis. Chapter 2 provides a brief review of the existing works on position measurements with optomechanical systems.

Chapter 3 is an overview of what is meant by impulse metrology and the noise associated with impulse metrology using optomechanical sensors. We also discuss in detail about the

gravitational impulse from the heavy dark matter candidates which inspired us to delve deeper into the noise investigations laid out in this thesis. Here we discuss our proposal for direct dark matter detection solely through their gravitational interaction. We suggest that a three-dimensional array of a large number of quantum-limited mechanical impulse sensors may be capable of detecting the correlated track of motion created by the gravitational interaction of a passing heavy dark matter particle around the Planck mass range. This array setup would also have the capability of providing exquisite directional information and background rejection as the dark matter particle produces a track like signature through this array. The experimental tasks at hand to realize this proposal in terms of scalability, noise reduction and data analysis are enormous but exciting at the same time and the Windchime collaboration is extensively working on making progress toward this ultimate goal.

In chapter 4 based on the dark matter search initiative, we have described how to go beyond the current noise limits in order to be sensitive to such extremely weak interactions. Based upon pioneering works by the gravitational wave community, we find that implementing a continuous momentum measurement rather than a continuous position measurement can help us in reducing the overall noise floor as momentum is a quantum non-demolition variable in the free particle limit. To showcase this, we have worked on a measurement protocol which allows for reduction of added noise from measurement, by coupling an optical field to the momentum of a small mirror in a double-ring optomechanical cavity, through an optimised design of the system. This leads to significant back-action noise evasion, yielding measurement noise below the standard quantum limit in a broadband sense.

In chapter 5, along the same research objective, we have laid out how we can improve the

sensitivities of these optomechanical sensors further. We have explored the theoretical limits to noise reduction while combining the quantum enhanced readout techniques such as squeezing and backaction evasion for these optomechanical sensors. We show that injecting squeezed light indeed improves our power requirement budget. We also find that the noise reduction via squeezing is compatible with the backaction evading mode of noise reduction through velocity sensing and also that backaction evasion dramatically reduces the technical challenges of using squeezed light for broadband force detection, paving the way for combining two different quantum noise reduction techniques in the context of impulse metrology.

In chapter 6, we discuss another approach to the QND measurements in the microwave domain. We have looked into the systems where the motion of a mechanical element can generate a voltage or current in an associated electric circuit which can then be read-out by a parametric cavity. In more detail, we have considered a parametric-cavity based readout system which depends on the electric field or magnetic field generated in the detectors, through which the mechanical motion is resolved by interrogating the changes in transition frequency of this cavity system. We have been able to show that, for an electromechanical sensor, being sensitive to the current generated in the circuit lets us directly access the velocity of the mechanical system whereas we need to sense the voltage in the circuit for magnetomechanical systems to access the velocity. This leads to the matching of the right kind of readout scheme with the right kind of detector in order to maximize the sensitivity.

Chapter 2: Position Measurements in a Single Sided Cavity

Part of the content of this chapter has been published as an appendix in Ghosh et al., Phys. Rev. A 102, 023525 [36] with collaborators Daniel Carney, Peter Shawhan and Jacob M. Taylor. This chapter describes previous works on position measurements with single-sided cavity based on [29, 37].

2.1 Position Measurement Imprecision with Optomechanical Sensors

Consider first a test mass with mass M in the free particle limit. On a regular basis an experimenter interacts with the test mass with a pulse of light, where the light develops a phase shift as a function of the position of the particle. For simplicity, we take the default configuration as some optical (or microwave) cavity with a resonance at a center frequency ω_c and linewidth κ as depicted in fig 2.1. Our detection scheme is to look for a shift of the phase of the pulse due to a length-dependent change in the center frequency.

For small displacements, we define a length scale L that characterizes this change, e.g., $\partial_x \omega_c \approx \omega_c/L$. Then we can estimate the change of phase of the optical pulse with respect to position by noting that in the single mode approximation, narrow-band light of frequency ν has

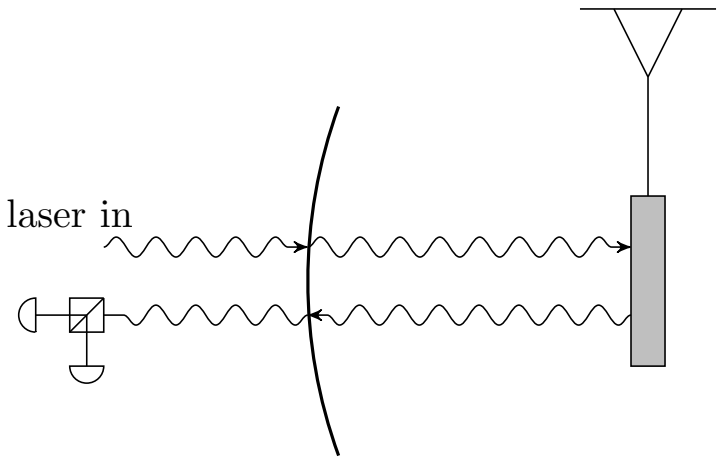

Figure 2.1: Schematic of a single-sided cavity optomechanics experiment. The cavity is driven by a laser from outside. The light picks up a phase $\phi \propto x(t)$ proportional to the mechanical position, which is then read out through an interferometer after the light exits the cavity.

an output field given by [29]

$$a_{\text{out}} = a_{\text{in}} \frac{-i(\nu - \omega_c) - \kappa/2}{-i(\nu - \omega_c) + \kappa/2} \equiv a_{\text{in}} e^{i\phi} \ . \tag{2.1}$$

This result comes from solving for the cavity field using the Heisenberg-Langevin equation and then using the input output relation as depicted below and described in detail in section 2.2

$$\begin{aligned} a_{\text{out}} &= a_{\text{in}} - \sqrt{\kappa} a \\ \dot{a} &= -i\omega_c a - \frac{\kappa}{2} a + \sqrt{\kappa} a_{\text{in}}. \end{aligned} \tag{2.2}$$

The corresponding phase is $\phi = 2\arctan(2(\nu - \omega_c)/\kappa)$. Thus we can see that a small change in ω_c when $|\nu - \omega_c|/\kappa \ll 1$ leads to a phase shift that is proportional to the change in

position δx as approximately:

$$\frac{\delta\phi}{\delta x} \equiv \partial_x \phi \approx 4\frac{\omega_c}{L\kappa} = 4\frac{Q_c}{L} \tag{2.3}$$

where $Q_c = \omega_c/\kappa$ is the optical Q factor.

With this simple analysis, we can ask what happens for estimating this phase shift when using a coherent pulse of light with a finite number of photons, which suffers from shot noise. We expect that a pulse with bandwidth much less than κ and a total of N photons will be able to resolve this phase shift with noise that is given by $1/\sqrt{N}$. The corresponding position measurement imprecision is, in units of length:

$$\Delta_x \approx \frac{L}{4Q_c\sqrt{N}} \tag{2.4}$$

$$\text{or } N = \left(\frac{L}{4\Delta_x Q_c}\right)^2 \tag{2.5}$$

in terms of power. Taking the pulse bandwidth $\lesssim \kappa$, we have a peak power of the pulse $P \sim \kappa\hbar\omega_c N = \hbar\omega_c^2 N/Q_c$, as expected for the enhancement of a phase shift by a cavity.

2.2 Continuous Position Measurements with Optomechanical Sensors

In this section, we present a detailed formalism for detection of forces using a prototypical single-sided optomechanical system implementing a continuous position measurement. Our treatment borrows heavily from [37], and we refer the reader to that review for further details.

The optomechanical system consists of a partially transparent fixed mirror on one side and another movable/suspended perfect mirror on the other side as in figure 2.1, forming a cavity whose frequency is a function of the position $x = x(t)$ of the movable mirror. The cavity mode,

mirror, and their respective baths can be characterized by the total Hamiltonian

$$H_{\text{tot}} = H_{\text{cav}} + H_{\text{mech}} + H_{\text{bath}}. \tag{2.6}$$

Both the cavity mode and mirror are modeled as harmonic oscillators,

$$\begin{aligned} H_{\text{cav}} &= \hbar\omega(x)a^\dagger a \\ H_{\text{mech}} &= \frac{1}{2}m\omega_m^2 x^2 + \frac{p^2}{2m}. \end{aligned} \tag{2.7}$$

Here a denotes the annihilation operator for the optical cavity mode, and ω and ω_m are the resonance frequencies of the cavity and resonator respectively. The cavity resonance frequency $\omega = \omega(x)$ is a function of the length of the cavity and it changes as the mechanical resonator at one end moves. This interaction couples the cavity and the resonator. For small displacements of the mirror, we can Taylor expand the position-dependent cavity

$$\omega(x) = \omega_c \left(1 - \frac{x}{\ell} + \mathcal{O}(x^2)\right), \tag{2.8}$$

where $\omega_c = 2\pi c/\ell$ is the cavity frequency when the mirror is at rest, ℓ being the equilibrium length of the cavity. Using this result, the optomechanical interaction can then be characterized with the following Hamiltonian:

$$H_{\text{int}} = \hbar g_0 \frac{x}{x_0} a^\dagger a. \tag{2.9}$$

The interaction strength here is defined as $g_0 = x_0 \frac{d\omega}{dx} = -x_0\omega_c/\ell$. Here x_0 is an arbitrary length scale which we factor out so that g_0 has units of a frequency. This interaction couples the cavity photons to the mechanical position and is the key to prepare and read out the mechanical motion

through the output light.

Both the cavity and the mechanical system have their own baths. The cavity bath consists of photons which are outside the cavity and can enter and exit through the fixed mirror. The mechanical bath includes degrees of freedom like ambient gas particles which can collide with the mechanics or phonons in the support structure suspending the movable mirror. Both baths consist of a large number of modes. In general, we write the bath Hamiltonian and coupling to the system as

$$\begin{aligned} H_{\text{bath}} &= \Sigma_p \hbar\omega_p A_p^\dagger A_p + \Sigma_p \hbar\nu_p B_p^\dagger B_p \\ &\quad - i\hbar\Sigma_p \left[f_p a^\dagger A_p - f_p^\star a A_p^\dagger \right] - i\hbar\Sigma_p \left[g_p b^\dagger B_p - g_p^\star b B_p^\dagger \right]. \end{aligned} \tag{2.10}$$

Here the A_p, B_p are the cavity and mechanical bath modes, indexed by an arbitrary label p, and ω_p, ν_p are the frequencies of these modes. We have have also introduced the mechanical annihilation operator b, and the coupling constants f_p, g_p.

The bath modes can be integrated out by solving their equations of motion explicitly in terms of their initial conditions and the system variables. Within the Markovian approximation, we can define the bath "input operators" [37, 38]

$$\begin{aligned} A_{\text{in}}(t) &= \frac{1}{\sqrt{2\pi\rho_A}} \Sigma_p e^{-i\omega_p(t-t_0)} A_p(t_0) \\ B_{\text{in}}(t) &= \frac{1}{\sqrt{2\pi\rho_B}} \Sigma_p e^{-i\nu_p(t-t_0)} B_p(t_0), \end{aligned} \tag{2.11}$$

where ρ_A, ρ_B are the densities of states of the baths. Assuming the couplings are constant for the modes of interest $f_p \equiv f, g_p \equiv g$, these quantities are related to the cavity and mechanical energy loss rates via $\kappa = 2\pi f^2 \rho_A, \gamma = 2\pi g^2 \rho_B$ respectively. We then define the input mechanical

force F_{in} in terms of B_{in} and $B_{in}^{\dagger}$. The input force consists of the deterministic signal $F_{\text{sig}}(t)$ plus random Brownian noise, which we model as usual thermal (Johnson-Nyquist) white noise (4.13).

The cavity mode, on the other hand, will be driven by an external laser. In other words, we take the cavity input modes to consist of fluctuations around a classical background. This effectively displaces the cavity operators by $a \to (\alpha + a)e^{-i\omega_L t}$, with ω_L the frequency of the monochromatic laser and $\alpha \propto \sqrt{P/\hbar\omega_L\kappa}$ the drive strength in terms of the laser power P and cavity energy loss rate κ. We move to a frame co-rotating with the drive by applying a unitary transform $U = e^{i\omega_L a^{\dagger} a t}$ to the Hamiltonian. This modifies the cavity Hamiltonian to

$$H_{\text{cav}} = -\hbar\Delta a^{\dagger} a \tag{2.12}$$

where $\Delta = \omega_L - \omega_c$, is the detuning due to the drive. Here we will work on resonance when $\Delta = 0$. For a strong drive, we can linearize the Hamiltonian in the fluctuations,

$$H_{\text{int}} = \hbar g_0 \alpha \frac{x}{x_0}(a + a^{\dagger}) + \hbar g_0 \alpha^2 \frac{x}{x_0}. \tag{2.13}$$

The second term here is just a constant radiation pressure which shifts the equilibrium position of the mechanical resonator. We can re-absorb this into the definition of the constants, thus we drop this term in the following. Defining the quadratures of the cavity to be $\hat{X} = (\hat{a} + \hat{a}^{\dagger})/\sqrt{2}$ and $\hat{Y} = -i(\hat{a} - \hat{a}^{\dagger})/\sqrt{2}$, we have the commutation relation $[\hat{X}, \hat{Y}] = i$, and obtain the effective optomechanical interaction Hamiltonian,

$$H_{\text{int}} = \hbar G x X \tag{2.14}$$

where the effective optomechanical coupling strength is defined as $G = \sqrt{2}g_0\alpha/x_0$ which has the dimension of frequency per length. Here we have chosen a gauge where the coupling is purely between the mechanical position x and optical amplitude quadrature X for notational simplicity.

All told, we can now write down the Heisenberg-Langevin equations of motion for the optical and mechanical quadratures. These read

$$\begin{aligned}
\dot{X} &= -\frac{\kappa}{2}X + \sqrt{\kappa}X_{in} \\
\dot{Y} &= -Gx - \frac{\kappa}{2}Y + \sqrt{\kappa}Y_{in} \\
\dot{p} &= -\hbar GX - \gamma p + F_{in} - m\omega_m^2 x \\
\dot{x} &= \frac{p}{m}.
\end{aligned} \tag{2.15}$$

Here, the input optical quadratures are defined as $X_{\text{in}} = (A_{\text{in}} + A_{\text{in}}^\dagger)/\sqrt{2}, Y_{\text{in}} = -i(A_{\text{in}} - A_{\text{in}}^\dagger)/\sqrt{2}$. These represent the vacuum fluctuations of the light around the classical laser drive, and are taken to satisfy white noise correlation functions of the form

$$\begin{aligned}
\langle X_{in}(t)X_{in}(t')\rangle &= \langle Y_{in}(t)Y_{in}(t')\rangle = \delta(t-t') \\
\langle X_{in}(t)Y_{in}(t')\rangle &= 0.
\end{aligned} \tag{2.16}$$

Note that this assumes the fluctuations are not correlated; these relations are modified in the presence of non-trivial input states, for example squeezed light.

Each input field has a corresponding output field. These are related by the input-output

relations

$$
\begin{aligned}
X_{\text{out}} &= X_{\text{in}} - \sqrt{\kappa} X \\
Y_{\text{out}} &= Y_{\text{in}} - \sqrt{\kappa} Y.
\end{aligned}
\tag{2.17}
$$

The output phase quadrature Y_{out} is what we have experimental access to, via an external homodyne interferometer. Thus, we want to solve for Y_{out} in terms of the various input fields. This is trivial in the frequency domain since the equations of motion are linear. In terms of the mechanical and cavity response functions (4.9), one finds easily that

$$
Y_{\text{out}} = e^{i\phi_c} Y_{\text{in}} + G\chi_c\chi_m \left[F_{\text{in}} - \hbar G \chi_c X_{\text{in}}\right]. \tag{2.18}
$$

Here we defined the "cavity phase shift"

$$
e^{i\phi_c} = 1 - \sqrt{\kappa}\chi_c = \frac{-i\nu - \kappa/2}{-i\nu + \kappa/2}. \tag{2.19}
$$

To estimate the force F on the mechanics given our observed Y_{out}, we can simply divide through with the appropriate coefficient and define an estimator for the force:

$$
F_E = \frac{Y_{out}}{G\chi_c\chi_m}. \tag{2.20}
$$

As we will discuss in chapter 4, the noise in the measurement protocol is characterized by the noise power spectral density (PSD), defined as in (4.12). Here, using (2.18) and the various

noise correlation functions, we obtain

$$N(\nu) = \frac{1}{|G|^2|\chi_c|^2|\chi_m|^2} + N_{BM} + \hbar^2|G|^2|\chi_c|^2. \tag{2.21}$$

The first term here is the shot noise arising from the statistical counting errors of photons. The middle term is the thermal noise. The last term denotes the back-action noise arising from the light randomly pushing the mirror around while probing the system.

Here, we notice that the shot noise term is inversely proportional to G whereas the back-action term is directly proportional to G. We can thus optimize these two terms with respect to the optomechanical coupling strength G which is in turn dependent on the laser power. Note that this procedure is done at some particular, fixed frequency. Differentiating with respect to G one finds the optimum

$$|G_{\text{opt}}|^2 = \frac{1}{\hbar|\chi_c|^2|\chi_m|}. \tag{2.22}$$

For a sinusoidal signal of frequency $1/\tau$ and assuming a small damping coefficient γ in the band of $\nu \gg \omega_m$, the noise spectrum is well approximated by

$$N(1/\tau) \approx \frac{\hbar m}{\tau^2} + N_{BM}. \tag{2.23}$$

The variance in the measured impulse with this measurement protocol would then be given by

$$\Delta p^2_{\text{noise}} = N_{BM}\tau + \frac{\hbar m}{\tau} = N_{BM}\tau(1+\eta^2) \tag{2.24}$$

where $\eta = \sqrt{\frac{\hbar m}{\tau^2 N_{BM}}}$.

Chapter 3: Impulse Metrology and its Application in Dark Matter Searches

Parts of this chapter have been published in Carney, Ghosh, Krnjaic, Taylor, Phys. Rev. D 102, 072003 [21] with collaborators Daniel Carney, Gordan Krnjaic and Jacob M. Taylor. Some of the other content is part of a manuscript in preparation with Jacob M. Taylor and with contributions from the collaborators at the Windchime Project. [1]

3.1 Introduction

The quantum limits to the measurement of the position of an object have a long history, going back to the birth of quantum mechanics. The advent of the concept of gravitational wave detectors like LIGO required researchers to sharpen the mathematics of such measurements and connect it to physical scenarios, leading to the definition of a 'standard quantum limit' [28]. At the same time, researchers realized that there are a variety of ways to go beyond these limits, including the use of entanglement [39–41], squeezing [42, 43], and quantum non-demolition measurements [44–46]. Today, groups around the world have realized that the sensing of forces on masses, typically implemented by measuring their position over time, can yield new insights and bounds on physics beyond the standard model, particularly with respect to dark matter [21, 47–52].

[1] I have specifically contributed to the analysis of the noise limits and signal to noise ratio (SNR) for the purpose of gravitational detection of dark matter and to the writing of the Windchime manuscript in preparation.

In order to measure and bound unknown physics, we must develop the tools for low cost, large-scale systems of mechanical sensors that operate below the standard quantum limit. This means balancing performance and scalability.

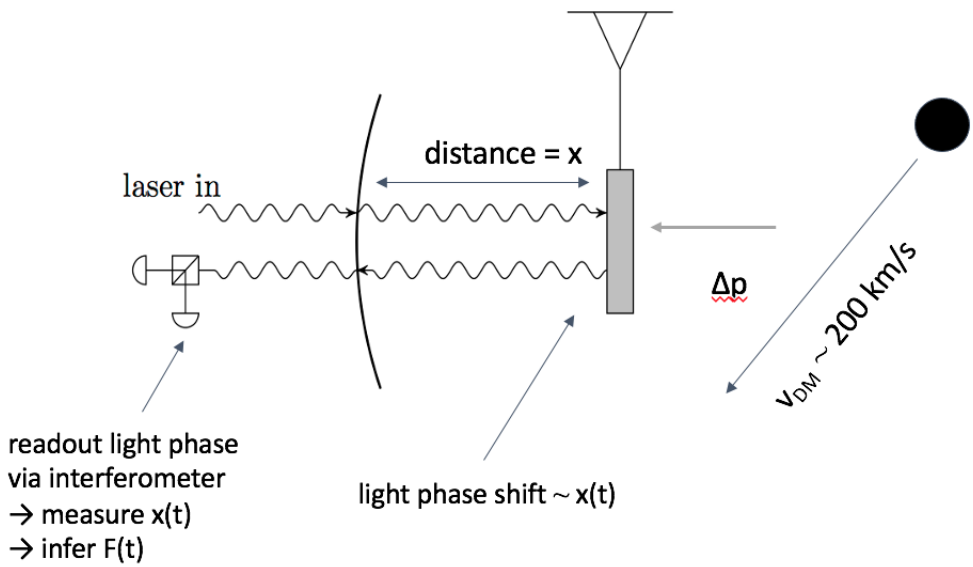

Figure 3.1: Schematic diagram of an optical cavity with a movable mechanical oscillator on one side where the cavity resonance frequency ω_c is set by the wavelength of light. Here we represent how a passing dark matter particle can exert an impulse which can be inferred from monitoring the position of the mechanical oscillator.

3.2 A Toy Model for Impulse Detection

We now turn to our metrology task at hand: looking for a small impulse delivered to a mass. Consider a series of pulsed measurements separated by a time τ of the position of the particle, $x_1, x_2, \ldots$. Working for now in the free particle limit, we get a relationship:

$$x_i = x_{i-1} + v_{i-1}\tau \tag{3.1}$$

$$v_i = v_{i-1} + I_i/M \tag{3.2}$$

where I_i is an impulse delivered just after the previous measurement, v_i is the velocity of the particle and M its mass. The impulses provide a way to account for backaction due to measurements, heating due to interaction with the surrounding bath, and the actual signal desired. This is overly simplistic, but helps us capture our overall goal for understanding.

Inverting the first equation yields $v_{i-1} = \frac{x_i - x_{i-1}}{\tau}$. Thus the double difference gives

$$I_{i-1}/M = v_{i-1} - v_{i-2} = \frac{x_i - x_{i-1}}{\tau} - \frac{x_{i-1} - x_{i-2}}{\tau}. \tag{3.3}$$

That is, we get this impulse by taking the estimate of the second derivative of $x(t)$, which in turn is the difference of the estimates of the velocity at two points in time.

Now we can ask, how well can we estimate the velocity of this mass by monitoring the position over time? One approach is the quantum optics, continuous time measurement approach using techniques of quantum non-demolition measurement [33, 36, 44, 46] and we elaborate on these results in chapter 4.

In this chapter, we first investigate the impulse due to the gravitational interaction with dark matter and then we address the question whether we can we approach thermal limits due to the interaction of the detector with the surrounding bath for such measurements.

3.3 Gravitational Impulse from Dark Matter

Our basic problem is the detection of a passing DM particle via gravity. See figure 3.2 for a diagram of the kinematics. We are interested in the Newtonian gravitational force $\mathbf{F}_N = G_N m_\chi m_d \hat{\mathbf{r}}/r^2$ between a detector of mass m_d and DM particle of mass m_χ. A lab at rest on Earth sees the DM pass by with average "wind speed" $v \approx 220\,\mathrm{km/s}$. Thus the DM imparts momentum

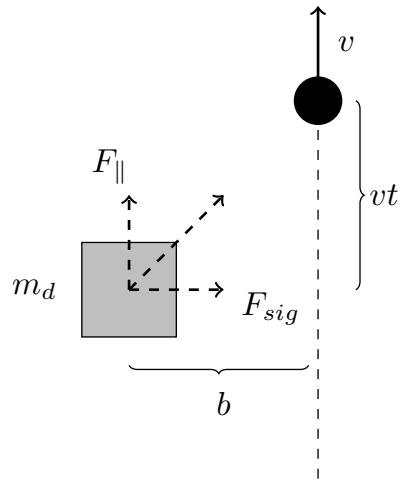

Figure 3.2: Kinematics of the long-range scattering event. A particle passes near the sensor, with impact parameter b and velocity v. This leads to an effective interaction time $\tau \sim b/v$.

to the detector on a very short timescale τ. For a fiducial impact parameter b of approximately a millimeter, we have $\tau \approx b/v \sim 10^{-8}$ s.

The fundamental limitation to force sensing is noise. The total force incident on the sensor is

$$F_{\text{in}}(t) = F_{\text{sig}}(t) + F_{\text{th}}(t) + F_{\text{meas}}(t). \tag{3.4}$$

The first term is the signal. For the purpose of impulse detection which is the integrated force over time, we only need to focus on the transverse component of the force, perpendicular to the dark matter trajectory (see figure 3.2),

$$F_{\text{sig}} = \frac{G_N m_d m_\chi b}{(b^2 + v^2 t^2)^{3/2}}. \tag{3.5}$$

The noise terms $F_{\text{noise}} = F_{\text{th}} + F_{\text{meas}}$ are random variables. The measurement-added noise F_{meas} is a fundamental quantum limitation, and depends on the system observable we probe and how

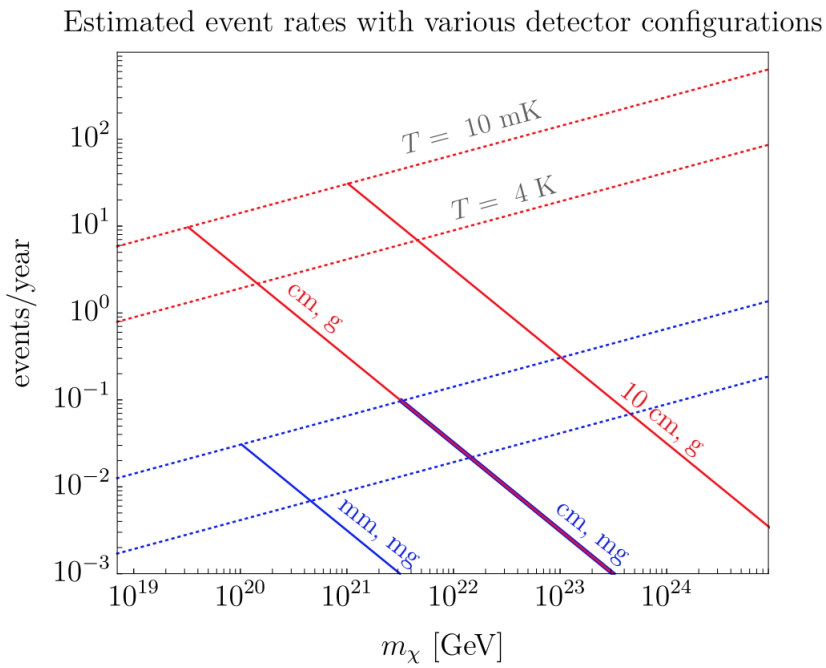

Figure 3.3: Detectable DM event rates, with a variety of detector configurations. Thick lines correspond to number of events per year, assuming all DM particles have mass m_χ. The $1/m_\chi$ falloff in the rate is due purely to number flux (see equation 3.11); by construction, all DM candidates passing through the detector are detected with at least 5σ confidence. Solid lines are labeled by the array lattice spacing (mm, cm, or 10 cm) of the detector and individual sensor masses (milligram in blue or gram in red). Dashed lines labeled by temperature (4 K or 10 mK) demonstrate the increased sensitivity of our scheme with improved environmental isolation. Here we are assuming background gas-limited environmental noise with the same fiducial parameters as in 3.10.

precisely we perform the readout (see [30] for a review). Meanwhile, the thermal noise F_{th} is set by the detector temperature T and the nature of the thermal bath coupling to the detectors, but independent of the measurement readout scheme.

The total impulse delivered to the detector is,

$$I = \int_{-t_{int}/2}^{t_{int}/2} dt\ F_{\text{sig}}(t) \to 2G_N m_d m_\chi \tau / b^2 = 2\overline{F}\tau, \tag{3.6}$$

where t_{int} is the integration time for the measurement, $\overline{F}$ is the average force, and

we assume $t_{int} \geq \tau$ and sufficient incoming velocity so that we can approximate the DM as moving on a straight-line track. The noise is characterized by the variance $\langle \Delta I^2 \rangle = \int\int dt dt' \ \langle F_{\text{noise}}(t) F_{\text{noise}}(t') \rangle$. For stationary noise, this correlation function is proportional to $\delta(t - t')$. Thus the noise grows as a square root in time

$$\Delta I^2 = \alpha t_{int}, \tag{3.7}$$

for some constant α, characteristic of Brownian motion. Since the integrated signal strength grows approximately linearly in t_{int} while the DM is nearby and the noise only grows as $\sqrt{t_{int}}$, an appropriately chosen $t_{int} \approx \tau$ serves to average out the fluctuations caused by the noise. We can further improve the situation by letting a single DM particle interact with $N > 1$ sensors. Assuming the noise is not correlated across these, the standard error decreases like $1/\sqrt{N}$. Thus, in total, the signal-to-noise ratio (SNR) is given by

$$\text{SNR}^2 = \overline{F}^2 N \tau / \alpha, \tag{3.8}$$

taking the measurement integration time $t_{int} \approx \tau$. It is critical that the signal here is the entire, correlated track of moving detectors. This in particular means that our backgrounds –that is, events other than passing DM which likewise trigger a correlated track of displacements– are very different from traditional direct detection experiments. It also means that the signal includes complete directional information.

Our basic result (3.8) can be used to estimate the SNR for any particular detector scheme. Let us assume that thermal noise is dominant over measurement-added noise. We will return

to this key assumption later. For detectors mechanically coupled to a support structure at temperature T, we have $\alpha_{\rm mech} = 4m_d k_B T\gamma$ with γ the detector's mechanical damping rate [30]. For freely-falling detectors, we are limited instead by the latent gas pressure P, which gives $\alpha_{\rm gas} = PA_d\sqrt{m_a k_B T}$, where A_d is the cross-sectional area of each detector and m_a is the mass of the gas atoms [53]. These results are discussed in detail in sections 3.6. Numerically, we thus obtain the following estimates for the SNR:

$$\begin{aligned} \text{SNR}^2 &= \frac{G_N^2 m_\chi^2}{v}\frac{L}{d^4}\frac{m_d}{k_B T\gamma} \\ &\approx 10^{-1}\times\left(\frac{m_\chi}{1\text{ mg}}\right)^2\left(\frac{m_d}{1\text{ mg}}\right)\left(\frac{1\text{ mm}}{d}\right)^4 \end{aligned} \tag{3.9}$$

in the case of detectors mechanically coupled to a support structure, and

$$\begin{aligned} \text{SNR}^2 &= \frac{G_N^2 m_\chi^2}{v}\frac{L}{d^4}\frac{m_d^2}{PA_d\sqrt{m_a k_B T}} \\ &\approx 10^{4}\times\left(\frac{m_\chi}{1\text{ mg}}\right)^2\left(\frac{m_d}{1\text{ mg}}\right)^2\left(\frac{1\text{ mm}}{d}\right)^4, \end{aligned} \tag{3.10}$$

for freely-falling detectors. Here for simplicity we assumed a cubical array of side length L (so that the number of sensors nearest the DM path is $N \sim L/d$) with $L = 1\text{ m}$, and assumed dilution refrigerator temperature $T = 10\text{ mK}$, helium ion-pump vacuum pressures $P = 10^{-10}\text{ Pa}, m_a = 4\text{ amu}$, mechanical damping $\gamma = 10^{-6}\text{ Hz}$, and typical solid density $\rho_{solid} \sim 10\text{ g/cm}^3$ for the detectors.

The signal-to-noise ratios (3.9), (3.10) represent our fundamental detection sensitivities. A DM candidate of mass m_χ passing through a detector will be detected with 5σ confidence if the detector parameters are such that SNR ≥ 5. Clearly, detecting a heavier DM candidate is easier. On the other hand, the number density of DM at high mass is low. The observed local DM energy

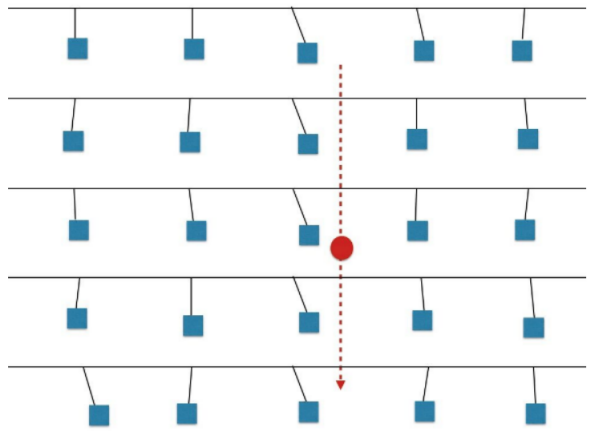

Figure 3.4: Two-dimensional representation of the array of tethered mechanical sensors: a passing DM produces a track through the array

density $\rho_\chi \approx 0.3\ \mathrm{GeV}\,/\,\mathrm{cm}^3$ [11] means that, for a detector of cross-section A_d, the rate of DM passing through the detector is

$$R = \frac{\rho v A_d}{m_\chi} \sim \frac{1}{\mathrm{year}} \left(\frac{m_{\mathrm{Pl}}}{m_\chi}\right) \left(\frac{A_d}{1\,\mathrm{m}^2}\right). \tag{3.11}$$

In figure 3.3, we plot our predicted event rates with a variety of detector geometries. With a billion detectors at the gram scale, Planck-scale ($\sim\ 10^{19}\mathrm{GeV}$) gravitational DM detection is achievable. Reaching heavier masses can be achieved with a sparse, larger array of detectors.

3.4 Windchime

Based on the detection scheme introduced in section 3.3 [21], a collaboration of particle physicists and quantum physicists across many different universities and national laboratories started exploring the idea of gravitational detection of DM [22]. The idea of the detector is based

on the three dimensional array of force sensors introduced in the previous section 3.3 and as depicted in Fig. 3.4. The signal of interest is the correlated track due to the long range interaction with the dark matter particle passing through this array. To reach the desired sensitivity of gravitational detection of Planck-scale DM, the collaboration members are working on different categories of challenges. These include device developments, experimental demonstration of efficient measurement protocols, advancing computational, and statistical analysis techniques and theoretical developments of quantum-enhanced readout techniques along with exploring searchable DM parameter spaces. A prototype set-up is being built as part of this vision. Beside the ultimate Windchime goal of gravitational sensitivity, the same device can also be sensitive to ultralight dark matter, such as through the B–L vector boson interaction [49]. In the near-term the Windchime collaboration expects to demonstrate sensitivities to a wide range of dark matter masses.

3.5 Achieving the Velocity SQL

How does the position SQL described in section 2.1, translate into a velocity SQL? We can simply subtract adjacent position measurements and divide by the time between measurements. Taking the position imprecisions to be uncorrelated, we get

$$\Delta_{v,\mathrm{SQL}} \sim \frac{1}{\tau}\Delta_{x,\mathrm{SQL}} = \sqrt{\frac{\hbar}{M\tau}}. \tag{3.12}$$

This translates our above Windchime numbers into a velocity sensitivity of $\sim 10^{-12}$ m/s if and when we achieve the SQL. We note, however, that increasing τ improves this by $\sqrt{\tau}$. More

generally, taking a sphere of density $\rho \sim 20{,}000$ kg/m^3 and radius R, we get

$$\Delta_{v,\mathrm{SQL}} \sim 10^{-17}\ \mathrm{m/s} \left(\frac{1\ \mathrm{s}}{\tau} \frac{1\ \mathrm{cm}^3}{R^3} \right)^{1/2}. \tag{3.13}$$

To put this in context, we expect the change in velocity due to a dark matter particle with impact parameter b to be approximately [21]

$$v_\infty - v_{-\infty} = \frac{Gm_*}{bv_*} < \frac{Gm_*}{Rv_*} \approx 6 \times 10^{-22}\ \mathrm{m/s} \left(\frac{m_*}{m_{\mathrm{pl}}} \frac{1\ \mathrm{cm}}{R} \right). \tag{3.14}$$

Let us assume that we have access to some degree of backaction evasion. Let us define this improvement by the parameter Q^*, such that $\Delta_{v,\mathrm{BAE}} = \Delta_{v,\mathrm{SQL}}/\sqrt{Q^*}$. With this, we could characterize the signal to noise ratio (SNR) for the Planck scale dark matter as,

$$\begin{aligned} \mathrm{SNR} &= \frac{\Delta_{v,\mathrm{planck}}}{\Delta_{v,\mathrm{SQL}}} \\ &\approx 10^{-5} \left(\frac{\tau}{1\mathrm{s}} \right)^{1/2} \left(\frac{R}{1\mathrm{cm}} \right)^{1/2} \left(\frac{Q^*}{1} \right)^{1/2}. \end{aligned} \tag{3.15}$$

If we were only worried about measurement noise and backaction, we see that the best strategy would be to use a large sphere and a long time, with improvements going as $\sqrt{\tau R}$. If the mass and time scale together, the input power to achieve the SQL level resolution remains the same, so we would not be power limited. However, we do eventually run into limits, with both laser stabilization and mass size. For Planck mass dark matter, getting to an SNR of $O(1)$ would require 1000 seconds between measurements and a radius of 1 meter and a reduction of backaction noise by at least 40 dB if there were no thermal noise.

3.6 Thermal Noise Limits

However, in practice a tethered mass will have a thermal background as well. For the same integration time τ, we expect the thermal noise in velocity to accumulate from a Brownian motion bath as

$$\dot{p} \approx -\gamma p + F_{\mathrm{Th}} \rightarrow \Delta_{v,\mathrm{Th}} \approx \sqrt{\frac{4\gamma k_b T \tau}{M}} \tag{3.16}$$

where γ is the mechanical damping rate, k_b the Boltzmann constant, and T the temperature. Thus the same long integration times that help for reducing the SQL hurt our ability to distinguish our target from a thermal background.

If we define the mechanical $Q_m = \omega_m/\gamma_m$, we find that the thermal noise at 10 mK goes as:

$$\Delta_{v,\mathrm{Th}} \sim 10^{-12}\ \mathrm{m/s}\sqrt{\frac{\omega_m \tau}{Q_m}}\left(\frac{1\ \mathrm{cm}^3}{R^3}\right)^{1/2}. \tag{3.17}$$

Thus we see that short times, long frequencies, and high Qs are all desired for the mechanical system. Note that we are assuming $\tau\omega_m \ll 1$ (otherwise we are not in the 'free particle' limit for a tethered mass).

We would still be limited by an effective white noise due to gas atoms coming off the walls of the cryostat leading to a background impulse noise calculated in section 3.3 [21] for free-falling masses. The background impulse noise due to gas collisions at ultra high vacuum can be characterized as follows,

$$
\begin{aligned}
\Delta_{v,\mathrm{gas}} &\approx \left[\frac{PA_d\sqrt{m_{\mathrm{gas}}k_bT}}{M^2}\tau\right]^{1/2} \\
&\approx 10^{-21.5}\ \mathrm{m/s}\left(\frac{P}{10^{-15}\ \mathrm{Pa}}\right)^{1/2}\left(\frac{T}{1\ \mathrm{K}}\right)^{1/4}\left(\frac{\tau}{1\ \mathrm{s}}\right)^{1/2}\left(\frac{1\ \mathrm{cm}}{R}\right)^{1/2}
\end{aligned}
\tag{3.18}
$$

where we analyse the collision of a He atom at $10\ \mathrm{mK}$ with A_d being the cross-section area of each sensor. This is one way to push the numbers using freely falling masses. Thus we can see that if we are not limited by the measurement added noise for a freely falling detector and only experience the noise due to background collision of gas particles, we would be able to achieve the threshold necessary to detect Planck-scale dark matter particles with roughly an $O(1)$ signal to noise ratio.

3.7 Broad-band Measurements

Let us now consider signals which have a broad range in the frequency spectrum like the gravitational impulse signal from dark matter which is almost like an instantaneous interaction. To calculate the signal to noise ratio in these scenarios we will need to integrate the expected noise over a large bandwidth in the frequency space. In this case, we generally have a fixed mechanical resonance frequency and we tune the driving power to achieve the SQL at just one target frequency and then scan over the broad frequency spectrum. Let us now discuss in detail about some of the mathematical descriptions of noise we will use throughout this thesis.

3.7.1 Noise Power Spectral Density

We usually represent the detector sensitivity to these external forces in terms of the noise power spectral density (PSD) which we will introduce here briefly. If we are measuring an observable which gives us the time series of the total force, the force noise PSD is defined as,

$$\begin{aligned} S_{FF}(\nu) &= \int_{-\infty}^{\infty} \langle \hat{F}_T^\dagger(t)\hat{F}_T(t')\rangle \, e^{i\nu(t-t')} dt \\ &= \int_{-\infty}^{\infty} \langle \hat{F}_T^\dagger(\nu)\hat{F}_T(\nu')\rangle \, d\nu'. \end{aligned} \tag{3.19}$$

Our goal is to measure the net impulse delivered to the detector. During an optical measurement we interferometrically read out the output light phase as a time series, and then process this data to infer the impulse. The simplest option would be to consider the observable

$$I(\tau) = \int_0^\tau F(t)dt, \tag{3.20}$$

where τ is some integration time we can choose, and $F(t)$ is estimated from the output phase of light. The noise in this signal is characterized by the variance,

$$\begin{aligned} \langle \Delta I^2(\tau)\rangle &= \int_0^\tau dt \int_0^\tau dt' \, \langle \hat{F}_T^\dagger(t)\hat{F}_T(t')\rangle \\ &= \int_{-\infty}^{\infty} d\nu \frac{4\sin^2(\nu\tau/2)}{\nu^2} S_{FF}(\nu). \end{aligned} \tag{3.21}$$

This equation says that the RMS net impulse $\Delta I(\tau)$ delivered to the device purely by noise is calculable from the force noise PSD.

3.7.2 Signal Processing and Optimal Filter Theory

Suppose we have some observed force signal $F(t)$ as a time series, which we have estimated from our output light. We want to test the hypothesis that there is a signal $F_{\text{sig}}(t)$ of known shape in the data, occurring at some unknown event time t_e. We thus need to use a filter $f(t - t_e)$ ("template") to scan the data through convolution. We define our estimator for the signal

$$O(t_e) = \int f(t_e - t)F(t)dt. \tag{3.22}$$

The noise in this quantity is independent of the event time t_e. Taking $t_e = 0$ for simplicity and using the convolution theorem, we have

$$O(0) = \int f^*(\nu)F(\nu)d\nu. \tag{3.23}$$

The variance is thus

$$\langle \Delta O^2 \rangle \quad = \int |f(\nu)|^2 S_{FF}(\nu)d\nu \tag{3.24}$$

using our definition of the noise PSD $S_{FF}(\nu)$. Thus the signal to noise ratio is

$$\text{SNR}^2 = \frac{|\int f^*(\nu)F_{\text{sig}}(\nu)d\nu|^2}{\int |f(\nu)|^2 S_{FF}(\nu)d\nu}. \tag{3.25}$$

The question is then: given a particular signal $F_{\text{sig}}(\nu)$ and noise PSD $S_{FF}(\nu)$, what is the optimal choice of filtering function $f(\nu)$ which maximizes the signal-to-noise ratio? Let us

redefine the integration variable

$$du = S_{FF}(\nu)d\nu. \tag{3.26}$$

Since $S_{FF}(\nu) > 0$ is positive everywhere, this change of variable is a valid transformation. Using this we can rewrite the SNR as

$$\text{SNR}^2 = \frac{|\int f^*(u)F_{\text{sig}}(u)\frac{d\nu}{du}du|^2}{\int |f(u)|^2 du}. \tag{3.27}$$

We notice that we have an inner product of $f(u)$ with the function $F_{\text{sig}}(u)d\nu/du$. We want to maximize this inner product while keeping the norm of f fixed. This means that the functions are necessarily going to be parallel. Thus the optimal choice is

$$f_{\text{opt}}(u) = F_{\text{sig}}(u)d\nu/du. \tag{3.28}$$

Inverting this back to frequency domain, we have the simple result for the optimal filter

$$f_{\text{opt}}(\nu) = \frac{F_{\text{sig}}(\nu)}{S_{FF}(\nu)}. \tag{3.29}$$

Using this filter, the signal-to-noise ratio is given by

$$\text{SNR}_{\text{opt}} = \int \frac{|F_{\text{sig}}(\nu)|^2}{S_{FF}(\nu)}d\nu. \tag{3.30}$$

3.8 Narrow-band Measurements

For signals which have a narrow or monochromatic frequency characteristic, we can focus on the noise at specific frequencies to maximize the signal to noise ratio. An example of such a monochromatic signal is the sinusoidal force on the mechanical sensors generated due to the $B - L$ vector boson interactions with ultra-light dark matter candidates [50]. Here, the best strategy is to tune the resonance of the mechanical sensors to gain the maximum sensitivity, if we are limited by the measurement-added noise. However, it is practically difficult to search for a monochromatic signal of unknown frequency by tuning into the resonance for every frequency in the search regime. Thus a better pragmatic strategy is to have a fixed mechanical resonance frequency and then adjusting the driving power to achieve the SQL level noise floor at every frequency for optical readout. We can also fix bins of frequencies and try to achieve the SQL for the central frequency of such bins for experimental convenience. We will discuss these strategies and results in detail again in chapter 5.

Chapter 4: Backaction Evading Impulse Measurement with Double Sided Cavity

The content of this chapter has been published in Ghosh et al., Phys. Rev. A 102, 023525 [36] with collaborators Daniel Carney, Peter Shawhan and Jacob M. Taylor [1].

4.1 Introduction

The precision of any measurement is limited by noise. Beyond technical sources of noise such as thermal backgrounds, quantum mechanics imposes a fundamental source of noise: the act of measurement itself can disturb the system being observed. However, the noise added by the measurement depends on how and what we probe, and in some settings can be reduced or even removed by a judicious choice of measurement protocol.

In an optomechanical system such as a laser interferometer, the noise added by measurement can be decomposed into two parts. The first is shot noise, coming from the finite counting statistics of the photons used to probe the mechanical system. The other is measurement back-action noise, which arises because of fluctuations in the radiation pressure of the light [31, 32]. Early on, it was realized that direct momentum measurements could be used to reduce measurement-added noise [28, 45]. In the context of gravitational wave detection,

[1] I have specifically contributed to the mathematical analysis of this system, noise limits and SNR calculations along with writing the manuscript.

Braginsky and Khalili proposed a concrete velocity-meter scheme in 1990 [46], and this idea has recently been revisited [54–59], with a prototype experiment in progress [60]. Other recent work has proposed using a discrete momentum measurement for noise reduction in sensing of forces [61].

Our approach here is to examine the use of continuous momentum measurement to evade back-action noise in the setting of broadband force sensing, i.e., the detection of rapid impulses. For other approaches to back-action evasion, see for example [62–66]. We present a treatment from a purely quantum optics perspective to demonstrate the benefits of a "speedmeter" design for application in a wide variety of sensors beyond gravitational wave detection. The core idea of our scheme is to monitor the momentum of a mechanical system by coherently integrating the discrete time derivative of the position. In the limit of low optical losses, this becomes equivalent to direct momentum measurement. In the ideal setting of a free-falling mirror without dissipation or losses, such a measurement would enable a complete elimination of all measurement-added noise, since one can further eliminate shot noise by ramping up the probe laser power. To examine imperfections and experimental challenges, we study a practical implementation using a pair of ring cavities, including loss and mechanical noise, which still allows for significant reduction of measurement-added noise.

The detection of rapid, small impulses is ubiquitous in physics, and these ideas should have broad applicability. In metrology, our broadband approach for optomechanical sensing enables applications such as detection of individual low-energy photons or gas collisions with a mechanical element, which would enable quantum noise-limited pressure calibrations [67–72] and force sensing [73–77]. In particle physics, low-threshold detection of energy deposition is of crucial importance in many contexts, for example the detection of light dark matter candidates

[78–81] and astrophysical neutrinos [82–85]. A concrete application which drove this work is the detection of tiny gravitational forces generated by transient dark matter particles [21], and this example is studied in detail in section 4.3.2.

4.2 Continuous Momentum Measurement

We begin with a conceptual outline of the advantages that momentum sensing can provide over position sensing in the context of short signals. Consider the classic argument for the "standard quantum limit" (SQL) in a position measurement [31, 32]. By measuring the system's position, we reduce the position uncertainty Δx while increasing its momentum uncertainty Δp. Assuming the system Hamiltonian is essentially free between measurements, this state will spread to an uncertainty $\Delta x' = \Delta x + \tau \Delta p/m$ after a short time τ. Thus, a subsequent measurement of the system will suffer this increased uncertainty. One could try to probe the system with more measurements (decrease the shot noise), but this will increase the momentum spread Δp (increase the back-action). Position measurement then involves a fundamental trade-off between these two effects; the optimization leads to the SQL uncertainty $\Delta x^2_{SQL} = \hbar\tau/m$.

Momentum measurement, on the other hand, does not suffer from this competition. If we first measure the momentum of the system, this will decrease the momentum uncertainty Δp. The subsequent free evolution of the system will then preserve this uncertainty, since $[H, p] = 0$. One can therefore monitor the momentum with arbitrarily low noise by increasing the rate or strength of these momentum measurements. This represents the "quantum non-demolition" nature of the momentum measurement [45]. If the measuring apparatus is not truly free but has an external potential, for example a harmonic trap, the non-demolition behavior should hold as long as we

perform measurements much faster than the internal dynamics of the device.

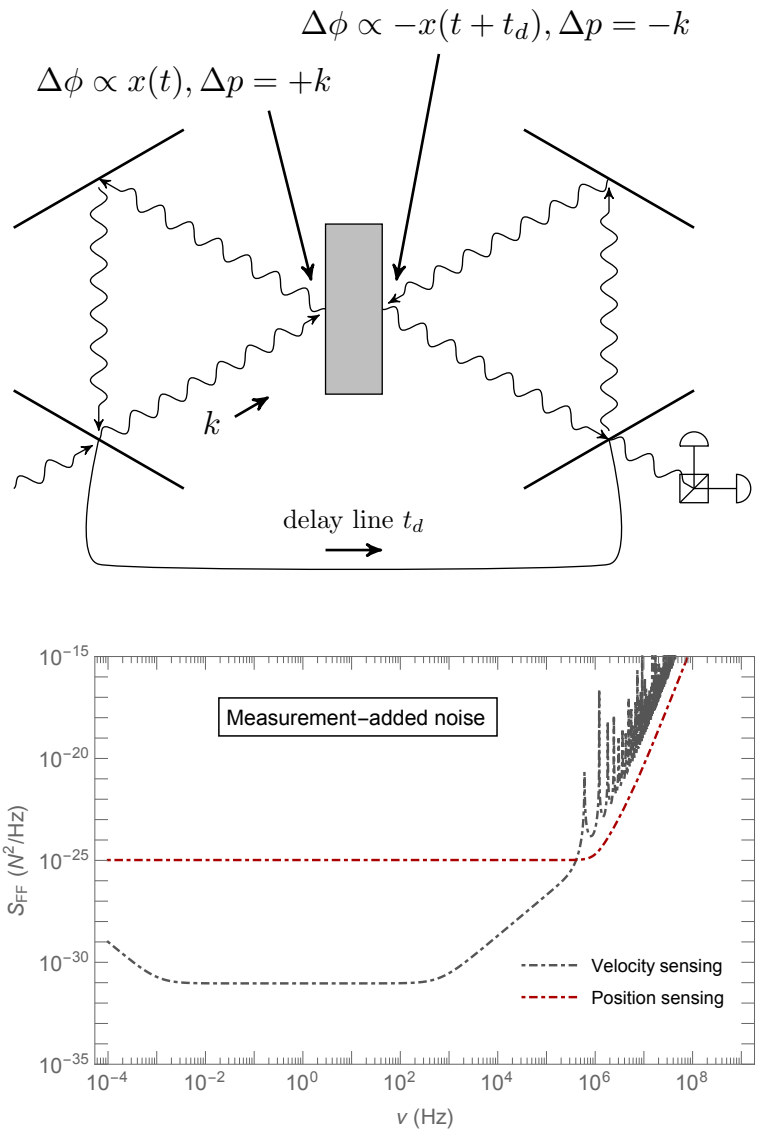

Figure 4.1: Top: Concrete realization of a velocity measurement, using a pair of optical ring cavities separated by a delay line with a suspended mirror as the detector. Each probe photon imparts a momentum $+k$ on the central mirror in the first cavity. After going through a short delay line and into the second cavity, the photon then imparts a momentum $-k$ on the mirror, and is finally read out by an interferometer. The net phase picked up by the light is $\Delta\phi \propto x(t) - x(t+t_d) \propto v$. The two impulses cancel and lead to zero net impulse on the mirror, which amounts to a back-action evading measurement. Bottom: Quantum measurement-added force noise (shot noise plus back-action) in typical position sensing and velocity sensing protocols. Reduction of the back-action noise in the velocity protocol leads to substantial improvements in force sensitivity over a broad band at low frequencies. See figure 4.2 for detailed explanations of the behavior in this plot as well as the relevant detector parameters.

To illustrate this general idea, we now study a concrete optomechanical realization where two ring cavities share a common mechanical element, a two-sided mirror (see figure 4.1). The light interacts with the shared mirror twice from opposite directions with a short time delay t_d. In the first interaction, the light picks up a phase shift proportional to the mirror position $x(t)$ at the time of interaction t. After being run through an optical delay line and fed into a second cavity, the same light then picks up an additional phase shift $\propto -x(t + t_d)$, the mechanical position at the time of the second interaction. This imprints a discrete estimate of the mechanical velocity onto the phase of the light $\phi \sim x(t) - x(t + t_d)$, which can then be read out directly through an interferometer. The same basic setup was proposed in [46, 58] as a "speedmeter", with the goal of searching for gravitational waves. Here we focus instead on the use of this protocol for direct sensing of small impulses (momentum transfers) on a mechanical element.

From this picture, one can see the microscopic mechanism for evasion of the back-action noise: fluctuations in the laser radiation pressure are equal and opposite between the two subsequent light-mechanical interactions, leading to a total change in the mirror momentum that approaches zero. In a practical setting, this cancellation is limited by optical losses. We now study this model using the tools of quantum optics to understand the roles of imperfections and noise in limiting this system for momentum measurement.

We remark that a short, sharp force applied to the system leads to a breaking of the quantum non-demolition condition. Thus, measuring the effect of a sharp force over a short time would best be done by monitoring the momentum before and after the event, such as a gas molecule hitting the mirror. However, here we show that continuous momentum measurement provides a similar benefit in the free fall limit.

4.2.1 Detector Configuration and Noise

Consider a pair of optical ring cavities which share a common mechanical element, taken to be a harmonic oscillator (e.g. a high-quality mirror suspended as a pendulum) with natural frequency ω_m, used here as a resonator. If we monitor the system much more rapidly than its mechanical frequency, we can approximate the dynamics as those of a freely falling system with $\omega_m \to 0$. While $\omega_m \to 0$ can be achieved by simply dropping the system, keeping a mechanical tether and thus a finite ω_m allows us to track corrections from a confining potential to the quantum non-demolition benefits that we can hope to realize.

The combined optomechanical system formed by the cavities, mechanical resonator, and their baths can be characterized by the Hamiltonian

$$\begin{aligned} H_{\text{tot}} &= H_{\text{cav}} + H_{\text{mech}} + H_{\text{bath}} \\ H_{\text{cav}} &= \hbar\omega a^\dagger a + \hbar\omega' a'^\dagger a' \\ H_{\text{mech}} &= \frac{p^2}{2m} + \frac{1}{2} m\omega_m^2 x^2. \end{aligned} \tag{4.1}$$

Here a and a' denote the annihilation operators for the optical cavities. The frequencies ω and ω' are the resonance frequencies of the cavities. These are functions of the lengths of the cavities, which in turn depend on the mechanical displacement x of the resonator: $\omega = \omega(x), \omega' = \omega'(x)$. For small displacements, we can Taylor expand the frequencies, and obtain

$$\begin{aligned} H_{\text{sys}} = \hbar\omega_c \left(a^\dagger a + a'^\dagger a'\right) + H_{\text{mech}} \\ + \hbar \left(g_0 a^\dagger a + g_0' a'^\dagger a'\right) \frac{x}{x_0}. \end{aligned} \tag{4.2}$$

The first line contains the kinetic terms for the two cavities and the resonator, where we have taken the two cavities to have the same frequency $\omega_c = \omega(0) = \omega'(0)$ when the mirror is at its equilibrium position. The second line encodes the optomechanical coupling with strength $g_0 = x_0 \frac{d\omega}{dx} = -x_0\omega_c/\ell = -g_0'$, where ℓ is the equilibrium length of the cavity and x_0 is a length parameter which transforms the coupling strength to a frequency. The key point is that the two cavity-mechanical couplings differ by a relative minus sign, corresponding to the fact that displacements of the resonator generate opposite frequency shifts in the two cavities.

We now examine the system using the input-operator formalism [38] (see section 2.2 for a review in the case of a single-sided cavity). To understand the measurement procedure, we consider driving the first cavity with a monochromatic laser. This effectively displaces the cavity operators by $a \to (\alpha + a)e^{-i\omega_L t}$, with ω_L the frequency of the monochromatic laser and $\alpha \propto \sqrt{P/\hbar\omega_L\kappa}$ the drive strength in terms of the laser power P and cavity energy loss rate κ. We have factored out the drive-frequency time dependence in the light fluctuations (i.e. we work in the frame co-rotating with the drive). We assume sufficient driving $|\alpha| \gg 1$ so that we can linearize the interaction Hamiltonian around the drive. We choose a gauge such that α is purely real, and lock the laser to provide zero detuning $\Delta = \omega_L - \omega_c = 0$. We then obtain the total Hamiltonian for the system

$$H_{\text{sys}} = H_{\text{mech}} + \hbar G x X - \hbar G' x X'. \tag{4.3}$$

Here $X = (a + a^\dagger)/\sqrt{2}$ and similarly X' are the amplitude quadratures of the cavity modes. The drive enhances the effective optomechanical coupling strength $G = \sqrt{2}\frac{g_0}{x_0}\alpha$ in the first cavity which has the dimension of a frequency per length; in the second cavity, we have $G' =$

$-\sqrt{1-L}G$, where L represents loss of photons as they traverse the delay line. We will justify this shortly [see (4.6)].

The system is subject to dissipation via the bath H_{bath}. The cavity bath consists of the cavity photons leaking through the mirrors and the mechanical bath consists of, at least, ambient gas molecules in the chamber and phonons in any support structure. Tracing out the bath with the input-operator formalism, we can study the evolution of the system in the Heisenberg picture. The equations of motion of the cavities and resonator are

$$\begin{aligned}
\dot{X} &= -\frac{\kappa}{2}X + \sqrt{\kappa}X_{in} \\
\dot{Y} &= -Gx - \frac{\kappa}{2}Y + \sqrt{\kappa}Y_{in} \\
\dot{X}' &= -\frac{\kappa}{2}X' + \sqrt{\kappa}X'_{in} \\
\dot{Y}' &= G'x - \frac{\kappa}{2}Y' + \sqrt{\kappa}Y'_{in} \\
\dot{p} &= -\hbar GX + \hbar G'X' - m\omega_m^2 x - \gamma p + F_{in} \\
\dot{x} &= \frac{p}{m}.
\end{aligned} \tag{4.4}$$

Here, γ is the mechanical energy damping rate, F_{in} is the external force (including noise) incident on the resonator, $Y = -i(a - a^\dagger)/\sqrt{2}$ and similarly Y' are the phase quadratures of the cavities, and $X_{in}, Y_{in}, X'_{in}, Y'_{in}$ represent the vacuum fluctuations of the cavities. These satisfy the white noise correlation functions of the form

$$\langle X_{in}(t)X_{in}(t')\rangle = \langle Y_{in}(t)Y_{in}(t')\rangle \propto \delta(t-t') \tag{4.5}$$

and similarly for the primed correlators. The force noise will be discussed in detail when needed.

Each cavity has both an input and output field associated to it. Ultimately we want to read out the phase quadrature of the second cavity Y'_{out}. The output fields are related to the input fields by the usual input-output relations (again see section 2.2 for a review). Here we also need to model the delay line. Photons traversing the delay line can be lost, so we model the line as a beam splitter with a dimensionless loss coefficient L, leading to the input-output relations

$$\begin{aligned}
X_{\text{out}}(t) &= X_{\text{in}}(t) - \sqrt{\kappa}X(t) \\
Y_{\text{out}}(t) &= Y_{\text{in}}(t) - \sqrt{\kappa}Y(t) \\
X'_{\text{out}}(t) &= X'_{\text{in}}(t) - \sqrt{\kappa}X'(t) \\
Y'_{\text{out}}(t) &= Y'_{\text{in}}(t) - \sqrt{\kappa}Y'(t) \\
X'_{\text{in}}(t) &= \sqrt{1-L}X_{\text{out}}(t-t_d) + \sqrt{L}\tilde{X}_{\text{in}}(t) \\
Y'_{\text{in}}(t) &= \sqrt{1-L}Y_{\text{out}}(t-t_d) + \sqrt{L}\tilde{Y}_{\text{in}}(t).
\end{aligned} \tag{4.6}$$

Here $\tilde{X}_{\text{in}}, \tilde{Y}_{\text{in}}$ are the input noise fields associated with the loss in the delay line, taken again to satisfy the vacuum noise correlations (4.5). The last two equations here justify the relation $G' = -\sqrt{1-L}\,G$ between the two driven coupling strengths.

We are interested in monitoring the external force F_{in} acting on the mechanical system. This force is imprinted onto the mechanical displacement $x(t)$. Working in the frequency domain, we can easily solve the equations of motion (4.4), (4.6) to find the mechanical displacement:

$$x(\nu) = \chi_m(\nu)F_{\text{in}}(\nu) + x_{\text{n}}(\nu), \tag{4.7}$$

where the term due to measurement noise is

$$x_{\rm n} = -\hbar G \chi_m \chi_c \left[\left(1 + (1-L) e^{i(\nu t_d + \phi_c)}\right) X_{\rm in} + \sqrt{L(1-L)} \tilde{X}_{\rm in} \right]. \tag{4.8}$$

Here we defined the cavity and the mechanical response functions and the phase,

$$\chi_c = \frac{\sqrt{\kappa}}{-i\nu + \kappa/2} \qquad \chi_m = \frac{-1}{m(\nu^2 - \omega_m^2 + i\gamma\nu)} \qquad e^{i\phi_c} = 1 - \sqrt{\kappa}\chi_c. \tag{4.9}$$

At very low frequency, $\nu \approx 0$ and with a small amount of loss $L \approx 0$, $G' \to -G$ and $e^{i\phi_c} \to -1$, thus the term proportional to the input noise $X_{\rm in}$ in the position variable vanishes. This amounts to back-action evasion in the low frequency part of the measurement: there is no net force from the fluctuations in the radiation pressure. The noise from the delay loss $\tilde{X}_{in}$ will also be negligible in this limit.

The mechanical displacement is in turn imprinted onto the phase quadrature Y of the light through the optomechanical coupling $H_{\rm int} \sim GxX$. We then read out the output light Y'_{out} from the second cavity, from which we infer the external force F_{in}. The equations of motion (4.4), (4.6) yield the output light phase

$$Y'_{\rm out} = \sqrt{L} e^{i\phi_c} \tilde{Y}_{\rm in} + \sqrt{1-L} e^{i(\nu t_d + 2\phi_c)} Y_{\rm in} + G\sqrt{1-L}\chi_c \left(1 + e^{i(\nu t_d + \phi_c)}\right) x. \tag{4.10}$$

Given the measured output light Y'_{out}, we estimate the force by simply dividing through with the

appropriate coefficient:

$$F_E = \frac{Y'_{out}}{G\sqrt{1-L}\chi_c\chi_m\left(1+e^{i(\nu t_d+\phi_c)}\right)}. \tag{4.11}$$

In order to calculate our sensitivity to various signals, we need the noise in the force estimator. We define the force noise power spectral density (PSD) in the usual way,

$$\langle F_E(\nu)F_E(\nu')\rangle = N(\nu)\delta(\nu+\nu') = S_{FF}(\nu)\delta(\nu+\nu'). \tag{4.12}$$

We will see later how exactly this is used to determine sensitivities, but the intuition is that for a broadband impulse signal, sensitivities are set by an integral of $N(\nu)$ over the relevant frequency band. Let us assume that the input force F_{in} is purely thermal (Johnson-Nyquist) noise, so that

$$\langle F_{in}(t)F_{in}(t')\rangle = N_{BM}\delta(t-t'), \;\; N_{BM} = 4m\gamma K_B T \tag{4.13}$$

with T the temperature of the bath coupled to the resonator. Then the force noise PSD can be computed directly using (4.10), (4.11), (4.12) and the vacuum noise correlation functions (4.5):

$$\begin{aligned} N(\nu) = &\frac{1}{4(1-L)|G|^2|\chi_c|^2|\chi_m|^2\cos^2(\frac{\nu t_d+\phi_c}{2})} \\ &+ N_{BM} + 2\hbar^2|G|^2|\chi_c|^2\left[1-\frac{L}{2}\right. \\ &\left.+\frac{(1-L)}{\nu^2+\kappa^2/4}[\nu\kappa\sin(\nu t_d)+(\nu^2-\kappa^2/4)\cos(\nu t_d)]\right]. \end{aligned} \tag{4.14}$$

The first term here is the shot noise arising from the statistical counting errors of the laser photons. The middle term is the thermal noise. The last term denotes the back-action noise arising from

the light pushing the mirror around while probing the system. At low frequency, the term in the bracket is proportional to $L/2$ and thus the back-action noise vanishes to the lowest order of the loss coefficient. We plot this noise PSD in figure 4.2. For comparison, we present the analogous noise PSD for a standard single-sided cavity force sensor (2.21) in the same figure (see section 2.2 for details).

In order to get some intuition about the noise in this protocol, first consider the high- and low-frequency behavior of the noise PSD (4.14). At arbitrarily low frequencies ν, the noise PSD diverges:

$$N(\nu) \xrightarrow[\nu\to 0]{} \frac{m^2\kappa^3\omega_m^4}{4|G|^2(4+\kappa t_d)^2}\frac{1}{\nu^2} \quad . \tag{4.15}$$

Meanwhile, at very high frequencies we also have a divergence

$$N(\nu) \xrightarrow[\nu\to\infty]{} \frac{m^2}{|G|^2\kappa}\nu^6 \quad . \tag{4.16}$$

These two limits mean that for a given broadband force signal, the very low and very high frequency parts of the signal will not be visible above our noise. Thus our protocol automatically comes with an effective bandwidth. We will discuss this in detail in examples.

We will be particularly interested in signals of very short temporal duration τ. If this is short compared to the natural period of the mechanical resonator, $\omega_m\tau \ll 1$, then the resonator is essentially a freely falling body over the time period of integration. We thus focus on frequencies

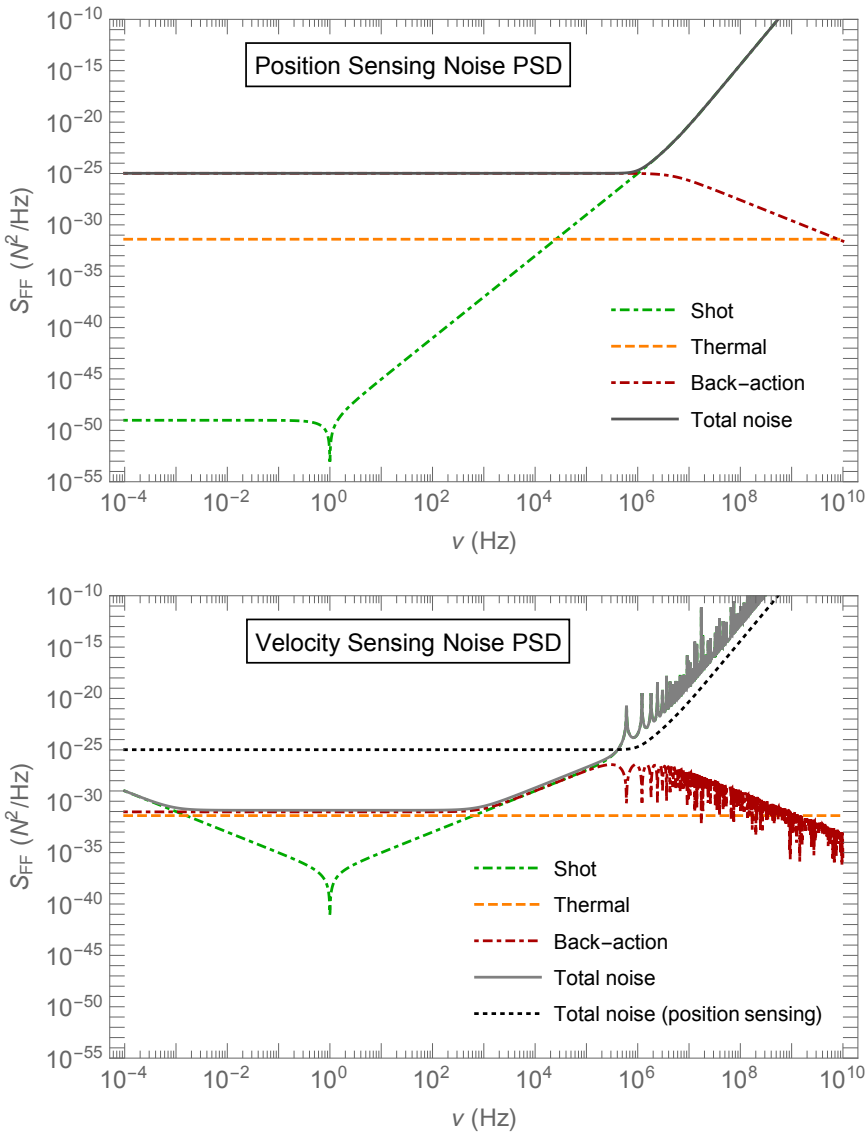

Figure 4.2: Force noise power spectral densities for position sensing in a standard single-sided optomechanical cavity (top) and our velocity sensing protocol in a double ring cavity (bottom). See equations (2.21) and (4.14), respectively. In addition to the spectrally flat thermal noise, we have shot noise and measurement back-action curves. One can clearly see that back-action noise in the velocity sensing protocol is substantially reduced in the range $\omega_m \lesssim \nu \lesssim \kappa$. The spiky features at high frequency come from resonance effects in the two-cavity response function $\propto e^{i[\nu t_d + \phi_c(\nu)]}$. Here in both cases the detector parameters are taken as $m = 1$ g, $\omega_{\rm m} = 1$ Hz, $\gamma = 10^{-4}$ Hz, $\kappa = 10$ MHz, at bath temperature $T = 10$ mK. In the position sensing protocol, optomechanical coupling G is optimized as in equation (2.22) with $\tau = 1$ μs. In the velocity sensing protocol, the delay line parameters are taken as $t_d = 10$ μs, $\mathrm{L} = 10^{-4}$, and the coupling is optimized as in (4.20).

satisfying

$$\omega_m \ll \nu < \kappa. \tag{4.17}$$

In this regime, assuming that the damping of the mechanical resonator is small ($\gamma \ll \omega_m$), we can approximate the noise PSD as

$$N(\nu) \approx \tilde{N}_{BM} + \Theta\nu^2. \tag{4.18}$$

Here

$$\begin{aligned} \tilde{N}_{BM} &= N_{BM} + \frac{4\hbar^2|G|^2 L}{\kappa} \\ \Theta &= \hbar m \left[\frac{m\kappa^3}{4\hbar|G|^2(4+\kappa t_d)^2} + \frac{4\hbar|G|^2(4+\kappa t_d)^2}{m\kappa^3} \right]. \end{aligned} \tag{4.19}$$

We see that there is a white noise contribution (i.e. a renormalization of the thermal noise) as well as frequency-dependent contributions from both the shot and back-action terms. Above $\nu \gtrsim \sqrt{\kappa/2t_d}$, the shot noise term begins to dominate. At these high frequencies, back-action evasion is not effective, and the shot noise term is dominated by the cavity and mechanical response functions.

For small loss $L \approx 0$, we can minimize the noise (4.18) with respect to the optomechanical coupling strength G, i.e. by varying the laser power P. Differentiating, one finds the optimized coupling

$$|G_{\text{opt}}|^2 \approx \frac{1}{4}\frac{m\kappa^3}{\hbar(4+\kappa t_d)^2}. \tag{4.20}$$

Using this, the noise PSD (4.18) becomes

$$N(\nu) \approx N_{BM} + \frac{\hbar m}{t_d^2}\left(L + \nu^2 t_d^2\right). \tag{4.21}$$

We can compare our results to those of the speedmeters being developed for gravitational wave detection, e.g. [58]. Since the force and position noise spectral densities are related by a simple transfer function, $S_{xx} = |\chi_m|^2 S_{FF}$, it is clear that the back-action evasion our protocol achieves is proportionally the same whether reported in position or force units. We obtain a similar basic pattern of noise reduction as [58]: sub-SQL noise in a reasonable band of frequencies, which must be targeted to the desired signal. For gravitational wave detection, the frequencies of interest are near the audio band; here, we are focused on much higher-frequency (radio band) signals, so we have chosen our system parameters accordingly. Moreover, we are focusing here on substantially smaller devices–milligram scale, compared to the gravitational speedmeter experiments with up to 200 kg mirrors, and accordingly smaller cavity lengths. In practice this is a much easier regime for dealing with issues of loss. The basic ideas here could potentially be demonstrated in a chip-scale device as proof of principle before being scaled to macroscopic devices.

4.2.2 Impulse Inference

Our goal is to measure the net impulse delivered to the detector. We interferometrically read out the output light phase $Y'_{out}(t)$ as a time series, and then process this data to infer the

impulse. The simplest option would be to consider the observable

$$I(\tau) = \int_0^\tau F(t)dt, \tag{4.22}$$

where τ is some integration time we can choose, and $F(t)$ is estimated from the observed $Y'_{out}(t)$ using (4.11). The noise in this signal is characterized by the variance,

$$\langle \Delta I^2(\tau) \rangle = \int_{-\infty}^{\infty} d\nu \frac{4\sin^2(\nu\tau/2)}{\nu^2} N(\nu). \tag{4.23}$$

This equation says that the RMS net impulse $\Delta I(\tau)$ delivered to the device purely by noise is calculable from the force noise PSD. As we have seen above, $N(\nu)$ has power law divergences at both high and low frequencies. In (4.23), the sinc function will provide a cutoff on the high-frequency divergence, but the low-frequency divergence is still present. This means that we would naively infer that an infinite random impulse was delivered to the device! Of course, the actual physical impulse is finite. The divergence comes from the shot noise, i.e. counting statistics in our readout photons, and represents the fact that at low frequency this noise becomes arbitrarily large.

This suggests that we use a more intelligent observable than simply the integrated force. Suppose that we are looking for signals of a known shape in time $F_{\text{sig}}(t)$. We want to test for the presence of this signal in our data $F(t)$. To do this we construct an observable $O(t)$ by filtering our data, where the filter scans over different possible event times t_e:

$$O(t_e) = \int f(t_e - t')F(t')dt'. \tag{4.24}$$

By the convolution theorem, for a fixed time (without loss of generality, we can assume $t_e = 0$), the variance in this estimator is,

$$\langle \Delta O^2 \rangle = \int |f(\nu)|^2 N(\nu) d\nu. \tag{4.25}$$

For example, a box filter $f(t) = \Theta(t - \tau) - \Theta(t)$ reproduces the simple estimator (4.23). The signal to noise ratio (SNR) is then defined by

$$\text{SNR}^2 = \frac{|\int f^*(\nu) F_{\text{sig}}(\nu) d\nu|^2}{\int |f(\nu)|^2 N(\nu) d\nu}. \tag{4.26}$$

Now we need a specific filter function which optimizes this signal to noise ratio. As we showed in section 3.7.2 that the SNR is optimized by the filter

$$f_{\text{opt}}(\nu) = \frac{F_{\text{sig}}(\nu)}{N(\nu)}. \tag{4.27}$$

This is sometimes referred to as "template matching" [86, 87]. It says that the optimal filtering protocol is to scan for the expected signal shape renormalized by the noise model. With this choice of filter, the signal to noise ratio is given simply by

$$\text{SNR}^2_{\text{opt}} = \int_0^\infty \frac{|F_{\text{sig}}(\nu)|^2}{N(\nu)} d\nu. \tag{4.28}$$

Here we see a more robust interpretation of the divergences in our noise PSD: the very low and very high frequency parts of the spectrum make no contribution to the SNR.

4.3 Example Signal-to-Noise Calculations

With our measurement protocol and corresponding noise PSD, we can now study our ability to detect particular signals. We begin with an instantaneous force, and then move on to the case of momentum transfer into a sensor by a passing object coupled to the sensor through a long-range force, for example gravity.

4.3.1 Instantaneous Force

Consider an instantaneous force signal

$$F_{\text{sig}}(t) = \Delta p \delta(t - t_0). \tag{4.29}$$

This is a flat function of frequency, $F_{\text{sig}}(\nu) = \Delta p e^{i\nu t_0}/\sqrt{2\pi}$. To estimate the signal-to-noise ratio achievable for such a signal, consider the optimal filter result (4.28). As discussed above, our noise PSD starts to diverge for $\nu \gtrsim \sqrt{\kappa/2t_d}$. There is also a low-frequency divergence starting around the mechanical frequency $\nu \approx \omega_m$. In practice, there can also be some low-frequency cutoff set by a maximum integration time; for example, if we are trying to resolve individual impacts to a sensor which occur at some rate τ_{coll}, the signal from an individual event can only be obtained from frequencies $\nu \gtrsim 1/\tau_{\text{coll}}$. Given these limits, we can then approximate (in fact,

lower-bound) the SNR, using (4.28) and (4.18), as

$$\begin{aligned}\mathrm{SNR}^2 &\gtrsim \frac{\Delta p^2}{2\pi}\int_{\tau_{\mathrm{coll}}^{-1}}^{\sqrt{\kappa/2t_d}} \frac{d\nu}{\tilde{N}_{BM}+\Theta\nu^2} \\ &\approx \frac{\Delta p^2}{4\sqrt{\Theta\tilde{N}_{BM}}}.\end{aligned} \tag{4.30}$$

The approximation in the last line holds if $\sqrt{\Theta\kappa/2\tilde{N}_{BM}t_d} \gg 1 \gg \sqrt{\Theta/\tilde{N}_{BM}\tau_{\mathrm{coll}}^2}$. The first condition says that the detector can move information between cavities fast, and the second says that the collisions do not occur too rapidly, in comparison to the typical time scales occurring in the noise.

As an example, consider the following problem: can we use this protocol to count individual gas collisions with a sensor? Concretely, imagine that we place our sensor in a vacuum chamber and continuously monitor it with our protocol. Let's assume that the sensor is freely-falling, or at least that the mechanical damping γ is so low that we can ignore phononic loss into the support, so that the only "thermal noise" comes from individual gas collisions with the device. We would then view the noise PSD as coming strictly from the quantum measurement-added noise, and the gas collisions are actually the signal we try to detect above the noise. We thus have $N(\nu) = \hbar m(L/t_d^2 + \nu^2)$, and the SNR for a single gas collision transferring a momentum Δp (taken to occur instantaneously) is then just the $\gamma \to 0$ limit of (4.30),

$$\mathrm{SNR}^2 = \frac{\Delta p^2 t_d}{\sqrt{L}\hbar m}. \tag{4.31}$$

This simple answer has a satisfying interpretation: the factor $\hbar m/t_d$ is what one would naively

obtain for a standard quantum limit on impulse sensing over a time t_d (cf. the expression for SQL position uncertainty $\Delta x^2_{SQL} = \hbar t/m$). We are then seeing a noise below the SQL by a factor of the delay line loss $L^{1/4}$, the limiting factor in our protocol. This represents the central idea in this paper: inferring force through a direct measurement of the momentum out-performs use of a position measurement. In the next section, we will see the same behavior for a different problem, the detection of impulses from long-ranged forces.

Numerically, we have in this limit

$$\mathrm{SNR} \approx 1 \times \left(\frac{\Delta p}{10\ \mathrm{keV/c}}\right)\left(\frac{1\ \mathrm{fg}}{m}\right)^{1/2}\left(\frac{10^{-4}}{L}\right)^{1/4}, \tag{4.32}$$

assuming a delay time $t_d \sim 10^{-5}$ sec.[2] Consider helium gas at room temperature. If the atoms scatter elastically off the sensor, the typical momentum transfer should be of the order $\Delta p \sim \sqrt{m_{\mathrm{gas}} k_B T} \sim 10\ \mathrm{keV/c}$. Thus, with a femtogram-scale detector (e.g. [88–90]), we would have the ability to resolve the individual gas collisions above the measurement noise.

Qualitatively, this calculation illuminates a fundamental limitation to momentum sensing. When we look for our signal, we assume some kind of template fitting, as discussed in the previous section. Naively, one might have expected that the best strategy to detect an instantaneous force would be to use a template that is essentially itself a delta function in time. But this is not right: if one only integrates the signal instantaneously, the detection will be limited by shot noise, and in fact the SNR is strictly zero. Quantitatively, we can see that our optimal filter (4.27) has a bandwidth $\Delta\nu \approx \sqrt{\kappa/2t_d}$, and thus finite support as a function of time.

[2]This would require an extremely long optical fiber, but could also be achieved for example by using a third cavity as the "delay line".

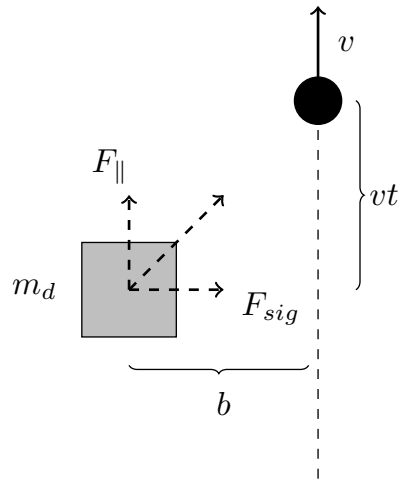

Figure 4.3: Kinematics of the long-range scattering event. A particle passes near the sensor, with impact parameter b and velocity v. This leads to an effective interaction time $\tau \sim b/v$.

4.3.2 Long Range Forces

Now we consider detection of some object approaching the sensor and interacting with it through a long range force. Our primary motivation here is the gravitational detection of passing dark matter [21], but the problem can be phrased more generally. We consider a $1/r$ potential between sensor and incoming particle

$$V(t) = \frac{\beta}{r(t)}. \tag{4.33}$$

Here β is a constant with dimensions of $\text{energy} \times \text{length}$ which characterizes the long range force. For example, $\beta = Q_1 Q_2 / 4\pi$ for the Coulomb force between two charges, or $\beta = G_N m_1 m_2$ for the Newtonian gravitational force.

Consider a particle passing by the detector at a high velocity v and impact parameter b interacting with a sensor via (4.33), as in figure 4.3. For simplicity, we assume that the particle's trajectory is a straight line. Almost all of the momentum is transferred to the sensor over a

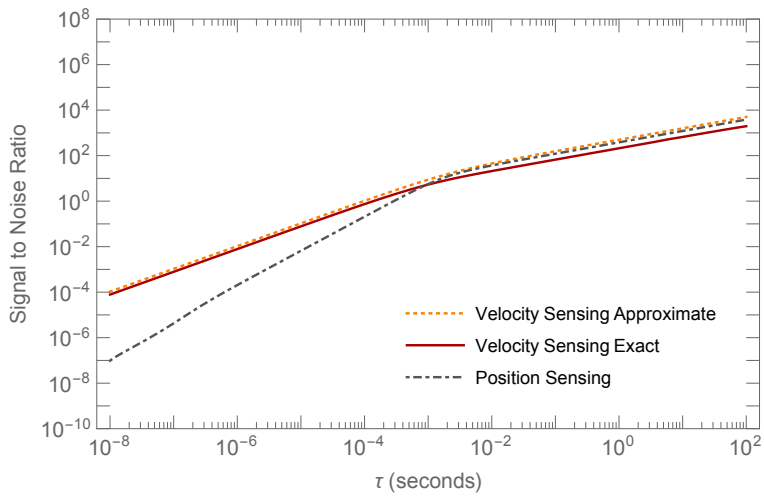

Figure 4.4: Signal to noise ratio for long range force detection, as a function of fly-by time τ. We see a clear improvement in the SNR obtained with our velocity sensing protocol (4.14) compared to the result with position sensing (2.21), for fast signals. For slow signals (here, $\tau \gtrsim 1$ ms), the measurement-added noise becomes subdominant to the thermal noise, and our back-action-evasion scheme does not help. To check our approximate result (4.37), we also display the exact SNR calculated using the full noise PSD (4.14) and signal (4.35). Here we use the same detector parameters as in figure 4.2 and at optimized G for both cases [see (4.20),(2.22)], and use the gravitational dark matter signal as in (4.41) with a very heavy dark matter candidate $m_\chi = 10$ mg and impact parameter $b = 1$ mm.

timescale $\tau \sim b/v$ when the particle is nearest to the sensor. The force acting on the sensor has pieces parallel and perpendicular to the particle track. The parallel component of the force exerted over this time period transfers no net momentum to the sensor. Thus we focus on the perpendicular component of the force,

$$F_{\text{sig}} = \frac{\beta b}{(b^2 + v^2 t^2)^{3/2}}. \tag{4.34}$$

The Fourier transform of this signal is

$$F_{\text{sig}}(\nu) = \sqrt{\frac{2}{\pi}} \frac{\beta |\nu|}{v^2} K_1 \left(\frac{b}{v} |\nu| \right) \tag{4.35}$$

where K_1 is a modified Bessel function. For the purposes of estimating a signal-to-noise ratio in (4.28), we can approximate (in fact, underestimate) this signal using an exponential

$$F_{\text{sig}}^{\text{approx}}(\nu) = \sqrt{\frac{2}{\pi}}\frac{\beta}{bv}e^{(-\tau|\nu|/2)}. \tag{4.36}$$

As discussed in the previous section, the noise PSD starts to diverge at frequencies above $\nu \gtrsim \sqrt{\kappa/2t_d}$. We can therefore approximate the signal-to-noise ratio (4.28) here as

$$\begin{aligned} \text{SNR}^2 &\approx \frac{2\beta^2}{\pi b^2 v^2}\int_0^{\sqrt{\kappa/2t_d}} \frac{e^{-\tau\nu}}{\tilde{N}_{BM} + \Theta\nu^2} d\nu \\ &\gtrsim \frac{\beta^2}{b^2 v^2 \tau \tilde{N}_{BM}} \frac{1}{(1+\eta)}. \end{aligned} \tag{4.37}$$

The approximation in the second line is good as long as $\tau\sqrt{\kappa/2t_d} \gtrsim 1$. The dimensionless parameter η is defined as

$$\eta = \sqrt{\Theta/\tilde{N}_{BM}\tau^2} \gg 1, \tag{4.38}$$

with this inequality holding in examples, to which we now turn. We have numerically verified that these approximations to the exact SNR calculated using the full noise PSD (4.14) and signal (4.35) are highly accurate, see figure 4.4.

We now use this formalism to show the central result of this paper: momentum monitoring out performs position monitoring for measuring rapid impulses. Specifically, with G optimized as in (4.20) and with small enough loss coefficient so that $\tilde{N}_{BM} \approx N_{BM} = 4\gamma m k_B T$, we can write the parameter $\eta^2 = (\hbar m/\tau)/(N_{BM}\tau)$. If our measurement protocol had SQL-level measurement

noise (see section 2.2 for details), the variance in our measured impulse would be given by

$$\Delta p^2_{\text{noise}} = N_{BM}\tau + \frac{\hbar m}{\tau} = N_{BM}\tau(1+\eta^2). \tag{4.39}$$

Here the first term comes from thermal noise and the second from the SQL measurement noise. In contrast, reading off the denominator of (4.37), we find with our protocol that the noise is

$$\Delta p^2_{\text{noise}} = N_{BM}\tau(1+\eta), \tag{4.40}$$

thus we have a reduction in noise by a factor $1/(1+\eta) \ll 1$. This is the analogue in the long-range detection problem to the noise reduction displayed in (4.31).

This result could be further improved by including the benefits of using squeezed light for detection. The noise above arises from assuming that the X and Y quadratures noises are uncorrelated, which is an assumption that is broken for squeezed light. For position monitoring, the appropriate quadrature and amplitude of light – necessary choices for using squeezing to improve the measurement – depend sensitively on the bandwidth and target frequency of the signal. That is, shot noise and back-action in those settings scale differently with frequency. Here, however, the frequency dependence from ω_m up to $\sim \kappa$ is the same for both quadratures, and thus broadband squeezed light suffices.

As a numerical example, we now consider explicitly the gravitational detection of a passing particle, for example a heavy dark matter candidate [21]. The key scaling property in this problem is that the signal strength scales linearly in both the sensor mass m_s and dark matter mass m_χ, and is enhanced by small impact parameters as $1/b^2$. In contrast, the noise scales like $\sqrt{m_s}$. In

a terrestrial experiment, individual dark matter particles pass through the lab at the "wind speed" $v_{DM} \sim 220\ \mathrm{km/s}$. Considering a fiducial impact parameter on the millimeter scale then leads to a very short flyby time $\tau \sim 10^{-8}\ \mathrm{sec}$. In this setting we obtain an SNR

$$\begin{aligned} \mathrm{SNR} &\approx \frac{G_N m_\chi m_s}{bv\sqrt{\tau N_{BM}}} \frac{1}{\sqrt{(1+\eta)}} \\ &\approx 10^{-3} \times \left(\frac{m_\chi}{10\ \mathrm{mg}}\right) \left(\frac{m_s}{1\ \mathrm{g}}\right)^{\frac{1}{2}} \left(\frac{\tau}{10\ \mathrm{ns}}\right) \left(\frac{1\ \mathrm{mm}}{b}\right)^2, \end{aligned} \tag{4.41}$$

where we take the thermal Brownian noise at dilution refrigeration temperature $T \sim 10\ \mathrm{mK}$ and assumed a very high-Q, low-frequency resonant detector with $\gamma \sim 10^{-4}\ \mathrm{Hz}$. The scaling with τ in the numerical estimate here is valid for signals fast enough that $\eta \gtrsim 1$, in which case the SQL level measurement added noise is greater than the thermal noise in the system $\hbar m/\tau^2 \geq N_{BM}$. In this example, the crossover occurs around $\tau \sim 1\ \mathrm{ms}$, as can be seen from figure 4.4.

From this estimate, we see that this measurement protocol is not yet sensitive enough for gravitational detection of Planck scale ($m_\chi \sim m_P \sim 10\ \mu\mathrm{g}$) dark matter particles. A more sophisticated protocol will be necessary to achieve the goals outlined in [21], for example, using squeezed light. However, a device with the sensitivity given here could be used, for example, to exclude dark matter models which couple through some other long range force a few orders of magnitude stronger than gravity, for example the modified gravity models in [91] or some composite dark sector models coupled through a new light gauge boson (e.g. [92–94]). Bounds on these types of dark matter models coming from impulse sensing detectors will be studied in detail in a future publication.

4.4 Slight Detuning

It is experimentally challenging to maintain both the ring cavities at the same equilibrium resonance frequency. We can quantify the impact of a slight imperfection by introducing a small amount of detuning to both the cavities. To get some intuition in a simple setting, we begin with a single sided cavity to understand how a slight detuning affects the quadratures of interest and the noise PSD. Then we move on to a qualitative discussion on the effects of detuning in our velocity measurement protocol with a double ring cavity, and provide some numerical estimates.

4.4.1 Slight Detuning in a Single Sided Cavity

With the introduction of detuning in the system, the single sided cavity Hamiltonian gets modified to

$$H = -\hbar\Delta a^\dagger a + H_{mech} + H_{int}. \tag{4.42}$$

Let us first consider this scenario in terms of the phase picked up by the cavity field. We are interested in the limit that the signal is much faster than both the mechanical period and the delay time. Thus we can consider the phase shifts picked up in the limit that the mechanical element is stationary. For a detuned single-sided cavity, the Hamiltonian is given in (4.42) where the interaction term is proportional to $\hbar g_0 a^\dagger a x/x_0$ before linearization. The quantum Langevin equation for the optical field in the cavity is

$$\dot{a} = i(\Delta - g_0\frac{x}{x_0})a - \frac{\kappa}{2}a + \sqrt{\kappa}a_{in}. \tag{4.43}$$

We can define an effective detuning parameter

$$\Delta_{\text{eff}} = \Delta - g_0 \frac{x}{x_0}. \tag{4.44}$$

Then for a steady state solution in the cavity, we obtain the phase shift of the light

$$a = \frac{\sqrt{\kappa}}{-i\Delta_{\text{eff}} + \kappa/2} a_{in}. \tag{4.45}$$

Following the input-output relation for the optical field we obtain the output field

$$\begin{aligned} a_{out} &= a_{in} - \sqrt{\kappa} a \\ &= \frac{-i\Delta_{\text{eff}} - \kappa/2}{-i\Delta_{\text{eff}} + \kappa/2}\, a_{in} \\ &= e^{i\phi} a_{in}. \end{aligned} \tag{4.46}$$

This phase shift formalism will be more important in our discussion of the double ring cavity in the next section. We can also use the familiar quadrature formalism to describe our detuned single sided cavity. The equations of motion from the above Hamiltonian are

$$\begin{aligned} \dot{X} &= -\frac{\kappa}{2} X + \sqrt{\kappa} X_{in} - \Delta Y \\ \dot{Y} &= -Gx - \frac{\kappa}{2} Y + \sqrt{\kappa} Y_{in} + \Delta X \\ \dot{p} &= -\hbar G X - m\omega_m^2 x - \gamma p + F_{in} \\ \dot{x} &= \frac{p}{m}. \end{aligned} \tag{4.47}$$

Note that the optical quadratures are now coupled through this detuning parameter.

We can solve for these equations of motion and obtain the following expression for the amplitude and phase quadratures in the cavity :

$$\begin{pmatrix} X \\ Y \end{pmatrix} = \frac{1}{f} \begin{pmatrix} \frac{\kappa}{\chi_c \chi_m} & -\frac{\sqrt{\kappa}\Delta}{\chi_m} & G\Delta \\ \sqrt{\kappa}\left[G^2\hbar + \frac{\Delta}{\chi_m}\right] & \frac{\kappa}{\chi_c \chi_m} & -\frac{G\sqrt{\kappa}}{\chi_c} \end{pmatrix} \begin{pmatrix} X_{\text{in}} \\ Y_{\text{in}} \\ F_{\text{in}} \end{pmatrix} \tag{4.48}$$

where

$$f = \frac{1}{G^2\hbar\Delta + \chi_m^{-1}(\kappa\chi_c^{-2} + \Delta^2)}. \tag{4.49}$$

Then we follow the input-output relations given in Eq. (5.24) to find the output quadratures. Since $\Delta \neq 0$ leads to mixing of the optical quadratures, the force signal F_{in} is now imprinted on both X_{out} and Y_{out}. We can choose an optimal quadrature to measure by linearly combining these so that the signal is in a single quadrature. Let's define

$$\begin{aligned} a &= \frac{-G\Delta\sqrt{\kappa}}{G^2\hbar\Delta + \chi_m^{-1}(\kappa\chi_c^{-2} + \Delta^2)} \\ b &= \frac{G\kappa\chi_c^{-1}}{G^2\hbar\Delta + \chi_m^{-1}(\kappa\chi_c^{-2} + \Delta^2)}. \end{aligned} \tag{4.50}$$

Naively, we would like to consider the quadratures

$$\begin{aligned} Q_{\text{out}} &= aX_{\text{out}} + bY_{\text{out}} \\ P_{\text{out}} &= bX_{\text{out}} - aY_{\text{out}}. \end{aligned} \tag{4.51}$$

The P quadrature here has no dependence on F_{in}, so all of the signal is encoded in the Q

quadrature. We would then like to monitor the Q quadrature, but here the coefficients a, b are functions of frequency ω, so constructing the appropriate filter would be exceedingly difficult. Instead, we can just evaluate these coefficients at our frequency of interest $\omega_{\text{sig}} \sim 1/\tau$. Using $a(\omega_{\text{sig}}), b(\omega_{\text{sig}})$, we define the observed quadrature

$$Q_{\text{meas}} = a(\omega_{\text{sig}})X_{\text{out}} + b(\omega_{\text{sig}})Y_{\text{out}}. \tag{4.52}$$

To convert this measured output to a force, we divide through by the appropriate coefficient,

$$F_E = \frac{Q_{\text{meas}}}{a^2 + b^2}, \tag{4.53}$$

cf. equation (2.20). With these choices we can find the force noise PSD. Finally, we still have the freedom to optimize the optomechanical coupling G. As before, we can find the optimized optomechanical coupling strength G_{opt} by minimizing the contribution from the measurement-added part of the noise, at the frequencies of interest around $1/\tau$. Doing so, and using the result in the noise PSD, we obtain the optimized noise PSD for the slightly detuned single sided cavity. See figure 4.5 for a comparison of the resulting noise PSD with the noise PSD in the case of exact cavity resonance (2.21).

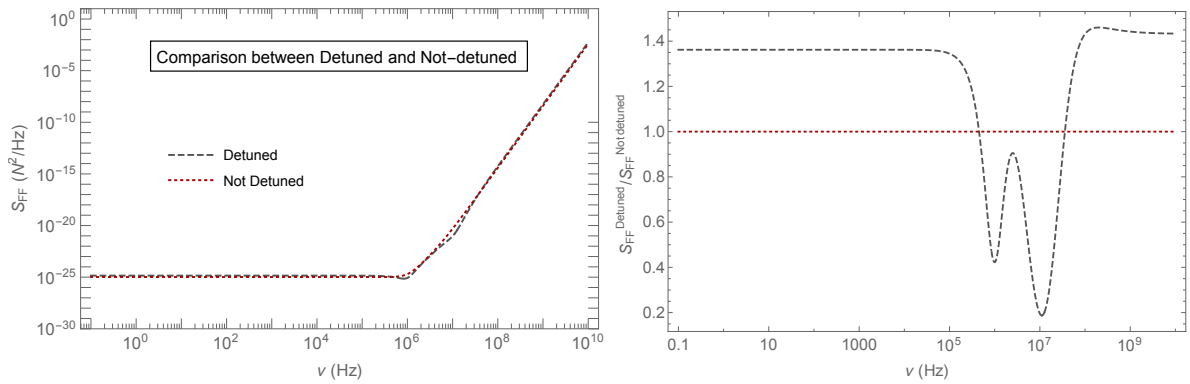

Figure 4.5: Comparison between noise power spectral densities in a single-sided cavity with detuning and without detuning (2.21). We show that the features of the noise PSD curves are similar when optimized. Here the detector parameters are the same as in figure 4.2, and we take detuning $\Delta \approx \kappa$. We plot the ratio in between the noise PSD of detuned and non-detuned scenarios. Note that there is a frequency regime where the detuned noise PSD gives us lower noise than the non-detuned case.

4.4.2 Slight Detuning in Double Ring Cavities

Similar to the single-sided cavity example illustrated above, we can introduce detuning to both the cavities in the system and obtain the following equations of motion:

$$
\begin{aligned}
\dot{X} &= -\frac{\kappa}{2}X + \sqrt{\kappa}X_{in} - \Delta Y \\
\dot{Y} &= -Gx - \frac{\kappa}{2}Y + \sqrt{\kappa}Y_{in} + \Delta X \\
\dot{X}' &= -G'x\sin\theta - \frac{\kappa'}{2}X' + \sqrt{\kappa'}X'_{in} - \Delta' Y' \\
\dot{Y}' &= G'x\cos\theta - \frac{\kappa'}{2}Y' + \sqrt{\kappa'}Y'_{in} + \Delta' X' \\
\dot{p} &= -\hbar G X + \hbar G'\left(X'\cos\theta + Y'\sin\theta\right) - m\omega_m^2 x - \gamma p + F_{in} \\
\dot{x} &= \frac{p}{m}
\end{aligned}
\tag{4.54}
$$

where the optomechanical coupling strength of the second cavity is related to that of the first cavity as

$$G' = G\sqrt{1-L}\sqrt{\frac{\kappa'}{\kappa}}\sqrt{\frac{\Delta^2+\kappa^2/4}{\Delta'^2+\kappa'^2/4}} \tag{4.55}$$

and the phase θ is defined as,

$$e^{i\theta} = \frac{-i\Delta-\kappa/2}{-i\Delta'+\kappa'/2}\sqrt{\frac{\Delta'^2+\kappa'^2/4}{\Delta^2+\kappa^2/4}}. \tag{4.56}$$

It is hard to get tractable analytical expressions for the double ring cavity given the complexity of the coupled equations of motion. So, we will first qualitatively discuss the effect of introducing detuning into both of the cavities and then demonstrate some numerical results.

In standard displacement sensing, the mechanical position $x(t)$ is imprinted onto the light. Measurement of the light then causes backaction on the mechanics. Here, to avoid this backaction, we have suggested instead that one wants to monitor the mechanical velocity $v(t)$, with no measurement of position. In our two-cavity system, the light picks up a total phase shift $\Delta\phi = \phi_1 + \phi_2$. The condition that we do *not* measure position then says that

$$\frac{d}{dx}(\phi_1+\phi_2) = 0. \tag{4.57}$$

We will show that this condition can be achieved by satisfying a simple constraint on the two cavity detunings Δ, Δ' and couplings g_0, g_0'.

Following the phase shift formalism introduced in the section above, the first cavity picks

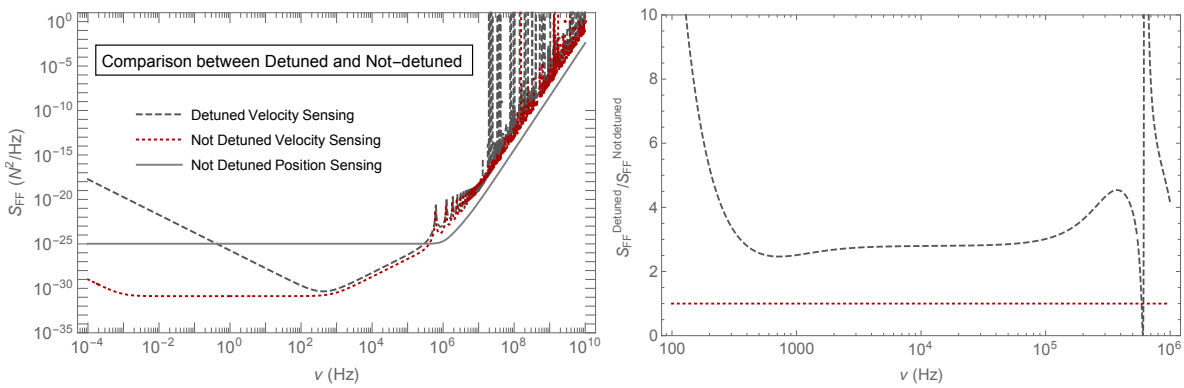

Figure 4.6: Comparison between noise power spectral densities in a double ring cavity with detuning and without detuning. Here the detector parameters are the same as in figure 4.2, and we take detuning $\Delta' \approx \kappa \approx -\Delta$ assuming $g_0' \sim -g_0$ and $\kappa' \sim \kappa$. The optomechanical coupling strength is optimized for the non-detuned scenario as in (4.20) and the detuned case has been plotted for the same circulating power as in the non-detuned case. We see that in the region where we have optimized for backaction evasion, here for 10^4 Hz $< \nu < 10^6$ Hz, the effects of detuning are minor once we impose our coupling condition (4.60).The ratio plot at the bottom shows the comparison in this zoomed in region.

up a phase proportional to,

$$a_{\text{out}} = e^{i\phi_1} a_{\text{in}}. \tag{4.58}$$

Now with a second cavity, in the limit that we can ignore losses in the delay line and treat the mechanics as stationary, the output light of the second cavity similarly picks up a phase shift involving x. We find

$$a'_{\text{out}} = e^{i\phi_2} a'_{\text{in}} = e^{i(\phi_1+\phi_2)} a_{\text{in}}. \tag{4.59}$$

The total phase shift $\phi_1 + \phi_2$ is written in terms of the two effective detunings $\Delta_{\text{eff}}, \Delta'_{\text{eff}}$.

For a backaction evading measurement, our main goal is to eliminate the position dependence from this total phase. Mathematically this is just the statement of (4.57). Using the above results for the phase shifts, at zero frequency of the mechanical oscillator, the phase

matching condition reduces to

$$\frac{\Delta'^2 + \kappa'^2/4}{\Delta^2 + \kappa^2/4} = -\frac{g_0'}{g_0}\frac{\kappa'}{\kappa} \tag{4.60}$$

which relates the detunings and couplings in the two cavities. In the final expression we have assumed that for $g_0 \ll \Delta \sim \kappa$, $\Delta_{\text{eff}}^2 \sim \Delta^2$ (and similarly $\Delta_{\text{eff}}'^2 \sim \Delta'^2$). If this condition is satisfied, the measurement will evade mechanical backaction, which is straightforward for $g_0'/g_0 < 0$ as in our double cavity design and for $|\omega_c - \omega_c'| \sim \kappa \sim \kappa'$.

Thus we can choose detunings in both the cavities to satisfy the above ratio in order to evade the backaction noise. After doing this, we solve the equations of motion and choose the optimal quadrature of the light coming out of the second cavity, similar to the description given for the single-sided case (4.51) to account for the total phase shift given in (4.59). This gives the noise PSD in the force estimator as before. This can be compared with the noise PSD in the case of zero detuning, cf. equation (4.21). The resulting formulas are too cumbersome to write down explicitly, but can be easily evaluated symbolically on a computer.

In figure 4.6, we provide a numerical example comparing the noise in the detuned and non-detuned cases. The noise PSD in the non-detuned case is optimized with the optomechanical coupling strength given in (4.20). For simplicity, we use the same circulating power inside the cavities for both scenarios which means use of higher amount of input laser power in the detuned case than the non-detuned case, although this choice could potentially be further optimized. From the figure, we see that in the frequency regime $\omega_m \ll \nu \lesssim \kappa \sim \Delta$, the effects of relative cavity differences can be largely compensated for by optimizing the relative couplings and detunings, though we pay a price by having higher noise in the lower frequency regime of the PSD. As

we are interested in signals in the radio band, we can see that our backaction-evasion strategy is highly robust to the presence of small mismatches in the two cavity parameters.

4.5 Conclusions and Discussion

Detection of a rapidly delivered impulse is a ubiquitous problem in many branches of physics. Fundamental quantum measurement noise in such a detection is often the ultimate limitation to reaching better sensitivities. In this paper, we have demonstrated that the use of a direct momentum sensing protocol can significantly reduce this noise in comparison with the more traditional approach of position sensing.

Here, we have presented a concrete example of this general phenomenon using an optomechanical system involving a pair of cavities probed continuously by a laser. This specific approach is ultimately limited by optical losses in a delay line which transmits the probe light between the cavities. With currently available fabrication techniques, these losses limit the noise reduction in this protocol to around 30 dB below the standard quantum limit. Other protocols, for example involving discrete pulse sequences [61] or direct measurement of velocity through an inductive coupling [95] could improve the situation, and require more detailed future study.

Given that momentum measurement or impulse detection is commonly needed, the results presented here could have wide applications. We gave a pair of examples, one in metrology and the other in particle physics. In the former, we suggested that our protocol is already sensitive enough [see equation (4.32)] to monitor all of the individual gas particles colliding with a femtogram-scale sensor in a room temperature, high vacuum environment. This could be used for example in quantum-limited pressure calibrations. In the latter, we studied the application of

this protocol to the detection of heavy dark matter candidates purely through their gravitational interaction with a sensor [21]. Although the sensitivity of the simple protocol presented here [see equation (4.41)] is too limited by optical losses to achieve the requirements of [21], this study shows a clear path to straightforward improvements, which we leave to future work. We hope that the example studied in this paper serves to guide the way to impulse measurement schemes reaching the fundamental limits allowed by quantum mechanics, enabling detection of such extremely weak signals.

Chapter 5: Combining Squeezing with Backaction Evasion

The content of this chapter is in pre-print as Ghosh et al., arXiv:2211.14460 [96] with collaborators Matthew Feldman, Seongjin Hong, Claire Marvinney, Raphael Pooser and Jacob M. Taylor. [1]

5.1 Introduction

State-of-the-art force sensors operate near the standard quantum limit (SQL) making possible the detection of weak impulses relevant to a plethora of physics [28, 97–100]. Broadband impulse metrology has recently been proposed to detect dark matter [21, 36, 49] and involves the measurement of rapid and minute impulses allowing for the detection of forces across a wide range of frequencies. Currently, the Windchime collaboration is developing such impulse measurement techniques using an array of mechanical sensors to aim for heavy dark matter detection through long range interactions [22]. Impulse metrology has potential applications in other fields as well including but not limited to low-energy single-photon detection and quantum noise-limited pressure calibrations accounting for gas collisions [67, 68, 70–72]. We are interested in impulse metrology with optomechanical sensors. Optomechanical sensors work by transducing a force acting on mechanical systems to measurable optical signals and are

[1] I have specifically contributed to the mathematical analysis of the toy models and the noise limits for various search strategies along with writing the manuscript.

relevant to very sensitive force measurements [24, 73–76, 101].

In this article, we determine the advantages of probing optomechanical systems with squeezed light in position and momentum sensing schemes combining two different quantum noise reduction methods. We find that the noise reduction through squeezing is compatible with the concurrent implementation of backaction evasion through a QND momentum measurement in the free mass regime. Our noise reduction scheme has implications to dark matter detection and quantum metrology more broadly, as our scheme provides an improvement over a broad frequency band and simultaneously simplifies the technical challenges of using squeezed light for impulse metrology.

Squeezed light and backaction evasion (BAE) are quantum resources that may be leveraged to reduce the measurement-induced noise below the SQL. Squeezed light has been used to enhance the signal-to-noise ratio (SNR) in atomic-force microscopy [102] and microelectromechanical (MEMS) cantilevers [103], and most famously to detect gravitational waves in the LIGO collaboration [104]. However, in traditional quantum enhanced metrology, position measurements with squeezed light have the maximum benefit when realized for a narrow-band force signal [77, 105]. We also consider quantum non-demolition (QND) measurements, where repeated measurements of a single observable result in no increment in uncertainty over time and yield the same precise result every time in the absence of any external influence. A QND measurement is accomplished when an observable is unaffected due to the quantum uncertainty produced in the corresponding non-commutative conjugate variable [28, 45, 63, 106]. A class of QND measurements known as backaction evading measurements are attainable when we can measure an observable devoid of backaction from the measuring apparatus. Backaction evasion experiments have been implemented using four-wave

mixing [107] and optical parametric amplifiers [108], and have enhanced the sensitivity of optomechanical systems [64, 109–112]. Several quantum noise reduction techniques have been investigated especially in the context of gravitational wave [113–117] and dark matter detection [118–121]. Here, we will focus on the prospect of using squeezing, backaction evasion and QND techniques simultaneously to enhance sensitivity to weak impulses.

5.2 Benefits of Squeezing

5.2.1 Single-mode Squeezing Toy Model

Here, we present a toy model for a backaction induced measurement system, where light interacts with the position of the system twice, and the interactions are separated by the free evolution of the system in between, as seen in the schematic diagram of Fig. 5.1a and the proposed experimental implementation of Fig. 5.3a. The interaction Hamiltonian for our toy model is given by

$$H_{\text{int}} = \hbar G x X, \tag{5.1}$$

where x is the position of the system, X is the amplitude quadrature of light, and G is the optomechanical coupling strength enhanced by the displacement amplitude α. In our model, the radiation pressure of the light alters the momentum of the mechanical system. During the free evolution of the system, this shift in momentum causes a change in the position of the optomechanical system as seen in Fig. 5.1a. Incorporating the free evolution in this manner allows us to model the effect of the backaction in the system. In the subsequent interaction, the

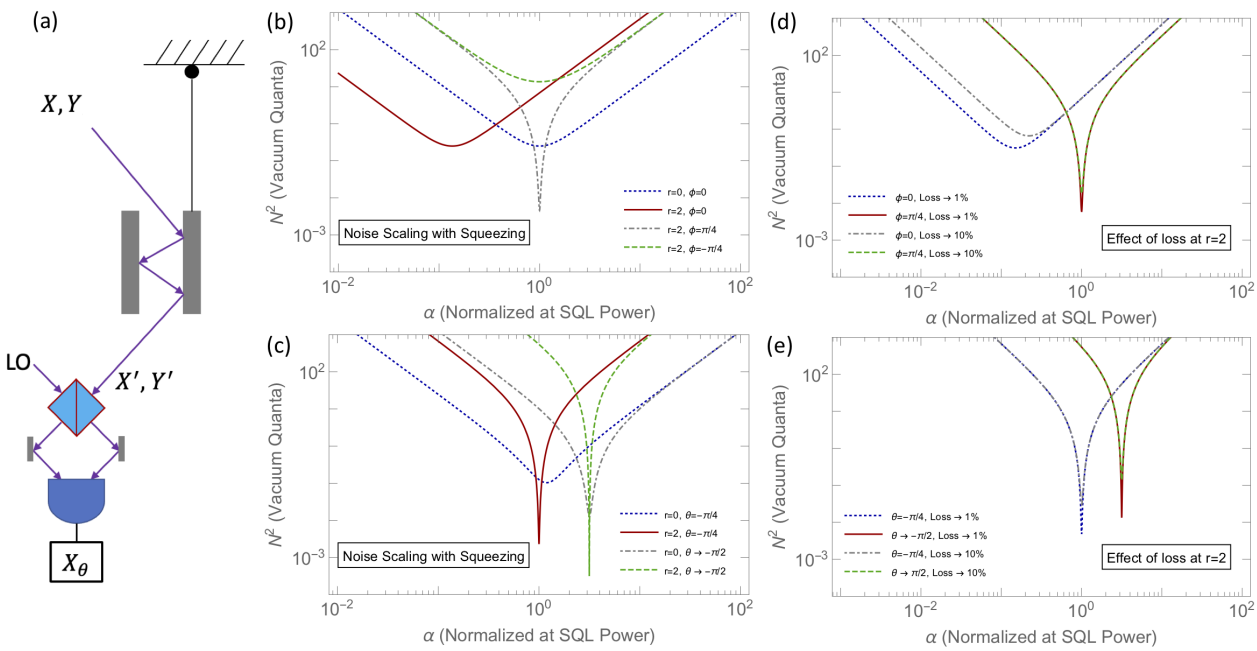

Figure 5.1: Position measurements using single-mode squeezed light. a) A position measurement comprising a single-sided optomechanical system probed with single-mode squeezed light with quadratures X and Y. In this proposed scheme the measured quadrature X_θ is read out using homodyne detection by interfering the output with a local oscillator (LO). b) Phase quadrature measurement ($\theta = 0$) at squeezing strengths $r = 0, 2$ and squeezing angles $\phi = 0, \pm\pi/4$ with the parameter $\beta = 1$. The displacement amplitude α is normalized to the power required to achieve the SQL. Here the power at the SQL is the solution to Eq. 5.7 where we optimize with respect to α at $\theta, \phi = 0$. The optimal noise floor for measuring the phase quadrature with $r > 0$ occurs at $\phi = \pi/4$ while at $\phi = 0$ squeezing provides a reduced power to attain the same noise floor. c) Noise for measurement quadratures $\theta = -\pi/4, -\pi/2$ with $\phi = 0$ and $\beta = 1$ where the optimal noise floor occurs at a $\theta = -\pi/2$, effectively an amplitude quadrature measurement. d) Effect of loss on phase quadrature measurement. e) Effect of loss on quadrature measurements $\theta = -\pi/4, -\pi/2$.

change in position is transduced to the phase quadrature of the light, Y. The above has following unitary evolution where we approximate the more common continuous process by the third-order Suzuki-Trotter approximation. :

$$U_{\text{tot}} = U_{\text{int}} U_{\text{free}} U_{\text{int}} = e^{-i\zeta x_0 X} e^{-i\beta \frac{p_0^2}{2}} e^{-i\zeta x_0 X}, \tag{5.2}$$

where x_0 and p_0 are the dimensionless position and momentum operators of the optomechanical system. These are normalized to a length and momentum scale comparable to the De Broglie wavelength $\lambda = \sqrt{\frac{\hbar^2}{2mK_BT}}$ where m and T are the mass and temperature of the moving mirror, respectively. For a harmonic oscillator scenario, the length scale is set by $K_BT \to \hbar\omega$. Thus, we interpret the parameter β as a dimensionless factor accounting for the free evolution of the system described by $\beta = \hbar t/(m\lambda^2)$ with the free evolution time $t \sim 1/\kappa$ where κ is the cavity linewidth. The parameter ζ is dependent on the displacement amplitude of the optical pulse via, $\zeta = \alpha\mu$, where μ is a dimensionless quantity defined in terms of the interaction time and the single photon optomechanical coupling strength in frequency units g, $\mu \sim g/\kappa$. By applying these unitaries, the momentum, the phase quadrature of the probing light and the position operators transform as follows,

$$\begin{aligned} U_{\text{int}}^{\dagger} p_0 U_{\text{int}} &= p_0 - \zeta X, \\ U_{\text{int}}^{\dagger} Y U_{\text{int}} &= Y - \zeta x_0, \text{ and} \\ U_{\text{free}}^{\dagger} x_0 U_{\text{free}} &= x_0 + \beta p_0. \end{aligned} \tag{5.3}$$

The remaining unitary transformations do not change the operators since X, Y and p_0 commute with U_{free} while x_0 and X commute with U_{int}. The transformation of the operators

under the full unitary evolution Eq. 5.2 can be represented as,

$$
\begin{aligned}
Y' &= U_{\text{tot}}^{\dagger} Y U_{\text{tot}} = Y - 2\zeta x_0 - \zeta\beta p_0 + \zeta^2 \beta X, \\
X' &= U_{\text{tot}}^{\dagger} X U_{\text{tot}} = X, \\
x' &= U_{\text{tot}}^{\dagger} x U_{\text{tot}} = x_0 + \beta p_0 - \beta\zeta X, \\
p' &= U_{\text{tot}}^{\dagger} p U_{\text{tot}} = p_0 - 2\zeta X.
\end{aligned}
\tag{5.4}
$$

Let us consider the arbitrary quadrature X_θ output from the system described by the unitary transformations in Eq. 5.4

$$
\begin{aligned}
X_\theta &= Y' \cos\theta \quad + X' \sin\theta \\
&= \cos\theta (Y - 2\zeta x_0 - \zeta\beta p_0 + \zeta^2 \beta X) + \sin\theta X,
\end{aligned}
\tag{5.5}
$$

where X' and Y' are the output amplitude and phase quadratures of the system (see Fig. 5.1a), and θ is the quadrature angle. We see that the quadrature has shot noise terms independent of ζ, signal terms proportional to ζ and a backaction term proportional to ζ^2. For the right combination of quadratures, the $\sin\theta X$ term can cancel the backaction term. Another way to reduce the backaction noise is through quantum non-demolition measurements [45]. In this scenario, we can continuously monitor a QND variable like momentum in a free particle system instead of the position, to reduce or eliminate the backaction term, thereby achieving backaction evasion. In section 5.4 we discuss how to perform a QND measurement to evade backaction noise in detail. For the toy model, we restrict our discussion to the continuous monitoring of position to showcase the benefits of squeezing. We obtain the estimator variable x_E for the system position by dividing

X_θ by the multiplicative factor $2\zeta\cos\theta$,

$$\begin{aligned} x_E &= X_\theta/(-2\zeta\cos\theta) \\ &= -\frac{Y}{2\zeta} + x_0 + \frac{\beta p_0}{2} - \frac{\zeta\beta X}{2} - \frac{\tan\theta X}{2\zeta}. \end{aligned} \tag{5.6}$$

From Eq. 5.6, we see that a judicious choice of θ allows us to cancel out the backaction noise from the amplitude quadrature. We find that the optimal θ is dependent on ζ^2 (which is proportional to power α^2). The noise power spectral density (PSD) is proportional to the square of the estimator variable, x_E. To analyze the measurement-induced noise of our system we evaluate $N^2 = (x_E - (x_0 + \beta p_0/2))^2$, since N^2 is proportional to the variance of the system position, which may be written as

$$\begin{aligned} N^2 = &\frac{Y^2}{4\zeta^2} + \frac{\zeta^2\beta^2 X^2}{4} + \frac{\tan^2\theta X^2}{4\zeta^2} + \frac{\beta\{X,Y\}}{4} \\ &+ \frac{\tan\theta\{X,Y\}}{4\zeta^2} + \frac{\beta\tan\theta X^2}{2}. \end{aligned} \tag{5.7}$$

For squeezed light all of the terms in Eq. 5.7 are non-zero. The vacuum expectation values of the correlators after squeezing can be represented as [122],

$$\begin{aligned} \langle X^2\rangle &= \frac{1}{2}\left(e^{2r}\cos^2\phi + e^{-2r}\sin^2\phi\right), \\ \langle Y^2\rangle &= \frac{1}{2}\left(e^{-2r}\cos^2\phi + e^{2r}\sin^2\phi\right), \text{ and} \\ \langle\{X,Y\}\rangle &= \frac{1}{2}(e^{-2r} - e^{2r})\sin 2\phi, \end{aligned} \tag{5.8}$$

where r, ϕ are the squeezing strength and squeezing angle, respectively. For a position measurement, where the phase quadrature ($\theta \to 0$) is measured, the cross-correlator term can be

made negative by choosing a suitable squeezing angle and increasing the squeezing strength to reduce the noise floor, N^2 as seen in Fig. 5.1b. We can access the same noise floor at a lower power by probing the system with squeezed light (red solid curve) rather than a coherent state (blue dashed curve). A squeezing angle of $\phi = \pi/4$ provides a lower noise floor (gray dashed curve) at the original power. This scenario is attained by adding a negative contribution from the cross-correlator term to the noise.

Alternatively, we explore combinations of the quadratures which reduces the backaction term to achieve a lower noise floor when using squeezed light (see Fig. 5.1c). We may globally minimize the contribution of the measurement-induced noise by optimizing the quadrature angle θ. The optimization at $\phi = 0$ gives us

$$\theta \to -\tan^{-1}(\zeta^2\beta). \tag{5.9}$$

Here, we see that the quadrature angle is strongly dependent on the power of the light. Hence, when working deep in the backaction limit, at high power we are nearly measuring the amplitude quadrature which is devoid of any information about the system position, and slight fluctuation in power will destroy this benefit.

The optical losses in our system are a critical consideration when probing it with squeezed light. Here, we evaluate the effect of the expected optical losses of our system on the noise floor. For an overcoupled cavity where the intrinsic losses through any channel other than the input port are negligible, the cavity losses would approximately be of the same order as the loss at the detection port. Thus here, we investigate only the effects of the loss at the detection port. We determine the effect of adding vacuum noise at the output port of the beamsplitter used in

homodyne detection. This can be represented by the following phase and amplitude measurement output,

$$\begin{aligned} Y_{\text{out}} &= Y' \cos(\eta) + Y'_{\text{in}} \sin(\eta), \text{ and} \\ X_{\text{out}} &= X' \cos(\eta) + X'_{\text{in}} \sin(\eta) \end{aligned} \tag{5.10}$$

where η^2 quantifies the loss percentage in the system. Here Y'_{in} and X'_{in} are the input vacuum noise quadratures. We now focus on measuring the combination of the modified output phase and amplitude quadratures

$$X_{\theta,\text{out}} = Y_{\text{out}} \cos\theta + X_{\text{out}} \sin\theta \cdot \tag{5.11}$$

By applying the same noise analysis as in the previous section, we demonstrate that the benefits of squeezing persist even at optical losses expected in experiments (see Fig. 5.1d-e).

5.2.2 Two-mode Squeezing Toy Model

In this section, we consider using two-mode squeezed light to continuously monitor the position of an optomechanical system. We find that for an approximate two-mode interaction, all the benefits expected from the single-mode case can be realized. Our system comprises a two-sided optical cavity with a pendulous mirror centered between two fixed mirrors as seen in the schematic diagram of Fig. 5.2a and the proposed experimental implementation of Fig. 5.3b. When the two modes are incident on opposite sides of the pendulous mirror with equal power,

the interaction Hamiltonian is

$$H_{\text{int}} = \hbar G x (X_1 - X_2), \tag{5.12}$$

where X_i is the amplitude quadrature of light for the ith mode. We now evaluate a toy model where two modes drive our backaction induced measurement system. In a manner analogous to the single-mode case, these dynamics can be characterized by applying the following chain of unitaries to the system,

$$U_{\text{int}} U_{\text{free}} U_{\text{int}} = e^{-i\zeta x_0 (X_1 - X_2)} e^{-i\beta \frac{p_0^2}{2}} e^{-i\zeta x_0 (X_1 - X_2)}. \tag{5.13}$$

Consequently, the following operators transform to,

$$\begin{aligned} U_{\text{int}}^\dagger p_0 U_{\text{int}} &= p_0 - \zeta (X_1 - X_2), \\ U_{\text{int}}^\dagger Y_1 U_{\text{int}} &= Y_1 - \zeta x_0, \\ U_{\text{int}}^\dagger Y_2 U_{\text{int}} &= Y_2 + \zeta x_0, \text{ and} \\ U_{\text{free}}^\dagger x_0 U_{\text{free}} &= x_0 + \beta p_0. \end{aligned} \tag{5.14}$$

Similar to the single-mode case, the remaining transformations do not change the operators since X_i, Y_i, and p_0 commute with U_{free} and x_0, and X_i commute with U_{int}. Under standard homodyne detection schemes, we have access to sums or differences of the quadratures, X_i and Y_i where i denotes the modes. We consider the arbitrary combination of differences in the X_i' and Y_i' quadratures between the output modes

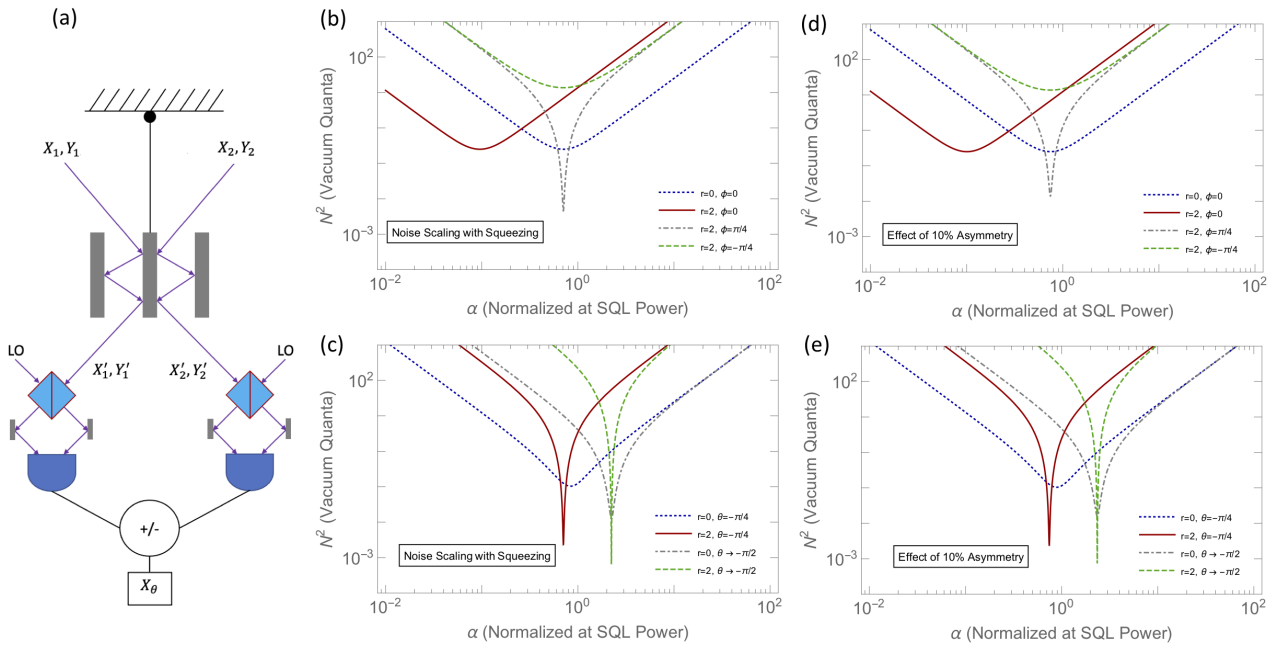

Figure 5.2: Position measurements using two-mode squeezed light. a) A position measurement comprising a two-sided optomechanical system probed with two-mode squeezed light with quadratures X_1, X_2 and Y_1, Y_2. In this proposed scheme the measured quadrature X_θ is read out using homodyne detection by interfering the outputs with their local oscillators (LO). b) Phase difference quadrature measurement ($\theta = 0$) at squeezing strengths $r = 0, 2$ and squeezing angles $\phi = 0, \pm\pi/4$. The displacement amplitude α is normalized at the power required to reach the SQL for the single-mode (in Fig 5.1) for comparison. The optimal noise floor for measuring the phase difference quadrature with $r > 0$ occurs at $\phi = \pi/4$, while at $\phi = 0$ squeezing provides a reduced power to attain the same noise floor. c) Noise for measurement quadratures $\theta = -\pi/4, -\pi/2$ where the optimal noise floor occurs at $\theta = -\pi/2$, effectively an amplitude difference quadrature measurement. d) Effect on phase difference quadrature measurement due to asymmetry in the power incident on the two-sided cavity with $\alpha_2 = 0.9\,\alpha_1$. e) Effect of power asymmetry on quadrature measurements $\theta = -\pi/4, -\pi/2$.

$$
\begin{aligned}
X_\theta &= \cos\theta(Y_1' - Y_2') + \sin\theta(X_1' - X_2'), \\
&= (\Delta Y - 4\zeta x_0 - 2\zeta\beta p_0 + 2\zeta^2\beta\Delta X)\cos\theta + \Delta X \sin\theta,
\end{aligned}
\tag{5.15}
$$

where $\Delta Y = Y_1 - Y_2$ and $\Delta X = X_1 - X_2$ are the phase difference quadrature and amplitude difference quadrature, respectively. Similar to the single-mode case, we find shot noise terms

independent of ζ, signal terms proportional to ζ and backaction term proportional to ζ^2. The estimator variable for measuring the position can be obtained by dividing the above quadrature through the multiplicative factor of x_0 in Eq. 5.15,

$$\begin{aligned} x_E &= X_\theta/(-4\zeta\cos\theta) \\ &= -\frac{1}{4\zeta}\Delta Y + x_0 + \frac{\beta p_0}{2} - \frac{\zeta\beta}{2}\Delta X - \frac{\tan\theta}{4\zeta}\Delta X. \end{aligned} \tag{5.16}$$

As in the single-mode case, we only consider the measurement-induced noise terms from the light quadratures. Yet again, we can select a θ in Eq. 5.16, to negate the X_i quadratures from adding backaction induced noise to the system. Similar to the single-mode case, we see that the selection of the θ which minimizes the backaction term is dependent on power (α^2). The noise metric $N^2 \propto (x_E - (x_0 + \beta p_0/2))^2$ for the two-mode case may be expressed as

$$N^2 = \frac{1}{16\zeta^2}(\Delta Y + 2\zeta^2\beta\Delta X + \Delta X\tan\theta)^2. \tag{5.17}$$

We now consider the effect of applying a squeezed two-mode vacuum to our two-sided cavity. For two-mode squeezed light, we see again that we have cross-correlation terms that are non-zero. The relevant vacuum expectation values comprising the amplitude difference and phase difference quadratures for two-mode squeezed light can be represented as,

$$\begin{aligned} \langle\Delta X^2\rangle &= e^{2r}\cos^2\phi + e^{-2r}\sin^2\phi, \\ \langle\Delta Y^2\rangle &= e^{-2r}\cos^2\phi + e^{2r}\sin^2\phi, \text{ and} \\ \langle\{\Delta X, \Delta Y\}\rangle &= (e^{-2r} - e^{2r})\sin 2\phi, \end{aligned} \tag{5.18}$$

with the individual quadrature correlations represented as,

$$\begin{aligned}
\langle X_1^2\rangle = \langle Y_1^2\rangle = \langle X_2^2\rangle = \langle Y_2^2\rangle &= \frac{1}{2}\cosh(2r), \\
\langle X_1 Y_1\rangle = \langle X_2 Y_2\rangle &= 0, \\
\langle X_1 Y_2\rangle = \langle X_2 Y_1\rangle &= \frac{1}{2}\sinh(2r)\sin(2\phi), \text{ and} \\
\langle X_1 X_2\rangle = -\langle Y_1 Y_2\rangle &= -\frac{1}{2}\sinh(2r)\cos(2\phi).
\end{aligned} \tag{5.19}$$

From the above correlations we observe that the cross-terms can be made negative by choosing an appropriate squeezing angle and boosting the squeezing strength, to lower the noise floor for position measurements , as was the case for single-mode squeezed vacuum. In Figs. 5.2b-c we show that two-mode squeezed light is an alternative squeezing modality that may be used in position measurements providing the same noise floor with the same dependencies on the squeezing parameter r, squeezing angle ϕ, and quadrature angle θ as in the single-mode case discussed above. In the two-mode case, we are using twice the amount of power compared to the single-mode case as both of the modes have equal amplitude. Thus, in the plot we notice that the optimal power requirement has reduced by a factor of half which is essentially equivalent to the single-mode case. We find that, at a squeezing angle of $\phi = 0$, squeezing reduces the power required to access the SQL for our system (see Fig. 5.2b). Similar to the single-mode case we see that for a squeezing angle of $\phi = \pi/4$ and a non-zero squeezing strength the noise falls below the SQL near the original displacement amplitude α due to the negative contribution from the cross-correlator term given by the aforementioned parameters. We globally minimize the noise by optimizing the quadrature angle θ. The optimization gives us, $\theta_{opt} \rightarrow -\tan^{-1}(2\zeta^2\beta)$ which is strongly dependent on power, similar to the single-mode case. This suggests that using

this optimization at high power, we would measure the amplitude difference quadrature which is devoid of any signal, as in the single-mode case.

Two-mode squeezed light sources may have an asymmetry in the power of each mode. Additionally there may be mismatches in reflection coefficients for the two-sided cavity. As we will see, our toy model when driven by two-mode squeezed light or two coherent states, is robust to small amounts of asymmetries. If we account for a typical power asymmetry, we can modify the toy model as follows

$$\begin{aligned} U_{\text{meas}} U_{\text{free}} U_{\text{meas}} = e^{-ix_0(\zeta_1 X_1 - \zeta_2 X_2)} \\ e^{-i\beta \frac{p_0^2}{2}} e^{-ix_0(\zeta_1 X_1 - \zeta_2 X_2)}. \end{aligned} \tag{5.20}$$

To understand the impact of asymmetry we consider a specific example where the squeezing strength is $r = 2$ as seen in Figs. 5.2d-e. We find numerically that the expected asymmetry of the modes with displacement amplitudes α_1 and α_2 should not exceed $\alpha_2/\alpha_1 = 0.9$, as seen in Fig. 5.2d. As our example illustrates, the squeezing and quadrature angles may be tuned to partially recover the noise floors of the symmetric case as seen in Fig. 5.2d-e. We expect that as r increases the amount of allowed asymmetry decreases.

5.3 Practical Design: Single-Sided Cavity

With the intuition gained from our toy model, we investigate the benefits of squeezing in a single-sided optomechanical cavity as illustrated in Fig. 5.3a. The linearized interaction

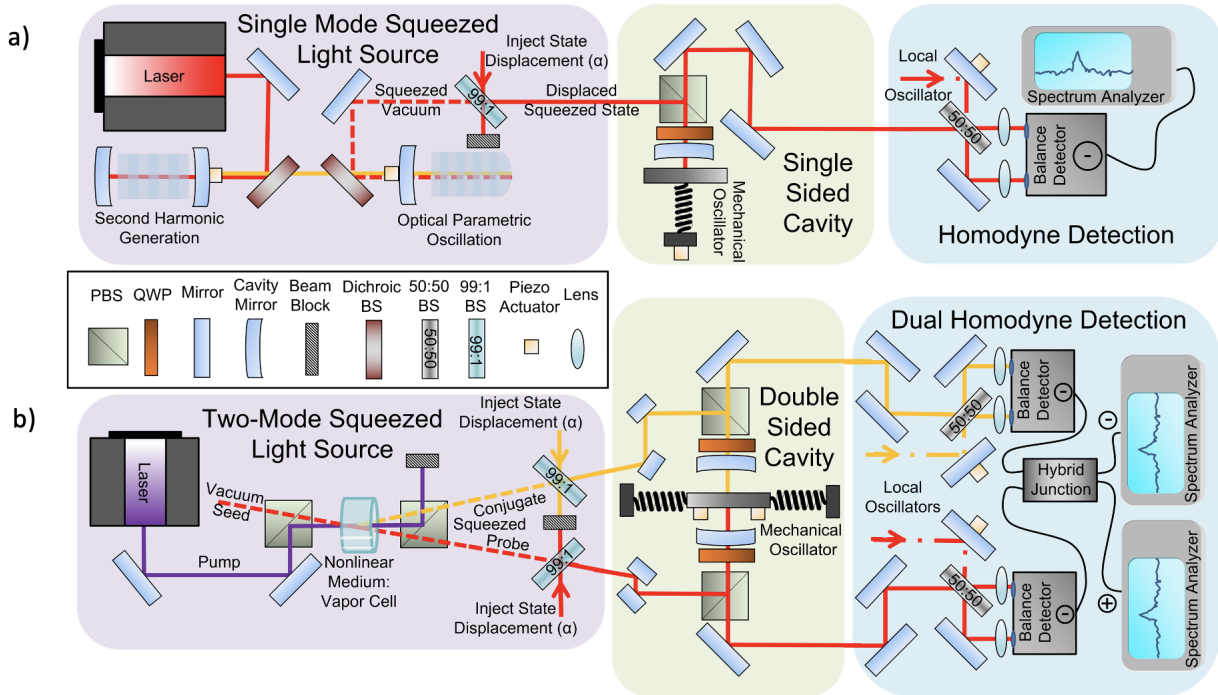

Figure 5.3: Experimental Vision: Schematics for a position measurement. a) A single-mode squeezed light source with displacement amplitude α injected after squeezing, is used to interrogate an unfixed mirror in an optical cavity. The phase sensitive signal is read out with homodyne detection. b) A two-mode squeezed light source with α injected onto the twin beams after squeezing, is used to interrogate an unfixed double-sided mirror in a double-sided optical cavity. The phase sensitive signal is read out with a joint measurement of the twin beams using dual homodyne detection.

Hamiltonian for the cavity is

$$H_{\text{int}} = \hbar G x X, \tag{5.21}$$

where G is the optomechanical coupling strength in frequency per length units and x is the position of the moving mirror. The Hamiltonian H_{tot} that describes the optomechanical system in the rotating frame of the drive with the detuning Δ is as follows,

$$
\begin{aligned}
H_{\text{tot}} &= H_{\text{cav}} + H_{\text{mech}} + H_{\text{int}} + H_{\text{bath}}, \\
H_{\text{cav}} &= -\hbar\Delta a^\dagger a, \text{ and} \\
H_{\text{mech}} &= \frac{1}{2}m\omega_m^2 x^2 + \frac{p^2}{2m},
\end{aligned}
\tag{5.22}
$$

where H_{cav}, H_{mech}, and H_{bath} are the Hamiltonian terms for the optical cavity, the mechanical oscillator and the bath coupled to the system respectively. The parameters m and p are the mass and momentum of the moving mirror, respectively, in our system and ω_m is the mechanical resonance frequency. On resonance with the drive, $\Delta = 0$, the cavity Heisenberg-Langevin equations of motion are

$$
\begin{aligned}
\dot{X} &= -\frac{\kappa}{2}X + \sqrt{\kappa}X_{\text{in}}, \\
\dot{Y} &= -Gx - \frac{\kappa}{2}Y + \sqrt{\kappa}Y_{\text{in}}, \\
\dot{p} &= -\hbar GX - \gamma p + F_{\text{in}} - m\omega_m^2 x, \text{ and} \\
\dot{x} &= \frac{p}{m},
\end{aligned}
\tag{5.23}
$$

where κ is the cavity decay rate, X_{in} and Y_{in} are the quadratures input to the system, F_{in} is the external force acting on the resonator, and γ is the mechanical damping rate. The bath operators are expressed in terms of the input fields [37, 38]. The output quadratures are related to the input quadratures by the input-output relations

$$
\begin{aligned}
X_{\text{out}} &= X_{\text{in}} - \sqrt{\kappa}X, \text{ and} \\
Y_{\text{out}} &= Y_{\text{in}} - \sqrt{\kappa}Y.
\end{aligned}
\tag{5.24}
$$

We determine X_{out} and Y_{out} in terms of the input fields. This analysis is done in the frequency domain by solving for all the variables X, Y, x, p in terms of the input fields $X_{\text{in}}, Y_{\text{in}}$ and F_{in}. We then apply input-output relations to write down the expressions for $X_{\text{out}}, Y_{\text{out}}$ as

$$\begin{aligned} X_{\text{out}} &= e^{i\phi_c} X_{\text{in}}, \text{ and} \\ Y_{\text{out}} &= e^{i\phi_c} Y_{\text{in}} + G\chi_c\chi_m \left[F_{\text{in}} - \hbar G \chi_c X_{\text{in}}\right]. \end{aligned} \tag{5.25}$$

The cavity response function χ_c, the mechanical response function χ_m and the cavity phase shift $e^{i\phi_c}$ are,

$$\begin{aligned} \chi_c &= \frac{\sqrt{\kappa}}{-i\nu + \kappa/2}, \\ \chi_m &= \frac{-1}{m(\nu^2 - \omega_m^2 + i\gamma\nu)}, \text{ and} \\ e^{i\phi_c} &= \frac{-i\nu - \kappa/2}{-i\nu + \kappa/2}. \end{aligned} \tag{5.26}$$

We define the measurement quadrature output from the system as

$$X_\theta = Y_{\text{out}} \cos\theta + X_{\text{out}} \sin\theta. \tag{5.27}$$

By inspection of Eqs. 5.25 and 5.27 we obtain the estimator variable for the input force F_E, by dividing the output quadrature with the coefficient of the input force term $G\chi_c\chi_m cos\theta$,

$$
\begin{aligned}
F_E &= \frac{X_\theta}{G\chi_c\chi_m\cos\theta} \\
&= \left[\frac{e^{i\phi_c}\tan\theta}{G\chi_c\chi_m} - G\hbar\chi_c\right] X_{\text{in}} + \frac{e^{i\phi_c}Y_{\text{in}}}{G\chi_c\chi_m} + F_{\text{in}}.
\end{aligned}
\tag{5.28}
$$

We determine the two point correlation function $\langle F_E(\nu)F_E(\nu')\rangle$ for F_E since $\langle F_E(\nu)F_E(\nu')\rangle$ is proportional to the noise power spectral density (PSD) $S_{FF}(\nu)$ as

$$
\langle F_E(\nu)F_E(\nu')\rangle = S_{FF}(\nu)\delta(\nu+\nu'). \tag{5.29}
$$

Understanding how to optimize the frequency-dependent power spectral density allows us to facilitate an intelligent search for a monochromatic or broadband signal. For a monochromatic signal, a frequency-dependent optimization of the PSD is required to obtain the maximum sensitivity. On the other hand, the optimized signal to noise ratio for a broadband signal corresponds to the noise PSD integrated over a bandwidth of interest. For this case, an optimization over a broad frequency range would be necessary to obtain maximum sensitivity.

To consider the contributions to the noise, we focus on the quantity $\langle F_E^2\rangle$. In the limit where the mechanical decay rate γ is much smaller than the other frequency scales ($\gamma \ll \omega_m, \kappa$), the γ-dependent imaginary term of the cross-correlator may be neglected to obtain the following expression

$$
\begin{aligned}
\langle F_E^2\rangle = &\left|\frac{e^{i\phi_c}\tan\theta}{G\chi_c\chi_m} - G\hbar\chi_c\right|^2 \langle X_{\text{in}}^2\rangle + \left|\frac{1}{G\chi_c\chi_m}\right|^2 \langle Y_{\text{in}}^2\rangle \\
&+ \left[\hbar m(\omega_m^2-\nu^2) + \frac{\tan\theta}{G^2|\chi_c|^2|\chi_m|^2}\right]\langle\{X_{\text{in}}, Y_{\text{in}}\}\rangle \\
&+ \langle F_{\text{in}}^2\rangle .
\end{aligned}
\tag{5.30}
$$

To optimally reduce the noise, we minimize $\langle F_E^2 \rangle$ with respect to the quadrature angle θ which reduces the backaction noise. Prior to minimizing the noise we fix the squeezing angle ϕ to zero. This reveals the optimized quadrature angle

$$\theta_{\text{opt}} \to \tan^{-1}\left[\hbar G^2 m |\chi_c|^2 |\chi_m|^2 (\nu^2 - \omega_m^2)\right]. \tag{5.31}$$

By inspecting Eq. 5.31 we see that θ_{opt} is strongly dependent on power ($G^2 \propto \alpha^2$) and frequency. In the limit of high power and low frequency, $\theta_{\text{opt}} = \pi/2$ which corresponds to measuring the amplitude quadrature X which is devoid of any signal from F_{in}. But in the high frequency limit θ_{opt} approaches 0, allowing us to measure our signal at an optimally low noise floor. Our objective is to minimize the measurement-induced noise terms $N(\nu)$ of $\langle F_E^2 \rangle$, so we only consider $N(\nu)$ for the remainder of the section. While the thermal contribution to the noise may be reduced as discussed in [21], it is not the focus of this article. At the optimal quadrature angle and in the low γ limit, the measurement-induced noise $N(\nu)$ for an arbitrary squeezing angle ϕ simplifies to

$$N(\nu) = \frac{e^{-2r}\cos^2\phi + e^{2r}\sin^2\phi}{2G^2|\chi_c|^2|\chi_m|^2}. \tag{5.32}$$

Only the shot noise term is present in Eq. 5.32 since at $\theta \to \theta_{\text{opt}}$ the backaction term of $N(\nu)$ cancels out as $\gamma \to 0$. Here the optimal choice for squeezing angle is $\phi = 0$. With these parameters, the quantum noise is

$$
\begin{aligned}
N(\nu) &= \frac{e^{-2r}}{2G^2|\chi_c|^2|\chi_m|^2} \\
&\approx \frac{e^{-2r}m^2(\kappa^2/4+\nu^2)(\nu^2-\omega^2)^2}{2G^2\kappa}.
\end{aligned}
\tag{5.33}
$$

As an alternative to the previous approach, by restricting ourselves to phase quadrature measurements, we may optimize $N(\nu)$ with respect to power. A power optimization at $\phi = 0$ leads to a target frequency-dependent coupling strength G,

$$
G(\nu) \to \frac{e^{-r}}{\sqrt{\hbar}|\chi_m(\nu)|^{1/2}|\chi_c(\nu)|}. \tag{5.34}
$$

which demonstrates that when squeezing is present and the squeezing angle is zero the optimum power requirements to access the same noise floor are reduced, consistent with our toy model. Moreover, when we measure the phase quadrature while operating at the original optimized coupling strength as in the without squeezing case, a contribution to the total noise will be from the sum of the balanced shot noise and backaction noise terms. This sum is equivalent to the SQL. The additional contribution is from the cross-correlator term (the third term in Eq. 5.30). Careful selection of the squeezing angle ϕ, will force the cross-correlator term to negatively contribute to the total noise expression, thus reducing the overall noise. Under these conditions, in the $\gamma \to 0$ limit, the total measurement-induced noise is represented as

$$
N(\nu) = \hbar m(\nu^2 - \omega_m^2)(\cosh 2r + \sinh 2r \sin 2\phi). \tag{5.35}
$$

Equation 5.35 reveals that the measurement-induced noise is minimized by squeezing when the

squeezing angle is tuned to $\phi = -\pi/4$.

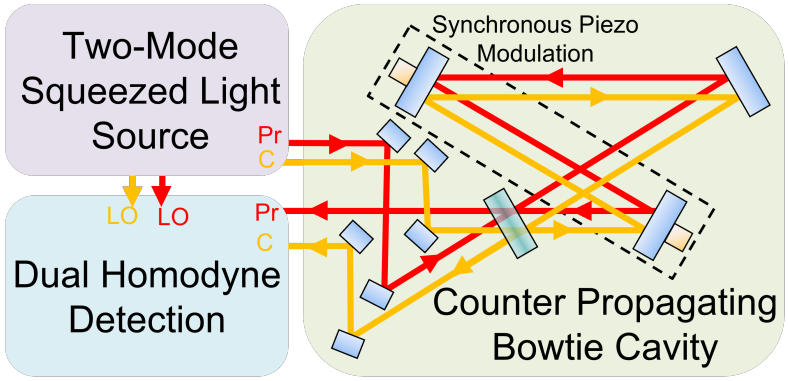

Figure 5.4: A momentum measurement where a bowtie cavity is probed by the counter-propagating modes of two-mode squeezed light. The modes enter the cavity through a beamsplitter. The phase sensitive measurement interferes the squeezed modes with their local oscillators within dual homodyne detectors (as in Fig 5.3.b), enabling a momentum measurement imparted from a pair of synchronously modulated mirrors. The spatial modes may be overlapped by cross-polarizing the modes and using polarizing beamsplitters for injecting and collecting light from the cavity.

5.4 Combining Backaction Evasion and Squeezing

5.4.1 Continuous Momentum Measurement

In this section we consider a backaction evading model achieved by approaching a quantum non-demolition measurement of momentum, where we continuously monitor the momentum rather than the position of an optomechanical system using single-mode squeezed light. Momentum is effectively a QND variable while working in the free particle limit [45]. In our model, the light interacts directly with the mechanical momentum which is proportional to the velocity of the movable mirror in the system above rather than the position. Thus the

interaction Hamiltonian is dependent on the momentum,

$$H_{\text{int}} = \hbar G' p X, \tag{5.36}$$

where G' is the optomechanical coupling strength in units of frequency over momentum. While this interaction cannot be directly generated by the single-sided optomechanical cavity discussed in the last section, there are some practical designs of optomechanical systems as described in the set-up of [36], as well as particular electromechanical couplings which essentially showcase the type of interaction described in Eq. 5.36. Furthermore, two-mode squeezed light can enable an experimental realization for a momentum measurement as described in Fig. 6.3 where the twin beams of two-mode squeezed light counter propagate through a bowtie cavity. We focus the remainder of this section on the benefits of a momentum based interaction and we do not consider its practical implementation any further. For the interaction Hamiltonian in Eq. 5.36, the Heisenberg-Langevin equations of motion are

$$\begin{aligned}
\dot{X} &= -\frac{\kappa}{2}X + \sqrt{\kappa}X_{\text{in}}, \\
\dot{Y} &= -G'p - \frac{\kappa}{2}Y + \sqrt{\kappa}Y_{\text{in}}, \\
\dot{p} &= -\gamma p + F_{\text{in}} - m\omega_m^2 x, \text{ and} \\
\dot{x} &= \frac{p}{m} + \hbar G' X.
\end{aligned} \tag{5.37}$$

The input and output quadratures for the optical fields are related by the input-output relations [37, 38]

$$
\begin{aligned}
X_{\text{out}} &= X_{\text{in}} - \sqrt{\kappa} X, \text{ and} \\
Y_{\text{out}} &= Y_{\text{in}} - \sqrt{\kappa} Y.
\end{aligned}
\tag{5.38}
$$

We solve for the output quadratures in terms of the input quadratures as was done in Eq. 5.25 in the previous section. They are expressed as

$$
\begin{aligned}
X_{\text{out}} &= e^{i\phi_c} X_{\text{in}}, \text{ and} \\
Y_{\text{out}} &= e^{i\phi_c} Y_{\text{in}} - iG' \chi_c \chi_m m \nu F_{\text{in}} \\
&\quad - \hbar m^2 \omega_m^2 G'^2 \chi_c^2 \chi_m X_{\text{in}}.
\end{aligned}
\tag{5.39}
$$

As in the previous section, to estimate the force acting on the system, we divide a particular combination of the phase and amplitude quadrature as in Eq. 5.27 by the multiplicative factor for F_{in}, resulting in the force estimator variable

$$
\begin{aligned}
F_E &= \frac{X_\theta}{-iG' \chi_c \chi_m m \nu \cos\theta}, \\
&= \left(\frac{i e^{i\phi_c} \tan\theta}{G' m \nu \chi_c \chi_m} - iG' \hbar \chi_c m \frac{\omega_m^2}{\nu} \right) X_{\text{in}} \\
&\quad + \frac{i e^{i\phi_c}}{G' m \nu \chi_c \chi_m} Y_{\text{in}} + F_{\text{in}}.
\end{aligned}
\tag{5.40}
$$

Our interest is in the contribution of the measurement-induced noise to the total noise PSD. To investigate the contributions to the noise PSD, we determine the two point correlation function of the estimator force variable as in the previous section

$$
\begin{aligned}
\langle F_E^2 \rangle = & \left| \frac{ie^{i\phi_c}\tan\theta}{G' m\nu\chi_c\chi_m} - iG'\hbar\chi_c m\frac{\omega_m^2}{\nu} \right|^2 \langle X_{\text{in}}^2 \rangle \\
& + \left| \frac{ie^{i\phi_c}}{G' m\nu\chi_c\chi_m} \right|^2 \langle Y_{\text{in}}^2 \rangle + \langle F_{\text{in}}^2 \rangle \\
& \left[\hbar m\frac{\omega_m^2}{\nu^2}(\omega_m^2 - \nu^2) + \frac{\tan\theta}{m^2\nu^2 G'^2|\chi_c|^2|\chi_m|^2} \right] \langle \{X_{\text{in}}, Y_{\text{in}}\} \rangle .
\end{aligned} \tag{5.41}
$$

Note that there is no backaction noise in the limit where the mechanical frequency $\omega_m \to 0$, indicating the system is in the free particle limit. Fixing $\phi = 0$, from Eq. 5.41 we find the optimal quadrature angle which minimizes the noise

$$
\theta_{opt} \to \tan^{-1}\left[\hbar G'^2 m^3 \omega_m^2 |\chi_c|^2 |\chi_m|^2 (\nu^2 - \omega_m^2) \right] . \tag{5.42}
$$

In the limit of $\omega_m \to 0$, the noise is minimized by measuring the phase quadrature corresponding to $\theta_{\text{opt}} = 0$. Under these conditions, the backaction term is canceled leaving only the shot noise term to contribute to the measurement-induced noise. Thus at $\theta \to \theta_{\text{opt}}$, in the low γ and free particle limit, the measurement-induced noise takes the form

$$
N(\nu) = \frac{e^{-2r}\nu^2(\cos^2\phi + e^{4r}\sin^2\phi)}{2G'^2|\chi_c|^2}. \tag{5.43}
$$

Since G'^2 is proportional to power, an increase in the power will monotonically lower the noise floor. Squeezing can further minimize the measurement-induced noise for momentum sensing. By inspecting Eq. 5.43, we find that under these conditions, the optimal squeezing angle to lower the measurement-induced noise is $\phi = 0$. As in the case of position sensing, if we focus

on the alternative approach where we only measure the phase quadrature, we can also optimize the measurement-induced noise with respect to power and obtain a target frequency-dependent coupling strength

$$G'(\nu) \to \frac{e^{-r}}{m\omega_m\sqrt{\hbar}|\chi_m(\nu)|^{1/2}|\chi_c(\nu)|}, \tag{5.44}$$

where the squeezing lowers the necessary power to attain a given noise floor. Using the original optimized power when squeezing is not present as an input into the total noise expression Eq. 5.41, we obtain the noise contributions from the SQL equivalent noise and the cross-correlator terms. Similar to the toy model and the position sensing scheme presented above, we see that by tuning the squeezing angle to $\phi = -\pi/4$, we force the cross-correlator term to be negative, thereby reducing the total noise. At the $\gamma \to 0$ limit, the measurement-induced noise expression in this case can be represented as,

$$N(\nu) = \hbar m \frac{\omega_m^2}{\nu^2}(\nu^2 - \omega_m^2)(\cosh 2r + \sinh 2r \sin 2\phi). \tag{5.45}$$

5.4.2 Comparisons

For position sensing, the coupling strength G scales as the frequency over the cavity length. For momentum sensing, the coupling constant G' scales as the frequency over momentum. For each technique, during measurement we coherently integrate the signal over the cavity lifetime. The momentum coupling strength G' is then related to G by the factor $1/(m\kappa)$ where m is the mass of the mechanical sensor and κ is the cavity decay rate. We also choose $1/\kappa$ as it is the natural scale in [36]. We begin by comparing the optimum quadrature angle that maximizes the signal-to-noise for the position and momentum sensing techniques. To compare the optimal

quadrature angles, the coupling strengths G and G' are chosen to produce the same power in both techniques. In Fig. 5.5a, we see that for a fixed value of G (corresponding to an input power of around 0.1 mW for a 1 cm cavity), the optimal quadrature for position sensing at low frequencies is the amplitude quadrature and at higher frequencies it is the phase quadrature. Whereas, under the same conditions, for momentum sensing we should optimally measure the phase quadrature across a broadband frequency spectrum. By fixing the frequency (here $\nu = 10$ kHz), we find that in Fig. 5.5b, the optimal quadrature for position sensing deviates from the phase quadrature at much lower powers than in the momentum sensing case.

To compare the performance of the position and momentum sensing protocols, we must first distinguish between the relevant search strategies for specific signals. For dark matter detection, we distinguish between a monochromatic signal such as the coherent field generated by ultralight dark matter candidates [50] and broadband impulse signals expected in heavy dark matter candidates [21]. For the monochromatic signal, the exact frequency is unknown and consequently we consider narrow-band or resonant search strategies. For a heavy dark matter search including long-range interactions, the target frequency band is 1-10 MHz for the expected rapid impulse signal, where we consider a broadband search.

We begin our calculation for broadband search effectiveness by choosing the phase quadrature and optimally tuning the target laser power, corresponding to tuning the optomechanical coupling at a fixed target band center on the order of $\sim$ 1 MHz. We ensure that the coupling strengths for the momentum and the position sensing techniques are chosen such that for each technique the same target power is used during the broadband search. As represented in Fig. 5.6, we show the potential benefits of squeezing while operating at the same power. For the position sensing case, we are backaction limited at lower frequencies since

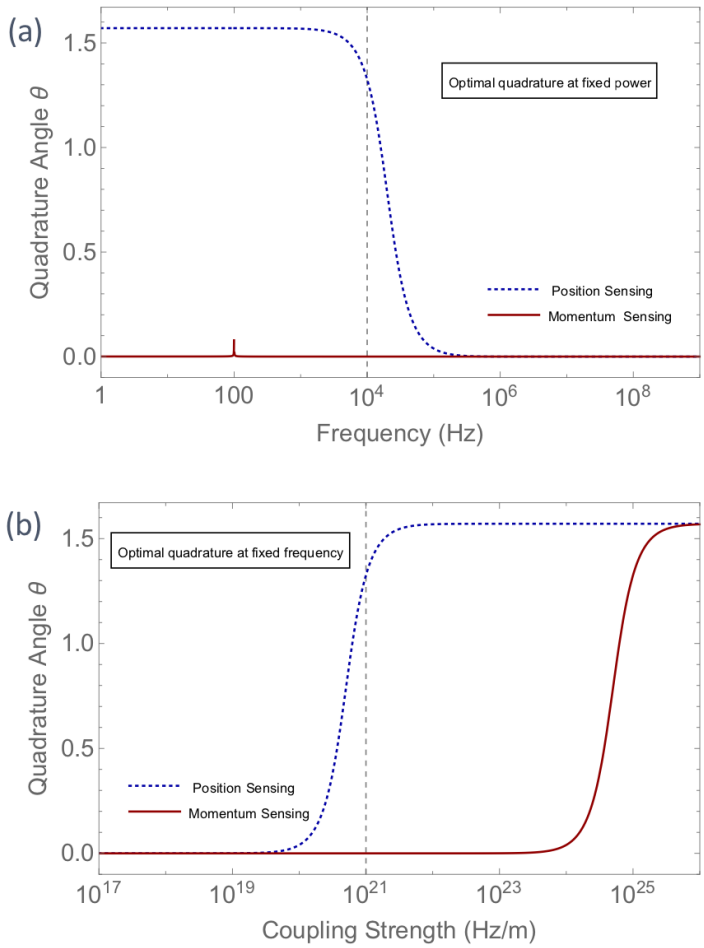

Figure 5.5: Optimal quadrature angle comparison between position sensing (Eq. 5.31) and momentum sensing (Eq. 5.42). a) Optimal quadrature angle plotted as a function of the frequency. The parameters used are the same as in Fig. 5.6 other than the coupling strength G which is fixed at $10^{21}\mathrm{Hz/m}$ and $G' \to G/m\kappa$. Position sensing has $|\theta| \to \pi/2$ at lower frequency and $|\theta| \to 0$ at higher frequency whereas for momentum sensing $|\theta| \to 0$ for a broad spectrum. b) Optimal quadrature angle plotted as a function of the power. Here the frequency has been fixed at $\nu \to 10$ kHz. We see that $|\theta|$ starts to deviate from 0 at much lower power for position sensing than momentum sensing.

we are operating at high input power $P \sim 1$ W. We need this higher power when compared to the $\nu = 10$ kHz case due to the much high frequency band-center. However, squeezing only provides a benefit at higher frequencies where we are shot noise limited. For momentum sensing, at frequencies below the mechanical resonance ω_m, backaction dominates, so squeezing provides no improvement. Then backaction noise diminishes at higher frequencies than the mechanical

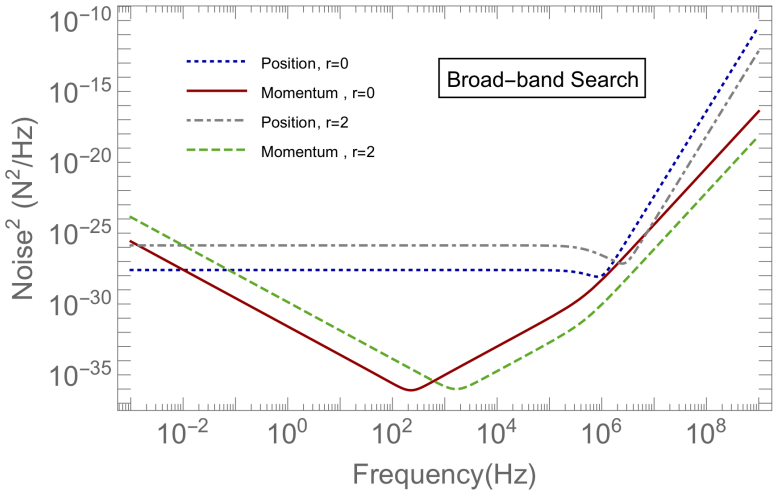

Figure 5.6: Broadband search strategy for position and momentum sensing. The phase quadrature noise is plotted for both sensing protocols while operating at the optimal power for position sensing with a 1 MHz target (using Eq. 5.34 at r=0, $\nu = 1$ MHz) . The same power is used for the squeezed scenario. The optomechanical coupling strengths in these techniques are related by $G' \to G/(m\kappa)$ with mechanical frequency $\omega_m = 100$ Hz, cavity decay rate $\kappa = 1$ MHz, mirror mass $m = 1$ mg, damping rate $\gamma = 0.1$ mHz, and squeezing angle $\phi = 0$. The noise for momentum sensing is lower than position sensing across a broad frequency range. At fixed power squeezing lowers the noise in the shot noise dominated region for both sensing protocols.

resonance ω_m, where we are shot noise limited. Hence, for momentum sensing, squeezing can significantly lower the noise in the regime of $\nu > \omega_m$. Additionally, we see that momentum sensing is more advantageous than position sensing for broadband detection as momentum sensing has a lower noise while operating at a fixed input power, especially for $\nu > \omega_m$.

We now describe the narrow-band search and its sensitivity as shown in Fig 5.7. Here we assume that the mechanical oscillator frequency is fixed. We begin the search by tuning the input power P at every frequency such that we set the noise floor to the SQL across the frequency spectrum. Simultaneously, at every frequency we select the optimal quadrature angle, in order to remove the backaction noise. We compare implementing our narrow-band search with ($r = 2$) and without ($r = 0$) using squeezed light, where the power used in each case is the same. Note that for the same power, squeezing lets us achieve a lower noise floor in both position and the

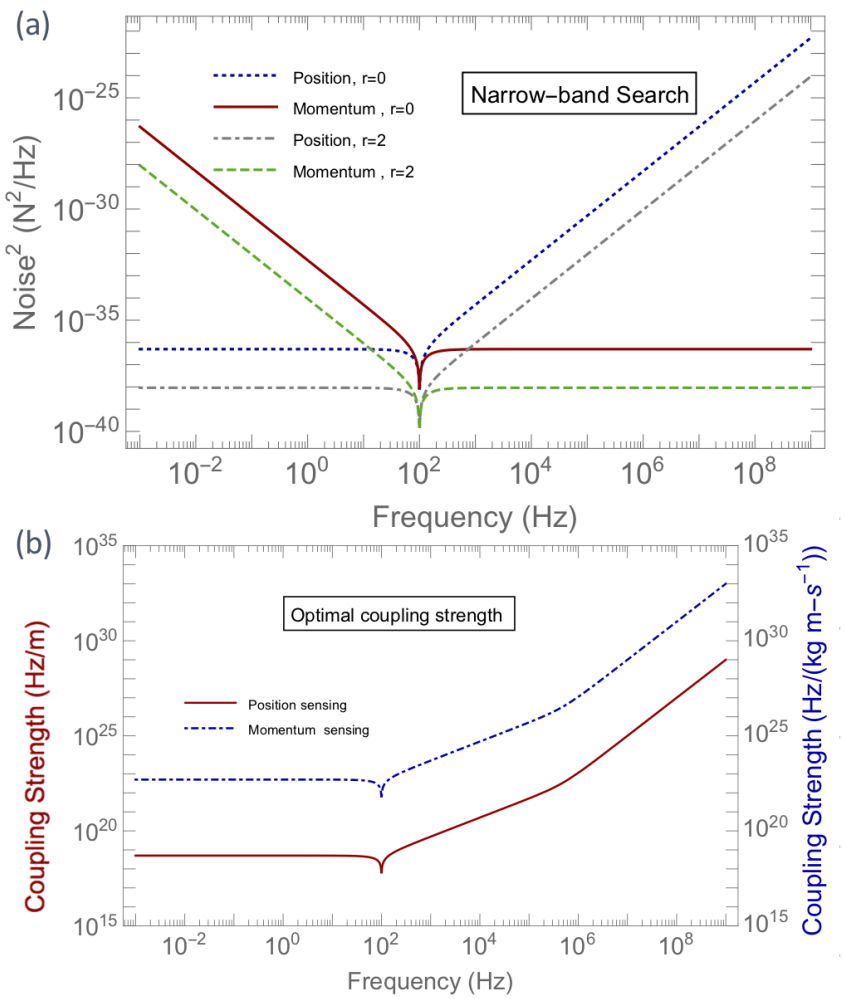

Figure 5.7: a) Narrow-band search strategy for position and momentum sensing. The noise is plotted for both techniques at the optimal power (Eqs. 5.34 , 5.44 at $r = 0$) and optimal quadrature angle (Eqs. 5.31, 5.42) for each frequency with a mechanical frequency $\omega_m = 100$ Hz, cavity decay rate $\kappa = 1$ MHz, sensor mass $m = 1$ mg, damping rate $\gamma = 0.1$ mHz, and squeezing angle $\phi = 0$. The optimal noise floor is lower in momentum sensing than position sensing when $\nu > \omega_m$. Squeezing at the same power lowers the noise floor. b) The optimal coupling strength dependence on frequency.

momentum sensing. By selecting the optimum quadrature the backaction term is eliminated and the remaining shot noise is reduced using squeezed light. For the position sensing case, we see that at frequencies below the mechanical frequency ($\nu \ll \omega_m$), the noise is proportional to $\hbar m \omega_m^2$ and is independent of frequency. The noise remaining constant across frequency in this scenario,

is due to selecting an optimal G. In the same regime for momentum sensing, the noise goes as $1/\nu^2$. The opposite is true when $\nu \gg \omega_m$ while operating at optimized powers, where the noise is flat for momentum sensing while the noise goes as ν^2 for position sensing. This characteristic can be attributed to the fact that the optimized noise in the momentum sensing technique is related to the optimized noise in the position sensing technique by a factor of ω_m^2/ν^2. Hence, for frequencies well above the mechanical frequency, we find the momentum sensing to be more advantageous than position sensing. With squeezing, the overall noise reduces in both cases by a constant factor dependent on the squeezing strength. While we see no particular improvement in the minimum noise attainable on resonance, we do see an improvement in the noise floor across off-resonance frequency regimes, for both the techniques through the narrow-band search strategy. This is in addition to the benefit from squeezing in achieving the same noise floor at a lower power.

5.5 Outlook

In this article, we have explored how to go beyond the SQL for optomechanical sensors using squeezing, backaction evasion, and QND techniques. From our toy model and our practical cavity example, we confirm that squeezing reduces the power needed to achieve a given noise floor for position sensing. We also examined a QND momentum sensing protocol using a momentum coupling model, which shows equal benefits from squeezing in terms of power requirements. Critically, in the momentum sensing model at the free particle limit, as the backaction term goes to zero, we need to only measure the phase quadrature. Specifically, there is neither frequency nor power dependence to the optimal quadrature angle, thereby reducing the technical challenges of using squeezing in comparison to squeezed position sensing.

We have also explored search strategies for monochromatic and broadband signals. For broadband signals we determined that our momentum sensing model provides us with an improved noise floor over a broad frequency range. In both techniques, the noise floor is lowered in the shot noise dominated regime using squeezed light at the same operating power. For monochromatic signals, in the low frequency regime position sensing outperforms momentum sensing and at the high frequency regime we see the opposite. Furthermore, by using squeezed light we can achieve a lower noise floor for both protocols by optimally tuning the quadrature angle and power.

The quantum-enhanced sensing techniques presented in this article are especially useful in the context of direct dark matter detection as previously discussed. Our techniques may also be used in impulse metrology experiments such as sensing the collisions from background gas particles. In order to practically implement the momentum sensing technique, we can use specific designs of optomechanical system or an electrical system for readout. The electrical alternative is part of an ongoing work by some of the authors here and will be explored in a separate manuscript. The analysis in this article provides the key insight that we may reduce the noise floor for an optomechanical sensor by combining backaction evasion through a momentum measurement and squeezing. Moreover, the momentum sensing approach has advantages in terms of bandwidth and a reduction in technical noise caused by power fluctuations. We foresee that deploying these techniques would aid in reducing the measurement-induced noise floor for optomechanical sensors and would pave the way for extremely sensitive impulse detections.

Chapter 6: Readout Protocols in Microwave Domain

Parts of this chapter are from a manuscript in preparation with collaborators Brittany Richman, Daniel Carney, Gerard Higgins, Peter Shawhan, Christopher Lobb and Jacob M. Taylor. Some of the other content is part of a manuscript in preparation, with Jacob M. Taylor and contributions from the collaborators at the Windchime Project. [1]

6.1 Introduction

In this chapter we shift our focus from optical domain readout to microwave domain readout and demonstrate the QND measurements approach in the microwave domain.

Our results rely upon a few key observations. First, we recognize that the electromechanical coupling per photon is very similar in today's superconducting devices to the optomechanical coupling achieved in optical systems [123, 124] – but the factor of 100,000 reduction in energy per photon leads to dramatic reductions in total power necessary to get to the back-action limit, a necessary step for going beyond the SQL. Also, the superconducting devices are better choices in the context of environmental isolation. Secondly, we note that in the magnetomechanical regime, there is a natural way to couple to the velocity of a mechanical sensor which is a QND observable in the free particle limit. This is governed by a fundamental electromagnetic principle, Faraday's

[1] I have specifically contributed to the mathematical analysis of receivers and noise in the systems along with writing the noise analysis part of the manuscript.

law, which describes how a moving magnet generates an electromotive force depending on the rate of change of the flux. Even for an electromechanical system, we can directly access the velocity of the system by choosing a proper readout scheme, as we will show in this chapter. All these together motivated us to look for ways to perform measurements in the microwave domain and achieve noise reduction.

6.2 Power Requirement in Optical and Microwave Domain

Let us consider interrogating a test mass M with pulses of light. By the usual argument, our initial measurement imprecision leads to an uncertainty in the velocity post-measurement of $\frac{\hbar}{\Delta_x M}$ which in turn leads to a later uncertainty in position of $\frac{\hbar\tau}{\Delta_x M}$. The standard quantum limit for position measurement is found by setting this induced imprecision to be equal to the first pulse's imprecision [28], leading to

$$\Delta_{x,\mathrm{SQL}} \equiv \sqrt{\frac{\hbar\tau}{M}}. \tag{6.1}$$

The number of photons needed to achieve this SQL level resolution can be analysed as in section 2.1:

$$N_{\mathrm{SQL}} = \frac{L^2 M}{16 Q_c^2 \hbar\tau}. \tag{6.2}$$

For Windchime-relevant numbers [21, 22] we can consider a mass around a gram, a length scale around 10 μm, an optical quality $Q_c \sim 10^6$, and a time of 1 ms. This requires 10^{10} photons per pulse, or about a nJ with peak power of a mW. The corresponding imprecision is 10 attometers.

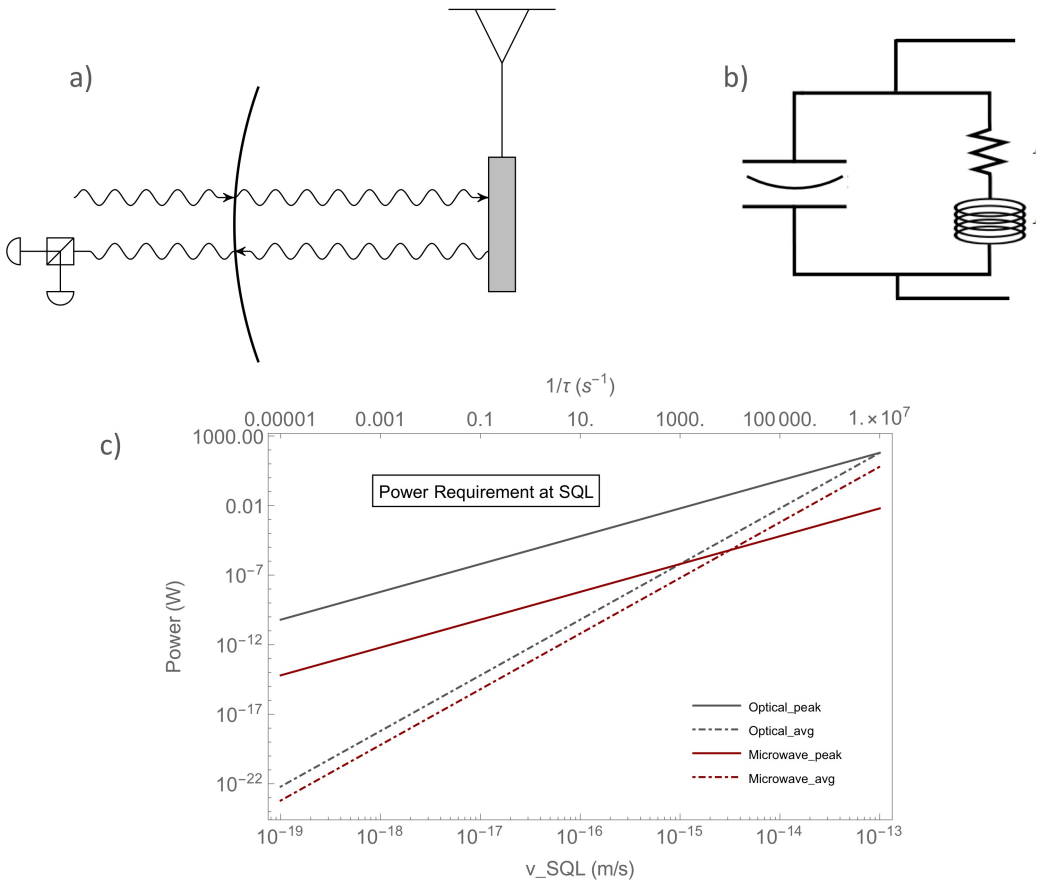

Figure 6.1: a) Schematic diagram of an optical cavity with a movable mechanical oscillator on one side where the cavity resonance frequency ω_c is set by the wavelength of light. b) Schematic diagram of a microwave cavity with a variable capacitance depending on the position of a mechanical membrane where the resonance frequency of the cavity ω_c is set by the value of the capacitance and inductance. c) Peak and average power requirement to reach the SQL, with the time in between measurements. Peak power is defined as $P \sim \kappa\hbar\omega_c N$ and avg power is defined by $P \sim (1/\tau)\hbar\omega_c N$. For optical domain, $\omega_c = 100$ THz, $\kappa = 1$ MHz and for microwave domain, $\omega_c = 1$ GHz, $\kappa = 10$ kHz, with lengthscale $L = 10\ \mu$m and the mass of the detector is taken to be proportional to a 1 cm detector with density 10^5 kg/m^3.

If we instead use an electromechanical setup, we can take advantage of the ability for capacitive structures to have a strong response to position. Specifically, for a microwave cavity with a re-entrant conductor or in the lumped element regime, small changes in the position of, e.g., a capacitive plate can lead to large changes in the resonant frequency [125–127]. As a

conservative estimate, we take $L^{-1} = \partial_x \log \omega_c \approx 0.1\ \mu\text{m}^{-1}$, which is comparable to the same parameter for the optical cavity.

Similarly, using superconducting systems enables us to maintain a high $Q_c \gtrsim 10^5$. We can work at 4-8 GHz with the cavity bandwidth $\kappa \sim 40$ kHz, which is still fast compared to $\tau = 1$ ms. However, while the total number of photons is similar for achieving SQL readout (here taking 10^{12} photons as the Q factor is 10 times worse), these photons are delivered over 25 μs rather than nanoseconds. Thus the peak power $\sim N\hbar\omega_c\kappa$ required is much lower:

$$P_{SQL,\mu\text{w}} \sim 10^{12}(2\pi\hbar \times 8\text{GHz})(40\ \text{kHz}) \approx 200\ \text{nW}$$

and the average power lower again by $1/\tau\kappa \sim 1/40$.

Thus, forgetting any other considerations except power, we see that using lower frequency light is highly advantageous if we can keep the system superconducting. Fortunately thermal noise requirements for measuring very small impulses will require working at dilution refrigerator temperatures, so superconductivity comes at no additional cost.

6.3 Velocity Sensing with Electro and Magneto-mechanical Systems

Now we explore the possibility of velocity measurements in the microwave domain with electro-mechanical and magneto-mechanical systems. Here we will adapt the language of voltage or current measurement as we focus on analysis in the lumped element equivalent circuit picture. In our upcoming manuscript, we discuss how in a magneto-mechanical voice-coil like configuration, the voltage is essentially proportional to the velocity of the mechanical system through Faraday's law:

$$\varepsilon = \oint_C (\mathbf{v} \times \mathbf{B}) \cdot \mathbf{dl} = 2\pi N R B_r v = T_v v \ , \tag{6.3}$$

where C is taken to be around the loops of the voice coil by integrating around the coil's N turns. The induced voltage is proportional to velocity via the transducer constant $T_v = 2\pi N R B_r$, which is simply the product of the length of wire used in the voice coil and the magnetic field. Through this constant, the mechanical motion of the magnetic detecting mass is transduced to a voltage, which may be measured by coupling the voice-coil configuration to a scheme for electrical readout.

If we want to write the Hamiltonian for such a system described in fig. 6.2, we will have to be careful about the gauge choices which arises from the spanning tree definitions [128]. Incorporating the mechanical degrees of freedom introduces the canonical momentum p into the Hamiltonian. Importantly, in this case p is not necessarily the mechanical momentum $m\dot{x}$; the gauge choice determines this. In particular, in the first gauge, $p = m\dot{x} + C_L T_v(\dot{\Phi} + T_v \dot{x})$. In the second gauge, $p = m\dot{x}$. Upon promoting the degrees of freedom to operators where $[\hat{Q}, \hat{\Phi}] = -i\hbar$ and $[\hat{p}, \hat{x}] = -i\hbar$, we find these two equivalent descriptions are now related via a more general unitary (gauge) transformation

$$\hat{U} = e^{-iT_v \hat{Q}\hat{x}/\hbar} \ . \tag{6.4}$$

Altogether, we find the Hamiltonians

$$\begin{aligned} H_1^{(E,v)} = \frac{p^2}{2m} + \frac{1}{2}kx^2 - \frac{T_v}{m}Qp \\ + \frac{Q^2}{2}\left(\frac{1}{C_L} + \frac{T_v^2}{m}\right) + \frac{\Phi^2}{2L} \end{aligned} \tag{6.5}$$

and

$$H_2^{(E,v)} = \frac{p^2}{2m} + \frac{1}{2}kx^2 + \frac{Q^2}{2C_L} + \frac{(\Phi - T_v x)^2}{2L} \quad , \tag{6.6}$$

where Q and p are the canonical node charge and momentum, conjugate to the node flux Φ and position x, respectively. However, with only capacitance C_L connected to the node, in this case Q corresponds to the charge on this capacitor's plates as depicted in fig 6.2.

Similarly, an electro-mechanical system with a variable capacitance can be proposed where the voltage generated can be shown to be proportional to the position of the mechanical system in the following way. The mechanical detecting element consists of two oppositely charged plates with charge $\pm Q_C^b$ connected by a linearized spring with spring constant k. This forms a capacitor with one fixed plate and one movable plate of mass m whose capacitance is a function of the position of the movable plate, namely,

$$C(x) = \frac{\epsilon_0 A}{d - x}. \tag{6.7}$$

We take the area of the plates A to be much larger than their uncharged equilibrium separation d. As the massive plate moves due to some detection event, the capacitance changes, thereby altering the charge on the plates and the voltage across them. In total, we come to a linearized Hamiltonian of the form

$$\begin{aligned} H^{(E,x)} = \frac{p^2}{2m} + \frac{1}{2}k_{\text{eff}}(x - x_0)^2 - \frac{T_x}{C_P}(Q - Q_0)(x - x_0) \\ + \frac{(Q - Q_0)^2}{C_{\text{eff}}} + \frac{\Phi^2}{2L} + V(Q_0, x_0) \quad , \end{aligned} \tag{6.8}$$

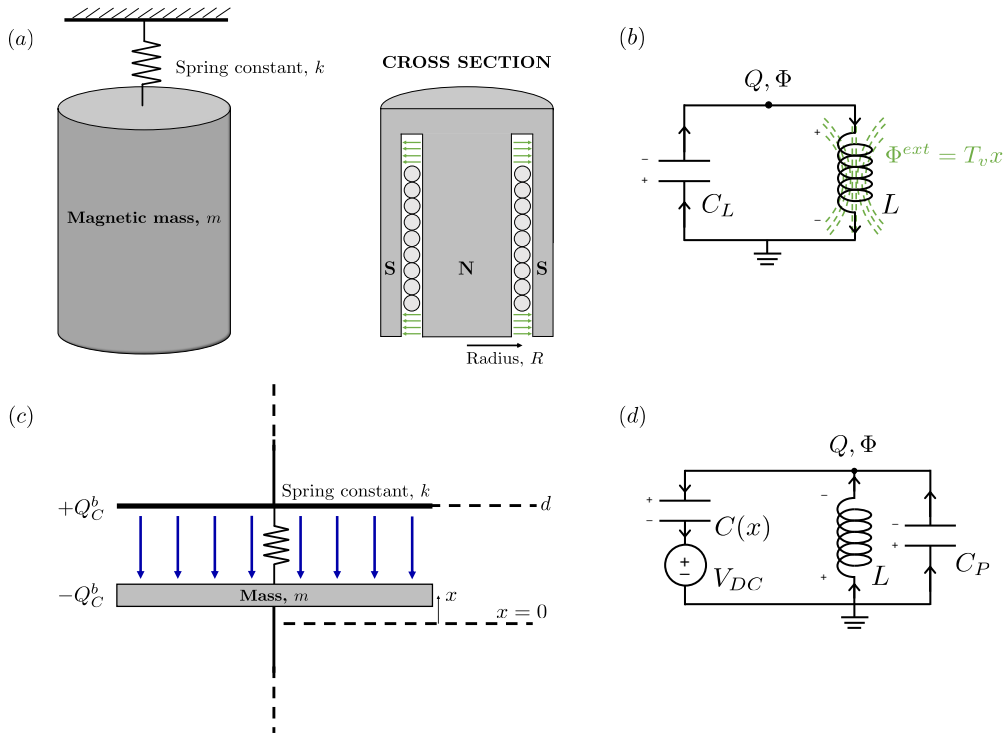

Figure 6.2: (a) Schematic representation of the magnetomechanical transducer, consisting of a structured magnetic mass m suspended via a linearized spring with spring constant k. In the cross section, the radial magnetic field in the air gap experienced by the coil is indicated in green. The lumped-element detector circuit for the magnetomechanical case is shown in (b), where the magnetomechanical element of (a) is modeled as an inductor L threaded by an external flux $\Phi^{ext} = T_v x$ (shown in green) dependent on the position of the magnetic mass. Sign conventions for analysis are indicated as well as the reference ground node and node variables Q, Φ. (c) Schematic representation of the electromechanical transducer, including the electric field (dark blue) between the charged plates of the mechanical capacitor consisting of a movable plate of mass m and charge $-Q_C^b$ connected to a fixed plate of charge $+Q_C^b$ via linearized spring with spring constant k. Equilibrium distances are indicated for reference. In (d), the electromechanical element of (c) is depicted in a lumped-element detector circuit via the capacitance $C(x)$. Sign conventions for analysis are indicated as well as the reference ground node and node variables Q, Φ.

where Q and p are the canonical node charge and momentum, conjugate to the node flux Φ and position x, respectively. In this case, Q corresponds to the sum of the charge on the plates of the two capacitors connected to the node, while p is the mechanical momentum of the movable plate. We define the effective capacitance as $C_{\text{eff}} = C(x_0) + C_P$ and the effective spring constant to be $k_{\text{eff}} = k - \frac{C_{\text{eff}} T_x^2}{C(x_0) C_P}$. The point $\{Q_0, x_0\}$ corresponds to the equilibrium node charge and position

when the plates are charged. While the distance d corresponds to the separation of the plates when uncharged, as the plates charge, the plate separation decreases as electrostatic attraction shifts the position of the movable plate closer to its counterpart. This equilibrium point corresponds to the position where the force of electrostatic attraction and the restorative force of the spring exactly balance. The offset $V(Q_0, x_0)$ corresponds to the energy associated with this equilibrium charge and position configuration. Importantly, this linearization procedure enables us to identify and define the transducer constant T_x in this system:

$$T_x = C_P \frac{(Q_0 - C_P V_{DC})}{\epsilon_0 A} \left(\frac{C(x_0)}{C_{\text{eff}}} \right)^2 \quad , \tag{6.9}$$

which characterizes how changes in the position x of the movable plate result in changes of the charge on the mechanically-varying capacitor's plates $\pm Q_C^b$, with V_{DC} as the source voltage i.e.,

$$Q_C^b \approx \frac{C(x_0)}{C_{\text{eff}}} (Q - C_P V_{DC}) + T_x (x - x_0) \quad . \tag{6.10}$$

We have to keep in mind that in the magneto-mechanical case, the voltage is proportional to the charge Q and thus accessing the charge makes us sensitive to the velocity of the system. On the other hand, the flux through the pick-up coil is proportional to the time integral of the voltage and thus the flux or current is directly proportional to the position of the system.

In the electromechanical system, the voltage is directly proportional to the position of the capacitor and thus it makes the charge variable Q position dependent. The current through the capacitor is thus proportional to the time derivative of the charge which drives a flux through the associated inductor 6.2, making the flux or current proportional to velocity. So, if we access the flux or current of this system, we will be directly sensitive to the velocity of the mechanical

system.

6.4 Idealized Receivers

Our interest lies in the measurement-added noise associated with each detector scheme, whereby a mechanical signal of interest is transduced to an electrical one. As a consequence, the mechanical degrees of freedom are coupled to those of the electrical circuit. This is in contrast to the standard optomechanical position-sensing problem where the mechanical position is directly coupled to a quantity accessible to measurement, namely, a quadrature of the optical cavity, via the cavity's position-dependent resonance.

In an effort to utilize the standard tools and procedures employed in optomechanical analyses of this nature, we construct a system analogous to the optomechanical system described above. We imagine nearby parametric cavities whose resonance frequency is a function of the electric or magnetic fields generated by each electrical circuit, as shown in Fig. 6.3. This amounts to a measurement of the mechanically-generated electrical signal as a voltage via the voltage drop and electric field of a capacitor or a current via the current flow and magnetic field of an inductor. As such, we consider generic voltage and current readout schemes for both the electromechanical and magnetomechanical detection schemes, including the two gauge descriptions.

We note that there are various potential strategies for voltage or current readout in superconducting systems (e.g., a Cooper-pair box or SQUID-based readout for voltage or current measurement, respectively [129, 130]). However, in choosing this general approach of electric or magnetic field sensing via a parametric cavity, existing methods for noise assessment may be

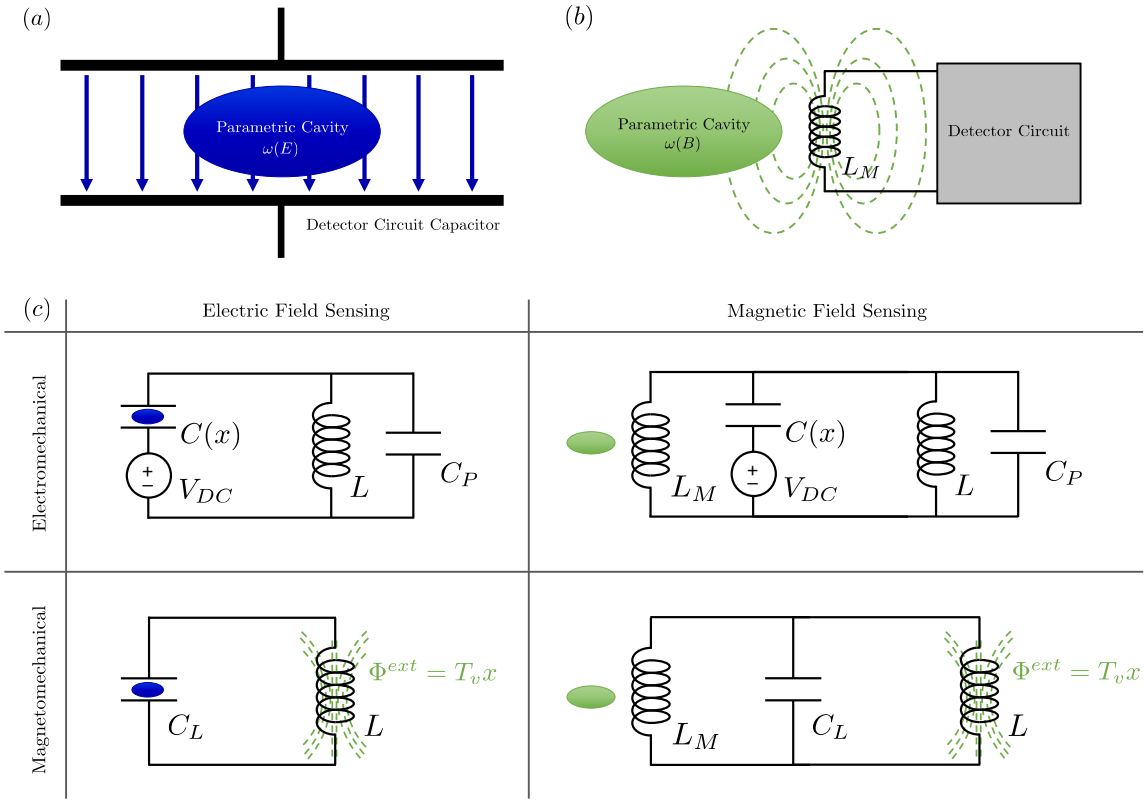

Figure 6.3: (a) Schematic representation of the configuration for voltage measurement via electric field sensing using a parametric cavity with a resonance frequency that depends on the electric field E (indicated in dark blue) inside a capacitor of each detector circuit. (b) Schematic representation of the configuration for current measurement via magnetic field sensing using a parametric cavity with a resonance frequency that depends on the magnetic field B (indicated in green) generated by an inductor L_M connected to each detector circuit. In (c), we provide a visual table showing the different combinations of measurement schemes and detector configurations considered in the main text, including indicators for which circuit elements interact with the parametric cavities in each case.

employed to come to a broader understanding of how different measurement schemes ultimately influence measurement-added noise in electrical systems.

6.4.1 Electric Field Sensing

For a voltage measurement via electric field sensing, we rely on the electric fields generated by the voltage drop across a capacitor for measurement readout by a nearby parametric cavity, as indicated in Fig. 6.3a and the left column of Fig. 6.3c. Therefore, we imagine the parametric cavity to be characterized by a resonance frequency that is a function of the electric field of a coupled capacitor. Generally, we can express the uniform electric field in a parallel plate capacitor in terms of the charge on the plates and their area or the voltage across the plates and their separation: $E = \frac{Q^b}{\epsilon_0 A} = \frac{v^b}{d}$. However, the coupling capacitors and their associated electric fields are unique to each detector configuration.

In the electromechanical case, we take the detecting capacitor $C(x)$ to be the capacitor coupled to the parametric cavity. To express the electric field in this capacitor in terms of the degrees of freedom of the circuit, we use the linearized expression for the charge on the plates of the mechanically-varying capacitor $C(x)$, given by Eq. (6.10). This ensures a linear coupling to the cavity and yields an approximate expression for the electric field of the form

$$E^x \approx \frac{C(x_0)}{C_{\text{eff}}} \frac{(Q - C_P V_{DC})}{\epsilon_0 A} + \frac{T_x}{\epsilon_0 A}(x - x_0) \ . \tag{6.11}$$

Similarly, in the magnetomechanical detector configuration, we take the coupled capacitance to be the parallel capacitance C_L. As the only capacitor connected to the non-reference node in this circuit, the charge on the capacitor's plates corresponds to the node charge Q. This yields the

electric field

$$E^v = -\frac{Q}{\epsilon_0 A} = -\frac{Q}{C_L d_L} \quad , \tag{6.12}$$

where we have taken $C_L = \frac{\epsilon_0 A}{d_L}$ with d_L the separation of the plates. The voltage across the capacitor $v^b_{C_L} = -Q/C_L$ is gauge-independent. As such, Eq. (6.12) relates the degrees of freedom of the circuit to the generated electric field in both gauges.

For each detection scheme, both coupling capacitors are already present in the lumped-element circuits introduced in Fig. 6.2. Therefore, these circuits and their associated Hamiltonians suffice for voltage measurement. We incorporate the parametric cavity into the Hamiltonian description from Section 6.3 by adding a cavity Hamiltonian to the circuit Hamiltonians given in Eqs. (6.8), (6.5) and (6.6). The electric field-dependent resonance may then be used to highlight the coupling between the circuit and the cavity. This cavity Hamiltonian takes the usual form,

$$\hat{H}^E_{cav} = \hbar\omega(E)\hat{a}^\dagger\hat{a} \quad , \tag{6.13}$$

where $\hat{a}^\dagger, \hat{a}$ are the creation and annihilation operators of the cavity mode that satisfy the commutation relation $[\hat{a}, \hat{a}^\dagger] = 1$ and $\omega(E)$ is the resonance frequency of the cavity that depends on the electric field E. To generate the usual optomechanical coupling, we expand $\omega(E)$ with respect to E in a Taylor series about some equilibrium field value E_0:

$$\omega(E) = \omega(E_0) + \left.\frac{d\omega(E)}{dE}\right|_{E=E_0}(E - E_0) + \dots \quad . \tag{6.14}$$

We then make the substitutions for E^x and E^v from Eqs. (6.11) and (6.12) and truncate at linear order to define the frequencies

$$\omega(E^x) = \omega_0^{(E,x)} + g_Q^{(E,x)}\hat{Q} + g_x\hat{x} \tag{6.15}$$

and

$$\omega(E^v) = \omega_0^{(E,v)} - g_Q^{(E,v)}\hat{Q} \ , \tag{6.16}$$

where we have collected relevant constants in each case to define the coupling constants $g_Q^{(E,x)} = \frac{\alpha_E C(x_0)}{C_{\text{eff}}\epsilon_0 A}$, $g_Q^{(E,v)} = \frac{\alpha_E}{C_L d_L}$, and $g_x = \frac{\alpha_E T_x}{\epsilon_0 A}$, including the cavity's sensitivity to electric fields $\alpha_E = \frac{d\omega(E)}{dE}|_{E=E_0}$. We have also defined the rescaled cavity frequencies $\omega_0^{(E,x)} = \omega(E_0^x) - \alpha_E E_0^x - g_Q^{(E,x)} C_P V_{DC} - g_x x_0$ and $\omega_0^{(E,v)} = \omega(E_0^v) - \alpha_E E_0^v$.

Altogether, we write the cavity Hamiltonian in Eq. (6.13) for the electromechanical and magnetomechanical detector configurations as

$$\hat{H}_{cav}^{(E,x)} = \hbar\omega_0^{(E,x)}\hat{a}^\dagger\hat{a} + \hbar\left(g_Q^{(E,x)}\hat{Q} + g_x\hat{x}\right)\hat{a}^\dagger\hat{a} \tag{6.17}$$

and

$$\hat{H}_{cav}^{(E,v)} = \hbar\omega_0^{(E,v)}\hat{a}^\dagger\hat{a} - \hbar g_Q^{(E,v)}\hat{Q}\hat{a}^\dagger\hat{a} \ , \tag{6.18}$$

respectively, where in both cases we have generated the coupling between the cavity and the circuit, akin to the optomechanical treatment.

6.4.2 Magnetic Field Sensing

For current measurement via magnetic field sensing, we exploit the magnetic fields generated by the current flowing through an inductor for measurement readout by a nearby parametric cavity, as shown in Fig. 6.3b. In this case, we take the parametric cavity to be characterized by a resonance frequency dependent on the magnetic field of a coupled inductor, adding a parallel inductance L_M to the circuits considered thus far, as shown in the right column of Fig. 6.3c, such that $L_M < L$. As a consequence, this additional inductor provides a relatively low-impedance element for current to flow through.

Noting that the motion of the detecting masses will alter the current through the inductor L_M, thereby changing the magnetic field it generates, we consider the expression of this magnetic field in terms of circuit quantities. For a long solenoid,

$$B = \mu n i^b_{L_M} = \frac{\mu n \Phi^b_{L_M}}{L_M} \quad , \tag{6.19}$$

where μ is the magnetic permeability of the material making up the core of L_M and n its turn density. The current flowing through the inductor $i^b_{L_M}$ is expressed in terms of its branch flux $\Phi^b_{L_M}$ in the usual way. We note that expressing the branch flux in terms of circuit degrees of freedom is dependent on the detector configuration, and in the magnetomechanical case, also dependent on the gauge choice. This necessitates some care in expressing $\Phi^b_{L_M}$ in terms of relevant circuit degrees of freedom.

One can perform an analogous treatment of the current measurement circuits in Fig. 6.3c and confirm that in the electromechanical case $\Phi^b_{L_M} = \Phi$, while in the magnetomechanical case,

the first gauge yields $\Phi^b_{L_M} = -(\Phi + T_v x)$ and the second gauge yields $\Phi^b_{L_M} = -\Phi$. The associated Hamiltonians are equivalent to their voltage counterparts except for the addition of an inductive term, $(\Phi^b_{L_M})^2/2L_M$. For the electromechanical detector scheme, we find the Hamiltonian

$$H^{(B,x)} = H^{(E,x)} + \frac{\Phi^2}{2L_M} \ , \tag{6.20}$$

while in the magnetomechanical case, we find

$$H_1^{(B,v)} = H_1^{(E,v)} + \frac{(\Phi + T_v x)^2}{2L_M} \tag{6.21}$$

and

$$H_2^{(B,v)} = H_2^{(E,v)} + \frac{\Phi^2}{2L_M} \tag{6.22}$$

for each gauge.

To include the parametric cavity in the description above, we proceed just as in the voltage measurement case, exchanging $\omega(E)$ for $\omega(B)$ and remaining mindful of the various expressions of the magnetic field appropriate for different detector configurations and gauges. We then find the cavity Hamiltonian appropriate for the electromechanical detection scheme to be

$$\hat{H}^{(B,x)}_{cav} = \hbar\omega_0^B \hat{a}^\dagger \hat{a} + \hbar g^B \hat{\Phi} \hat{a}^\dagger \hat{a} \ , \tag{6.23}$$

where we have defined the coupling constant $g^B = \frac{\alpha_B \mu n}{L_M}$, the rescaled resonance frequency $\omega_0^B = \omega(B_0) - \alpha_B B_0$, and the cavity's sensitivity to magnetic fields $\alpha_B = \frac{d\omega(B)}{dB}|_{B=B_0}$. Similarly, we find the Hamiltonians

$$\hat{H}_{cav,1}^{(B,v)} = \hbar\omega_0^B \hat{a}^\dagger \hat{a} - \hbar g^B (\hat{\Phi} + T_v \hat{x}) \hat{a}^\dagger \hat{a} \tag{6.24}$$

and

$$\hat{H}_{cav,2}^{(B,v)} = \hbar\omega_0^B \hat{a}^\dagger \hat{a} - \hbar g^B \hat{\Phi} \hat{a}^\dagger \hat{a} \tag{6.25}$$

for each gauge in the magnetomechanical case.

6.4.3 Exploiting the Optomechanics Analogy

To consider the measurement-added noise in these proposed toy models, we now consider and incorporate a drive to probe the system. To do so, we exploit the optomechanical analogy we have constructed by following the usual formulation for optomechanical systems [131–133] to include the drive and model the associated bath. Altogether, we arrive at the Hamiltonians for voltage and current measurement in both the electromechanical and magnetomechanical detection schemes, accounting for the two gauges in the magnetomechanical case.

For voltage measurement in the electromechanical case, we come to the Hamiltonian

$$\begin{aligned} \hat{H}'^{(E,x)} = -\hbar\Delta \hat{a}^\dagger \hat{a} + \hbar \left(G_Q^{(E,x)} \hat{Q} + G_x \hat{x} \right) \hat{X} \\ + \hat{H}^{(E,x)} + \hat{H}_B + \hat{H}_{int} \ , \end{aligned} \tag{6.26}$$

where we have defined the detuning $\Delta = \omega_L - \omega_0^{(E,x)}$ and the Hamiltonians $\hat{H}_B$ and $\hat{H}_{int}$ describe those of the bath and the bath-cavity coupling, respectively, as defined in section 2.2. Relevant constants have been collected to define $G_Q^{(E,x)} = \sqrt{2}\alpha g_Q^{(E,x)}$ and $G_x = \sqrt{2}\alpha g_x$. Similarly, the

magnetomechanical case is described by the Hamiltonian

$$\hat{H}'^{(E,v)}_i = -\hbar\Delta\hat{a}^\dagger\hat{a} - \hbar G^{(E,v)}_Q \hat{Q}\hat{X} + \hat{H}^{(E,v)}_i + \hat{H}_B + \hat{H}_{int} \ , \tag{6.27}$$

where $i = 1, 2$ for the two gauge choices and we have defined $G^{(E,v)}_Q = \sqrt{2}\alpha g^{(E,v)}_Q$. In both detector schemes, we take the drive strength α to be real, enabling the cavity-circuit coupling to be written in terms of the amplitude quadrature of the cavity, $\hat{X} = (\hat{a} + \hat{a}^\dagger)/\sqrt{2}$.

Alternatively, for current measurement in the each of the detector configurations and gauges, we find the Hamiltonians

$$\hat{H}'^{(B,x)} = -\hbar\Delta\hat{a}^\dagger\hat{a} + \hbar G^B \hat{\Phi}\hat{X} + \hat{H}^{(B,x)} + \hat{H}_B + \hat{H}_{int} \ , \tag{6.28}$$

$$\hat{H}'^{(B,v)}_1 = -\hbar\Delta\hat{a}^\dagger\hat{a} - \hbar G^B(\hat{\Phi} + T_v\hat{x})\hat{X} + \hat{H}^{(B,v)}_1 + \hat{H}_B + \hat{H}_{int} \ , \tag{6.29}$$

and

$$\hat{H}'^{(B,v)}_2 = -\hbar\Delta\hat{a}^\dagger\hat{a} - \hbar G^B \hat{\Phi}\hat{X} + \hat{H}^{(B,v)}_2 + \hat{H}_B + \hat{H}_{int} \ , \tag{6.30}$$

where instead we have defined the coupling constant $G^B = \sqrt{2}\alpha g^B$. In what follows, we use the Hamiltonians in Eqs. (6.26)-(6.30) to find and solve the Heisenberg-Langevin equations, allowing for the assessment of noise sensitivities.

6.5 Matching Transducers to Receivers

With the generic readout and detector schemes considered, we now turn our attention to measurement and the consequences of different transducer and receiver combinations, given by the Hamiltonians in Eqs. (6.26)-(6.30). For each of these combinations, we write down and solve the Heisenberg equations of motion, coming to a force noise power spectral density (PSD). This force noise PSD is the metric we use to assess noise performance at various frequencies.

6.5.1 Finding Equations of Motion

We begin with the usual methods from input-output theory [134], writing down and solving the Heisenberg equation of motion for the bath modes $\hat{b}(\omega)$. This enables the equations of motion for the cavity operators $\hat{a}, \hat{a}^\dagger$ to be expressed in terms of the input modes $\hat{b}_{\text{in}}$ and output modes $\hat{b}_{\text{out}}$. The details of this procedure can be found in section 2.2.

At this stage, it is preferable to recast the equations of motion for the cavity operators in terms of quantities accessible to measurement, namely, the amplitude and phase quadratures of the cavity, $\hat{X}$ and $\hat{Y}$, respectively. They are defined as $\hat{X} = \frac{1}{\sqrt{2}}(\hat{a} + \hat{a}^\dagger)$ and $\hat{Y} = \frac{-i}{\sqrt{2}}(\hat{a} - \hat{a}^\dagger)$, where $[\hat{X}, \hat{Y}] = i$. The input and output quadratures are analogously defined in terms of the input and output bath modes as $\hat{X}_{\text{in}} = (\hat{b}_{\text{in}} + \hat{b}^\dagger_{\text{in}})/\sqrt{2}$, $\hat{Y}_{\text{in}} = -i(\hat{b}_{\text{in}} - \hat{b}^\dagger_{\text{in}})/\sqrt{2}$, $\hat{X}_{\text{out}} = (\hat{b}_{\text{out}} + \hat{b}^\dagger_{\text{out}})/\sqrt{2}$, and $\hat{Y}_{\text{out}} = -i(\hat{b}_{\text{out}} - \hat{b}^\dagger_{\text{out}})/\sqrt{2}$. It can be verified that these each satisfy their own input-output

relations of the form

$$\hat{X}_{\text{out}} = \hat{X}_{\text{in}} + \sqrt{\kappa}\hat{X} \tag{6.31}$$

and

$$\hat{Y}_{\text{out}} = \hat{Y}_{\text{in}} + \sqrt{\kappa}\hat{Y} \quad , \tag{6.32}$$

using their definitions and the input-output relation given section 2.2.

By combining the equations of motion for $\hat{a}$ and $\hat{a}^\dagger$ we find the equations of motion for each cavity quadrature. These equations, in combination with the Heisenberg equations of motion for the remaining system operators ($\hat{x}$, $\hat{p}$, $\hat{\Phi}$, and $\hat{Q}$), specify the complete system of equations describing each case. Below, we explicitly show the equations of motion for each detector configuration, measurement scheme, and gauge, where we have included an input force $\hat{F}_{\text{in}}$ in the equation for the canonical momentum to account for the initial impulse we wish to detect.

We first consider the equations of motion for voltage measurement via electric field sensing. In the magnetomechanical case, the first gauge yields the equations of motion

$$
\begin{aligned}
\frac{d\hat{x}}{dt} &= \frac{\hat{p}}{m} - \frac{T_v}{m}\hat{Q} \ , \\
\frac{d\hat{p}}{dt} &= -k\hat{x} + \hat{F}_{\text{in}} \ , \\
\frac{d\hat{\Phi}}{dt} &= -\hbar G_Q^{(E,v)}\hat{X} - \frac{T_v}{m}\hat{p} + \left(\frac{1}{C_L} + \frac{T_v^2}{m}\right)\hat{Q} \ , \\
\frac{d\hat{Q}}{dt} &= -\frac{\hat{\Phi}}{L} \ , \\
\frac{d\hat{X}}{dt} &= -\Delta\hat{Y} - \frac{\kappa}{2}\hat{X} - \sqrt{\kappa}\hat{X}_{\text{in}} \ , \\
\frac{d\hat{Y}}{dt} &= \Delta\hat{X} + G_Q^{(E,v)}\hat{Q} - \frac{\kappa}{2}\hat{Y} - \sqrt{\kappa}\hat{Y}_{\text{in}} \ .
\end{aligned}
\tag{6.33}
$$

It is convenient to rewrite these equations in a more compact form. Defining the matrix

$$
\underline{\underline{M_1}}^{(E,v)} = \begin{bmatrix}
0 & \frac{1}{m} & 0 & -\frac{T_v}{m} & 0 & 0 \\
-k & 0 & 0 & 0 & 0 & 0 \\
0 & -\frac{T_v}{m} & 0 & \frac{1}{C_L'} & -\hbar G_Q^{(E,v)} & 0 \\
0 & 0 & -\frac{1}{L} & 0 & 0 & 0 \\
0 & 0 & 0 & 0 & -\frac{\kappa}{2} & -\Delta \\
0 & 0 & 0 & G_Q^{(E,v)} & \Delta & -\frac{\kappa}{2}
\end{bmatrix} \ ,
\tag{6.34}
$$

we can rewrite Eq. (6.33) as

$$
\frac{d}{dt}\underline{\hat{Z}} = \underline{\underline{M_1}}^{(E,v)}\underline{\hat{Z}} + \underline{\hat{Z}_{\text{in}}} \ ,
\tag{6.35}
$$

where we have defined the vector of operators $\underline{\hat{Z}} = \{\hat{x}, \hat{p}, \hat{\Phi}, \hat{Q}, \hat{X}, \hat{Y}\}$ and the vector of inputs

$\underline{\hat{Z}_{\text{in}}} = \{0, \hat{F}_{\text{in}}, 0, 0, \text{-}\sqrt{\kappa}\hat{X}_{\text{in}}, \text{-}\sqrt{\kappa}\hat{Y}_{\text{in}}\}$. We also define the capacitance C'_L for convenience to be $\frac{1}{C'_L} = \frac{1}{C_L} + \frac{T_v^2}{m}$. The equations of motion for the second gauge can be similarly represented via Eq. (6.35) with the unique matrix $\underline{\underline{M_2}}^{(E,v)}$ defined as

$$\underline{\underline{M_2}}^{(E,v)} = \begin{bmatrix} 0 & \frac{1}{m} & 0 & 0 & 0 & 0 \\ \text{-}k' & 0 & \frac{T_v}{L} & 0 & 0 & 0 \\ 0 & 0 & 0 & \frac{1}{C_L} & \text{-}\hbar G_Q^{(E,v)} & 0 \\ \frac{T_v}{L} & 0 & \text{-}\frac{1}{L} & 0 & 0 & 0 \\ 0 & 0 & 0 & 0 & \text{-}\frac{\kappa}{2} & \text{-}\Delta \\ 0 & 0 & 0 & G_Q^{(E,v)} & \Delta & \text{-}\frac{\kappa}{2} \end{bmatrix}, \tag{6.36}$$

where we have defined for convenience $k' = k + \frac{T_v^2}{L}$. Likewise, the electromechanical case is described by the matrix

$$\underline{\underline{M}}^{(E,x)} = \begin{bmatrix} 0 & \frac{1}{m} & 0 & 0 & 0 & 0 \\ \text{-}k_{\text{eff}} & 0 & 0 & \frac{T_x}{C_P} & \text{-}\hbar G_x & 0 \\ \text{-}\frac{T_x}{C_P} & 0 & 0 & \frac{1}{C_{\text{eff}}} & \hbar G_Q^{(E,x)} & 0 \\ 0 & 0 & \text{-}\frac{1}{L} & 0 & 0 & 0 \\ 0 & 0 & 0 & 0 & \text{-}\frac{\kappa}{2} & \text{-}\Delta \\ \text{-}G_x & 0 & 0 & \text{-}G_Q^{(E,x)} & \Delta & \text{-}\frac{\kappa}{2} \end{bmatrix}. \tag{6.37}$$

We can analogously describe the equations of motion for the current measurement scheme.

In the magnetomechanical case, we find for the two gauges

$$\underline{\underline{M_1}}^{(B,v)} = \begin{bmatrix} 0 & \frac{1}{m} & 0 & -\frac{T_v}{m} & 0 & 0 \\ -k'_M & 0 & -\frac{T_v}{L_M} & 0 & \hbar G^B T_v & 0 \\ 0 & -\frac{T_v}{m} & 0 & \frac{1}{C'_L} & 0 & 0 \\ -\frac{T_v}{L_M} & 0 & -\frac{1}{L'} & 0 & \hbar G^B & 0 \\ 0 & 0 & 0 & 0 & -\frac{\kappa}{2} & -\Delta \\ G^B T_v & 0 & G^B & 0 & \Delta & -\frac{\kappa}{2} \end{bmatrix}, \tag{6.38}$$

and

$$\underline{\underline{M_2}}^{(B,v)} = \begin{bmatrix} 0 & \frac{1}{m} & 0 & 0 & 0 & 0 \\ -k' & 0 & \frac{T_v}{L} & 0 & 0 & 0 \\ 0 & 0 & 0 & \frac{1}{C_L} & 0 & 0 \\ \frac{T_v}{L} & 0 & -\frac{1}{L'} & 0 & \hbar G^B & 0 \\ 0 & 0 & 0 & 0 & -\frac{\kappa}{2} & -\Delta \\ 0 & 0 & G^B & 0 & \Delta & -\frac{\kappa}{2} \end{bmatrix}, \tag{6.39}$$

where we have defined for convenience the quantities $k'_M = k + \frac{T_v^2}{L_M}$ and $\frac{1}{L'} = \frac{1}{L} + \frac{1}{L_M}$. For the electromechanical detector configuration, we have

$$\underline{\underline{M}}^{(B,x)} = \begin{bmatrix} 0 & \frac{1}{m} & 0 & 0 & 0 & 0 \\ -k_{\text{eff}} & 0 & 0 & \frac{T_x}{C_P} & 0 & 0 \\ -\frac{T_x}{C_P} & 0 & 0 & \frac{1}{C_{\text{eff}}} & 0 & 0 \\ 0 & 0 & -\frac{1}{L'} & 0 & -\hbar G^B & 0 \\ 0 & 0 & 0 & 0 & -\frac{\kappa}{2} & -\Delta \\ 0 & 0 & -G^B & 0 & \Delta & -\frac{\kappa}{2} \end{bmatrix} . \tag{6.40}$$

6.5.2 Assembling the Noise PSD

These are all linear equations and hence straightforward to solve in the frequency domain. Defining the Fourier transform of our relevant operators as follows

$$\begin{aligned} \hat{\mathcal{O}}(\nu) &= \frac{1}{\sqrt{2\pi}} \int_{-\infty}^{\infty} \hat{\mathcal{O}}(t) e^{-i\nu t} dt \\ \hat{\mathcal{O}}(t) &= \frac{1}{\sqrt{2\pi}} \int_{-\infty}^{\infty} \hat{\mathcal{O}}(\nu) e^{i\nu t} d\nu \end{aligned} , \tag{6.41}$$

the time derivatives in the equation of motion given by Eq. (6.35) for each matrix $\underline{\underline{M}}$ simply transform as $\frac{d\hat{\mathcal{O}}(t)}{dt} \rightarrow i\nu\hat{\mathcal{O}}(\nu)$.

Solving the systems of equations given by Eq. (6.35) in the frequency domain, for zero detuning ($\Delta = 0$), yields the general solution form

$$\underline{\hat{Z}}(\nu) = \left(i\nu\underline{\underline{\mathbb{1}}} - \underline{\underline{M}}\right)^{-1} \underline{\hat{Z}_{\text{in}}}(\nu) \ , \tag{6.42}$$

where we focus on the solutions for $\hat{Y}(\nu)$, given by the final row of Eq. (6.42). The circuit degrees of freedom are coupled to $\hat{X}$, hence, the information about the circuit, the mechanics, and ultimately $\hat{F}_{\text{in}}$ will live in the equation of motion of its conjugate $\hat{Y}$ (as opposed to $\hat{X}$, the other quantity accessible to measurement).

In the magnetomechanical system, the solutions found in each gauge are identical for the voltage and current measurement cases, sans the solutions for $\hat{p}$ and $\hat{\Phi}$, as expected due to these quantities being those affected by the unitary that connects the gauges. One can confirm that the unitary in Eq. (6.4) transforms the equations of motion appropriately. For both the electromechanical and magnetomechanical detector schemes, the solutions for $\hat{Y}(\nu)$ may then be used in the input-output relation, Eq.(6.32), to find the output quadrature $\hat{Y}_{\text{out}}(\nu)$.

We then use the solution for the output quadrature $\hat{Y}_{\text{out}}(\nu)$ to assess noise sensitivity. Normalizing with respect to the input force, we define the force estimator as the normalized output quadrature in force units (i.e., we divide $\hat{Y}_{\text{out}}$ by the coefficient of $\hat{F}_{\text{in}}$):

$$\hat{F}_E(\nu) = \hat{F}_{\text{in}} + a\hat{X}_{\text{in}} + b\hat{Y}_{\text{in}} \ , \tag{6.43}$$

where a and b are coefficients specific to each measurement scheme, with a representing the coefficient for the backaction noise term and b corresponding to the shot noise term in this measurement, as we are measuring the $\hat{Y}$ quadrature.

We then determine noise sensitivities via a power spectral density (PSD). We define the force noise PSD as

$$S_{FF}(\nu) = \int_{-\infty}^{\infty} \langle \hat{F}_E^\dagger(\nu)\hat{F}_E(\nu')\rangle \, d\nu' \ . \tag{6.44}$$

The noise PSD specifies how the signal (and its noise) is distributed over frequency, thereby providing an indication of noise performance. It has other uses; for example, it could also be used to determine the net impulse delivered to the detector [135]. To evaluate the noise PSD in Eq. (6.44), we note the following regarding the resulting noise correlation functions:

$$\begin{aligned} \langle \hat{X}_{\text{in}}^{\dagger}(t)\hat{X}_{\text{in}}(t')\rangle &= \langle \hat{Y}_{\text{in}}^{\dagger}(t)\hat{Y}_{\text{in}}(t')\rangle = \frac{1}{2}\delta(t-t') \\ \langle \hat{F}_{\text{in}}^{\dagger}(t)\hat{F}_{\text{in}}(t')\rangle &= N_{\text{BM}}\delta(t-t') \end{aligned} , \tag{6.45}$$

where we have taken the vacuum fluctuations of the cavity to be white noise and the input signal noise from the mechanics to be Brownian noise N_{BM}. The signal noise and vacuum fluctuations are uncorrelated. We also assume that there is no correlation among the input noise quadratures as well.

Taking all of the above into consideration, the general force noise PSD for all considered cases can be written succinctly as:

$$S_{FF}(\nu) = \frac{|a|^2}{2} + \frac{|b|^2}{2} + N_{BM} \ . \tag{6.46}$$

In what follows, we list the noise PSD expressions for each detector configuration and measurement scheme (recalling that the solutions across gauges are identical). Then, we discuss the features of these noise PSD expressions and compare their performances. In the magnetomechanical case, voltage measurement via electric field sensing yields the noise PSD

$$S_{FF}^{(E,v)} = \frac{{G_Q^{(E,v)}}^2 \hbar^2 \kappa m^2 (\omega_m^2 - \nu^2)^2}{2T_v^2 \nu^2 (\frac{\kappa^2}{4} + \nu^2)} + \frac{m^2(\frac{\kappa^2}{4} + \nu^2)\left[\omega_m^2(\frac{\nu^2}{\omega_c^2} - 1) + \nu^2(1 + \frac{C_L T_v^2}{m} - \frac{\nu^2}{\omega_c^2})\right]^2}{2C_L^2 {G_Q^{(E,v)}}^2 T_v^2 \kappa \nu^2} + N_{\mathrm{BM}} \ , \tag{6.47}$$

while for current measurement via magnetic field sensing we find the expression

$$\begin{aligned} S_{FF}^{(B,v)} =& \frac{m^2(\frac{\kappa^2}{4} + \nu^2)}{2{G^B}^2 T_v^2 \kappa}\left[\frac{T_v^2}{mL_M}(1 - \frac{\nu^2}{\omega_l^2}) + \omega_m^2(\frac{L}{L_M} + 1 - \frac{\nu^2}{\omega_c^2}) + \nu^2(\frac{\nu^2}{\omega_c^2} - \frac{L}{L_M} - 1)\right]^2 \\ &+ \frac{{G^B}^2 \hbar^2 \kappa m^2 L^2 (\omega_m^2 + \frac{T_v^2}{mL} - \nu^2)^2}{2T_v^2(\frac{\kappa^2}{4} + \nu^2)} + N_{\mathrm{BM}} \ . \end{aligned} \tag{6.48}$$

For the electromechanical detector configuration, voltage measurement via electric field sensing yields the noise PSD

$$\begin{aligned} S_{FF}^{(E,x)} =& \frac{{G_Q^{(E,x)}}^2 \hbar^2 \kappa}{2(\frac{\kappa^2}{4} + \nu^2)(C_{\mathrm{eff}} T_x + C_P \frac{G_x}{G_Q^{(E,x)}}(-\frac{\nu^2}{\omega_{ce}^2} + 1))^2}\Bigg[- 2C_{\mathrm{eff}} \frac{G_x^2}{{G_Q^{(E,x)}}^2} T_x + C_P \frac{G_x^2}{{G_Q^{(E,x)}}^2}(\frac{\nu^2}{\omega_{ce}^2} - 1) \\ &+ C_{\mathrm{eff}} C_P m(-\omega_m^2 + \nu^2)\Bigg]^2 + \frac{(\frac{\kappa^2}{4} + \nu^2)\left[C_{\mathrm{eff}} T_x^2 + C_P^2 m(\frac{\nu^2}{\omega_{ce}^2} - 1)(\omega_m^2 - \nu^2)\right]^2}{2C_P^2 {G_Q^{(E,x)}}^2 \kappa (C_{\mathrm{eff}} T_x + C_P \frac{G_x}{G_Q^{(E,x)}}(-\frac{\nu^2}{\omega_{ce}^2} + 1))^2} + N_{\mathrm{BM}} \ , \end{aligned} \tag{6.49}$$

while for current measurement via magnetic field sensing we find the expression

$$
\begin{aligned}
S_{FF}^{(B,x)} =& \frac{(\frac{\kappa^2}{4}+\nu^2)}{2C_{\text{eff}}^2 C_P^2 {G^B}^2 \kappa L^2 L_M^2 T_x^2 \nu^2}\left[C_{\text{eff}}(L+L_M)T_x^2 + C_P^2 m L_M(\frac{L}{L_M}(\frac{\nu^2}{\omega_{le}^2}-1)-1)(\omega_m^2-\nu^2)\right]^2 \\
&+ \frac{{G^B}^2 \hbar^2 \kappa (C_{\text{eff}} T_x^2 + C_P^2 m(-\omega_m^2+\nu^2))^2}{2(\frac{\kappa^2}{4}+\nu^2)C_{\text{eff}}^2 C_P^2 T_x^2 \nu^2} + N_{\text{BM}} \ ,
\end{aligned}
\tag{6.50}
$$

where in all instances we have defined the following frequency scales:

$$
\omega_m^2 = \frac{k}{m},\ \omega_{c(\text{ce})}^2 = \frac{1}{LC_{L(\text{eff})}},\ \omega_{l(\text{le})}^2 = \frac{1}{L_M C_{L(\text{eff})}} \ . \tag{6.51}
$$

If we inspect each of the noise PSD expressions, we find that they all have a term inversely proportional to the coupling coefficient squared, i.e., ${G_Q^{(E,x)}}^2$ and ${G_Q^{(E,v)}}^2$ for the voltage measurement scenarios or ${G^B}^2$ for the current measurement scenario. These terms originate from the $\langle \hat{Y}_{\text{in}}^2 \rangle$ contribution to the noise PSD, corresponding to the factor $\frac{|b|^2}{2}$ in Eq. (6.46). As we are interested in monitoring the $\hat{Y}_{\text{out}}$ quadrature, we understand this contribution as shot noise — it constitutes the statistical counting error at the output port. In addition, each noise PSD has another term which is directly proportional to the coupling coefficient squared. These terms arise from the $\langle \hat{X}_{\text{in}}^2 \rangle$ contribution to the noise PSD, corresponding to the factor $\frac{|a|^2}{2}$ in Eq. (6.46). These terms form the basis of backaction noise on the measurement of the output phase quadrature. Fig. 6.4 shows the individual curves representing these shot noise and backaction noise contributions to the total noise PSD for each of the different transducer and readout combinations as well as for varied coupling strengths. Therefore, from Fig. 6.4 we can understand the overall frequency response of each of these terms. As expected, the shot noise

decreases with an increase in coupling strength (i.e., a stronger drive) whereas the backaction noise increases.

We also note the presence of various resonance features, which we can understand in terms of relevant frequencies in each system. For voltage readout of the magnetomechanical system, shown in Fig. 6.4c and described by Eq. (6.47), the backaction noise term exhibits a resonance at the mechanical frequency ω_m while the shot noise term has two resonances: one near ω_m and the other near the self-resonance of the detector circuit ω_c. This is a consequence of our chosen parameters which result in $\omega_l^2 \gg \omega_c^2 \gg \frac{T_v^2}{mL} \gg \omega_m^2$, where the quantity $\frac{T_v^2}{mL}$ represents the shift in the mechanical resonance due to the circuit coupling. Similarly, for current readout in the magnetomechanical system, shown in Fig. 6.4d and described by Eq. (6.48), resonances occur near $\sqrt{\frac{T_v^2}{mL}}$ in both the backaction and shot noise terms. For the electromechanical system, described by Eqs. (6.49) and (6.50) and shown in Figs. 6.4a and 6.4b, both voltage and current readout demonstrate resonances near ω_m. In addition, a resonance near the circuit's self-resonance ω_{ce} is just visible in the voltage measurement case in Fig. 6.4a. As before, the location of these resonances are a consequence of our chosen parameters, where we note $G_Q^{(E,x)} \gg G_x$ and $\omega_{le}^2 \gg \omega_{ce}^2 \gg \omega_m^2$.

While these resonance features might be useful for some applications, our interest is in the broadband frequency response of the noise PSD rather than monochromatic signals, where noise optimization at a specific frequency, especially efforts to tune a set-up around the resonance frequencies, would be important. In contrast, our goal is to look for signals which have broad characteristics in frequency space (i.e., an impulse in the time domain), requiring an integration of the noise over a bandwidth of frequency in order to analyze a signal to noise ratio (SNR). Additionally, if we can directly access a QND-like variable, such as the velocity of the mechanical

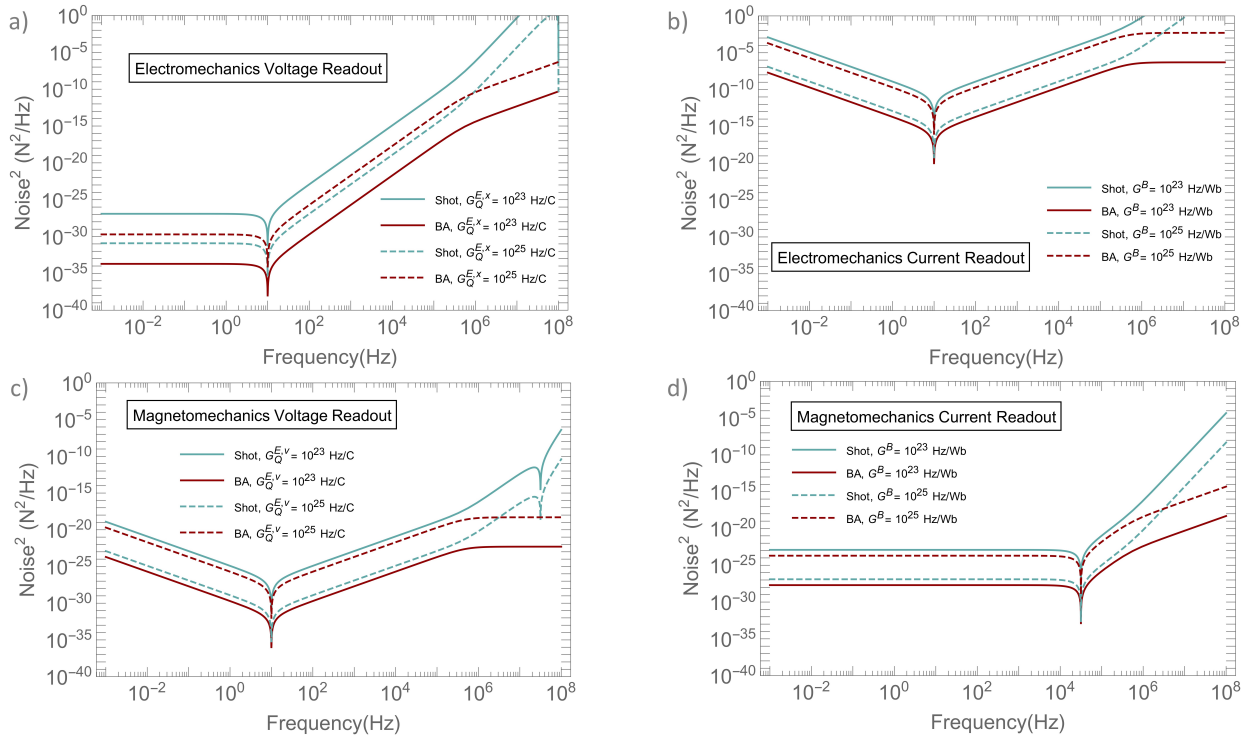

Figure 6.4: Shot noise (light blue) and backaction noise (dark red) curves at different coupling strengths for the electromechanical and magnetomechanical set-ups. In all instances solid curves correspond to smaller coupling strengths relative to the dashed curves, indicated in the legends of each plot. Plots in (a) and (b) show the curves for the electromechanical detector configuration, where (a) represents the electric-field dependent parametric cavity or voltage readout and (b) represents the magnetic field dependent parametric cavity or current readout. Plots in (c) and (d) show the curves for the magnetomechanical detector configuration, where (c) represents the electric-field dependent parametric cavity or voltage readout and (d) represents the magnetic field dependent parametric cavity or current readout. The parameters used for generating these plots are as follows: detector mass $m = 1$ g, mechanical resonance frequency $\omega_m = 10$ Hz, cavity decay rate $\kappa = 1$ MHz, inductance $L = 1$ μH, mutual inductance $L_M = 1$ nH, capacitance $C_L = 1$ nF, capacitance $C_{\text{eff}} = 0.1$ nF, capacitance $C_P = 1$ pF, transducer constant $T_v = 1$ T-m, transducer constant $T_x = 10^{-10}$ C/m, coupling coefficient $G_x = 10^{-10} G_Q^{(E,x)}$ Hz/m.

system, we expect the measurement backaction to decrease over a broad frequency spectrum. Therefore, we restrict our discussion to the broadband frequency response of the noise PSD in an effort to understand the best readout strategies for certain kinds of transducers subject to broadband signals.

Focusing on the behavior of these noise PSD expressions over a range of frequencies, we make several observations. At high frequency where $\nu > \kappa$, we see similar behavior in the backaction and shot noise terms across all of the detector and readout combinations. In particular, backaction noise is either constant in this region, as in Figs. 6.4b and 6.4c for electromechanical current readout and magnetomechanical voltage readout, respectively, or diverges as ν^2, as in Figs. 6.4a and 6.4d for electromechanical voltage readout and magnetomechanical current readout, respectively. On the other hand, shot noise diverges as either ν^4 for electromechanical current readout and magnetomechanical voltage readout or ν^6 for electromechanical voltage readout and magnetomechanical current readout.

More important, however, is the behavior observed in the region of frequency above the mechanical resonance but below the cavity decay rate κ. This is a consequence of our signal of interest — as this signal is an impulse delivered over a very short time, we are interested in making measurements on the timescale associated with this frequency range. We note a sharp contrast in the behavior of the electromechanical voltage readout and magnetomechanical current readout cases (Figs. 6.4a and 6.4d) when compared to that of electromechanical current readout and magnetomechanical voltage readout (Figs. 6.4b and 6.4c). In the former, backaction and shot noise are constant in the regions for which $\nu < \omega_m, \sqrt{\frac{T_v^2}{mL}}$, and in the region $\omega_m, \sqrt{\frac{T_v^2}{mL}} < \nu < \kappa$, diverge as ν^4. In the latter, backaction and shot noise go as ν^{-2} for $\nu < \omega_m$ and ν^2 for $\omega_m < \nu < \kappa$. In other words, the electromechanical current and magnetomechanical voltage schemes

exhibit a decrease in backaction noise in the vicinity of the mechanical resonance.

This term-by-term behavior in each frequency regime directly contributes to the resulting overall behavior of the total measurement-added noise in each case, shown in Fig. 6.5. We note that we have taken the thermal noise contribution from the mechanics, given by N_{BM}, to be negligible. In addition, we have chosen the coupling coefficients such that the total noise in Fig. 6.5 is dominated by backaction noise, except in the very high frequency regime, as can be understood from Fig. 6.4. Taken together, the total noise and its associated behavior are particularly relevant in the context of the standard optomechanical position-sensing problem as well as previous work on velocity sensing in optomechanical systems [96, 135]. For convenience of comparison, we have included Fig. A.1, which shows the expected noise PSD for both position and velocity sensing scenarios in an optomechanical analogue, specifically for use with a broadband signal. Details associated with this plot can be found in Appendix A.

Upon comparison, it is immediately clear that voltage readout of the electromechanical detector and current readout of the magnetomechanical detector share similarities with the noise PSD for standard optomechanical position sensing, specifically the 'flat at low frequency' feature. Furthermore, current readout of the electromechanical detector and voltage readout of the magnetomechanical detector bear striking similarity to the noise PSD for velocity sensing. Both show a decrease in total noise near the mechanical resonance, and share the same frequency dependence in this region, namely, going as ν^{-2} below resonance and ν^{2} above resonance.

We understand these similarities by using the fundamental relations describing how the mechanics are transduced to an electrical signal in each detector configuration, outlined in Section 6.3. In the magnetomechanical case, the flux (comparable to current) is proportional to the position x of the mechanical oscillator, while in the electromechanical case, charge

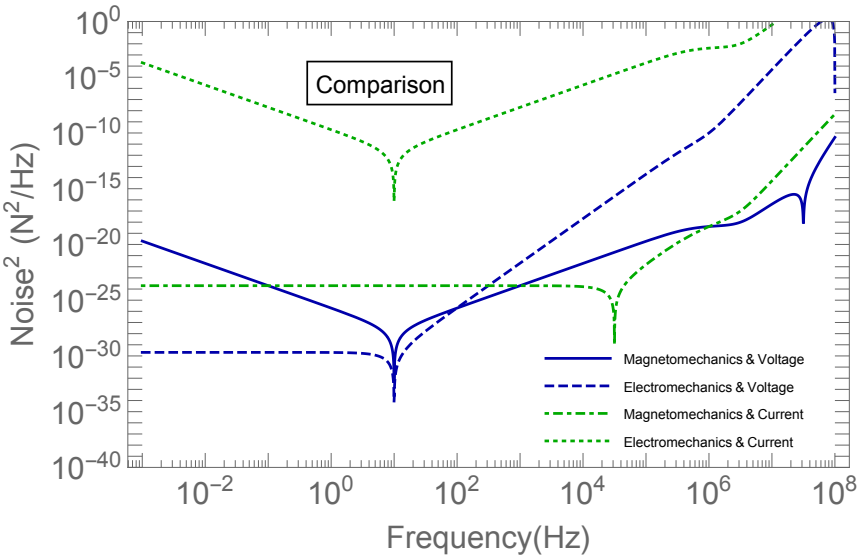

Figure 6.5: Total measurement-added noise for each detector configuration and readout choice. The dark blue curves correspond to voltage readout via electric field sensing for the electromechanical and magnetomechanical configurations. Here, the magnetomechanical system displays a velocity-sensing characteristic absent in the electromechanical case. The green curves correspond to current readout via magnetic field sensing for each detector configuration. However, in this case the electromechanical system displays a velocity-sensing feature rather than the magnetomechanical case. The parameters used for generating these plots are as follows: detector mass $m = 1$ g, mechanical resonance frequency $\omega_m = 10$ Hz, cavity decay rate $\kappa = 1$ MHz, inductance $L = 1$ μH, mutual inductance $L_M = 1$ nH, capacitance $C_L = 1$ nF, capacitance $C_{\text{eff}} = 0.1$ nF, capacitance $C_P = 1$ pF, transducer constant $T_v = 1$ T-m, transducer constant $T_x = 10^{-10}$ C/m, coupling coefficient $G_x = 10^{15}$ Hz/m, coupling coefficients $G_Q^{(E,v)} = G_Q^{(E,x)} = 10^{25}$ Hz/C, coupling coefficient $G^B = 10^{25}$ Hz/Wb.

(comparable to voltage) is proportional to position. Thus, by coupling the parametric cavity to a specific circuit degree of freedom, both of these readout schemes access the position of the mechanical oscillator. Alternatively, it is voltage in the magnetomechanical case and current in the electromechanical case which are directly proportional to velocity. Therefore, electromechanical current readout and magnetomechanical voltage readout directly access the velocity of the oscillator, providing a way to reduce the measurement-added backaction noise over certain bandwidths of frequencies.

These results indicate that if we want to attain a QND-like measurement using an electrical circuit set-up in the microwave domain, we need to match an electromechanical or magnetomechanical transducer with the appropriate readout scheme. Namely, voltage readout for a magnetomechanical transducer and current readout for an electromechanical transducer may yield a QND-like measurement and reduce backaction over a broad range of frequency.

6.6 Conclusions

In this article, we have demonstrated a way to be directly sensitive to the velocity of a mechanical oscillator using an electrical circuit set-up and then probing the circuit quantities with a parametric cavity toy model. We have presented examples of transducers in the microwave domain which would transduce a mechanical signal to an electric or magnetic signal. These include the use of an electromechanical transducer with a varying capacitance or a magnetomechanical transducer with a moving magnetic mass through a pick-up coil. We have explicitly written down the Hamiltonians for these systems and have shown how the mechanics to circuit coupling can be written in different forms for the magnetomechanical case but they are

equivalent.

We have then discussed about the choice of receivers for these transducers. Our result shows that the current measurement for the electromechanical transducer and the voltage measurement for the magnetomechanical transducer will let us directly access the velocity of the mechanical system. The intuition for how to understand the mechanical degree of freedom being accessed in measurement comes down to the relation defining the transducer constant. In the magnetomechanical case, Faraday's law provides the relation $\dot{\Phi}_{ext} = T\dot{x}$. This relates voltage/charge to velocity and current/flux to position. As a result, voltage measurement (which couples charge to the cavity) will access velocity while current measurement (which couples flux to the cavity) will access position. In the electromechanical case, while there isn't a fundamental electromagnetism principle that provides the relation defining the transducer constant, we can derive it to get $Q = Tx$. In contrast to the magnetomechanical case, this relation would connect voltage/charge to position and current/flux to velocity. In this way, a voltage measurement instead accesses position while a current measurement accesses velocity.

This approach to velocity sensing would let us reduce the measurement-added noise while monitoring the mechanical motion in the microwave domain. This is the result of the QND structure of the velocity variable in the context of a mechanical oscillator, well above its resonance frequency, i.e. in the free particle limit. These techniques are particularly useful in dark matter searches.

Chapter 7: Summary and Conclusions

In this thesis, we have attempted to lay out a framework for quantum noise reduction for impulse metrology, especially in the context of searches for dark matter candidates. We have exploited the advances in optomechanical devices and sensing technologies to present the approaches of achieving ultrasensitive force measurements for this purpose.

In the first part of the thesis, we have shown that detecting heavy dark matter candidates through their gravitational interaction alone, even though a very challenging task indeed, is not beyond the reach of rapid improvements in quantum sensing technologies. We are especially interested in the gravitational interaction because that is the guaranteed interaction between dark matter candidates and the visible matter surrounding us. Our proposal includes a detector array concept where about a billion of mg-g scale mechanical sensors would be arranged in a three dimensional array kind of set-up with mm-cm spacings. A Planck-scale dark matter candidate when passing through that array will create a correlated track like signature, while imparting tiny impulses to the sensors due to the gravitational interaction. The effects of these impulses can be read out by monitoring the motion of the sensors. Employing an efficient and effective readout is a key ingredient to the reduction of noise associated with these measurements. Thus we turned our focus onto the impulse metrology task at hand and tried to answer the questions about the fundamental limitation to the sensitivities of these devices.

When we want to measure a specific variable of interest with utmost precision, a fundamental limitation arises from the Heisenberg uncertainty principle, whereby measuring one quadrature precisely, we inadvertently introduce more noise to its conjugate quadrature. If during the system evolution, there is any feedback of noise to the variable of interest from its conjugate quadrature, we would run into the noise limits namely the standard quantum limit. For the large mass, low frequency resonators we consider, this measurement added noise dominates over the thermal noise from other environmental noise sources. In the rest of the thesis, we have discussed our works on different quantum noise reduction techniques which would help us in lowering this measurement-added noise floor.

In chapter 4, we have specifically shown a practical implementation of velocity sensing in the optomechanical domain with double ring cavities connected through a delay line, which would let us achieve backaction evading measurements. Velocity is a quantum non-demolition (QND) variable of the mechanical sub-system, if we are considering measurements well above its resonance frequency. Even-though it is not a QND variable of the combined detector and probe system, directly accessing the velocity lets us achieve substantial reduction of backaction noise. In our double ring cavity set-up, the light interacts wih the mechanical sensor twice from the opposite sides, thus yielding a net reduction in the random momentum kicks which is the source of the backaction noise in this measurement. Consequently, the phase of the outgoing light picks up the information about the differences in the positions at two instances, which essentially makes this system sensitive to the velocity of the mechanical detector. We have presented the noise PSD corresponding to this set-up in comparison to the standard position sensing scenario, along with analyzing the SNR for the dark matter detection purpose.

In chapter 5, we have explored the theoretical limits to further noise reduction by combining

different noise reduction resources like QND measurements and squeezing. Squeezing is the technique to introduce lesser noise to a quadrature of interest at the expense of adding more noise to its conjugate counterpart to preserve the uncertainty relation. We have presented a toy model calculation to understand how single mode and two mode squeezed sources of probing light can aid in the reduction of measurement-added noise for a standard position sensing scenario while also lowering the power requirement. Then we have analyzed a hypothetical model of direct velocity sensing through optical quadratures along with providing some examples of how to achieve that practically. We have considered combining the velocity sensing approach with squeezed probes in order to enhance the sensitivity of our devices to broad-band signals for the purpose of dark matter detection.

In chapter 6, we have discussed the benefits of microwave domain readout and laid out the advantages of the velocity sensing schemes using electromechanical set-up and magnetomechanical set-ups. We have shown that the power requirement in the microwave domain can be substantially less than that of the optical domain while maintaining a similar level of coupling strength per photon. Then we have analyzed the ways to be directly sensitive to the velocity using an electrical readout set-up which converts the mechanical signal to an electric or magnetic one and a parametric cavity as an optomechanical analogue which picks up the information about the desired circuit degree of freedom. We have considered the use of either an electromechanical transducer with varying capacitance or a magnetomechanical transducer with a moving magnetic mass through a pick-up coil. We show how the circuit degrees of freedom in these scenarios couple to either the position or the velocity of the mechanical element we are interested in monitoring. We analyze the measurement-added noise in this scenario, with the help of a parametric cavity set-up which reveals that depending on the circuit quadrature we are

reading out, we can either directly sense the position or the velocity of the mechanical detector. It turns out that reading out the voltage for the magnetomechanical system and reading out the current in the electromechanical system would let us access the velocity of the mechanical system, thus paving a way to take advantages of the QND structure of velocity measurement and leading to backaction noise evasion.

Our proposal on gravitational detection of heavy dark matter candidates had set the stage for the formation of the Windchime collaboration. The researchers involved in the collaboration from many different fields are interested in addressing the key challenges of building such an array like set-up, ultimately leading to the gravitational detection of Planck-mass dark matter candidates. Some of the members are focusing on the sensor developments and scalability for a prototype set-up by building on-chip accelerometers whereas some members are investigating the possibility of using magnetically levitated sensors in the near future to decrease the effect of environmental noise. Some members are actively looking into the experimental implementation of the quantum-enhanced optical readout techniques, some of which we have described above. On the theoretical front, we are exploring the possibility of investigating other non-gravitational signals from dark matter with a smaller size set-up such as the B-L vector boson interaction with ultra-light dark matter [49], along with examining different quantum systems and readout techniques for development of theoretical proposals on quantum-limited impulse sensing. We continue to work on the development of energy-efficient readout techniques including pulsed measurements, use of entanglements etc. to enhance the sensitivity of the Windchime sensors. We are hoping to broaden the scopes of the Windchime sensors to be sensitive to a wide variety of dark matter models and explore various detector set-ups for the highest efficiency and sensitivity achievable in the near-term.

In conclusion this thesis lays out the basic limitations related to noise while doing impulse measurements and demonstrates a few readout techniques to go beyond those noise limits. Though we have discussed most of these techniques in the context of dark matter detection, the scopes of applications for these techniques are much wider than the particle physics targets we discussed. Ultra-sensitive force measurements have been a topic of interest for many decades and in many fields of science and, technology. We hope that the content discussed in this thesis would aid in the advancement of research towards this extensive direction.

Appendix A: Analysis of Optomechanical Systems to Yield Fig. A.1

This is a derivative work based on chapter 5 and [96] in the context of the microwave domain readout. Here we consider the continuous measurement of an optomechanical system subject to either direct position or direct momentum coupling. In the case where the probing optical amplitude quadrature $\hat{X}$ directly interacts with the position $\hat{x}$ of the mechanical system, the interaction Hamiltonian takes the form

$$\hat{H}_{\text{int}} = \hbar G \hat{x} \hat{X} \quad . \tag{A.1}$$

This is the basis of the standard optomechanical position sensing problem. If instead the optical quadrature directly interacts with the velocity, i.e., the mechanical momentum of the system, which can be practically implemented by specific designs of the system as in Refs. [36, 96], the interaction Hamiltonian becomes

$$\hat{H}_{\text{int}} = \hbar G' \hat{p} \hat{X} \quad . \tag{A.2}$$

Following the standard procedures and Section 6.5, we write down the full Hamiltonian and derive the equations of motion for these systems. Here we additionally consider a mechanical damping with damping coefficient μ. Then, we solve for the output phase quadrature of light $\hat{Y}_{\text{out}}$

using the input-output relations. These yield the following estimated force expressions [96]:

$$\hat{F}_{E_x} = -G\hbar\chi_c\hat{X}_{\text{in}} + \frac{e^{i\phi_c}\hat{Y}_{\text{in}}}{G\chi_c\chi_m} + \hat{F}_{\text{in}} \ , \tag{A.3}$$

and

$$\hat{F}_{E_v} = -iG'\hbar\chi_c m\frac{\omega_m^2}{\nu}\hat{X}_{\text{in}} + \frac{ie^{i\phi_c}}{G'm\nu\chi_c\chi_m}\hat{Y}_{\text{in}} + \hat{F}_{\text{in}} \ . \tag{A.4}$$

Here we define the cavity response function χ_c, the mechanical response function χ_m, and the cavity phase shift $e^{i\phi_c}$ as

$$\begin{aligned} \chi_c &= \frac{\sqrt{\gamma}}{-i\nu + \gamma/2} \ , \\ \chi_m &= \frac{-1}{m(\nu^2 - \omega_m^2 + i\mu\nu)} \ , \\ e^{i\phi_c} &= \frac{-i\nu - \gamma/2}{-i\nu + \gamma/2} \ . \end{aligned} \tag{A.5}$$

Using these estimated force expressions we can derive the noise PSD solutions analogously to those derived in the main text and use them to generate the broadband noise PSD plot in Fig. A.1.

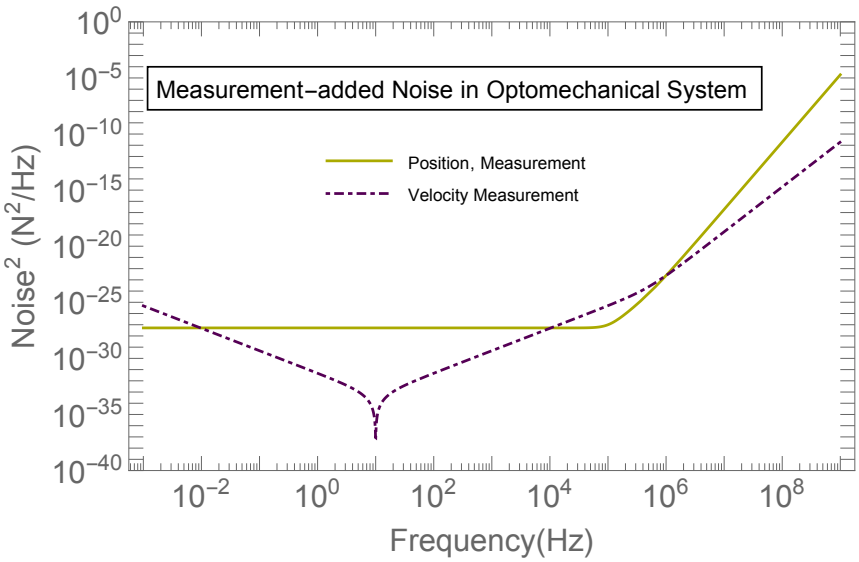

Figure A.1: The noise PSD representing total measurement-added noise in an optomechanical system is plotted for both position and velocity sensing protocols as described in Appendix A. The noise for velocity sensing is lower than position sensing across a broad frequency range, with the functional dependence ν^{-2} below resonance and ν^2 above. The optomechanical coupling strengths in these techniques are related by the velocity coupling coefficient $G' \to G/(m\gamma)$, with position coupling coefficient $G \approx 10^{23}$ Hz/m, mechanical frequency $\omega_m = 10$ Hz, cavity decay rate $\gamma = 1$ MHz, detector mass $m = 1$ g, mechanical damping rate $\mu = 0.1$ mHz.

Bibliography

[1] Edvige Corbelli and Paolo Salucci. The extended rotation curve and the dark matter halo of m33. *Monthly Notices of the Royal Astronomical Society*, 311(2):441–447, 2000.

[2] Douglas Clowe, Maruša Bradač, Anthony H Gonzalez, Maxim Markevitch, Scott W Randall, Christine Jones, and Dennis Zaritsky. A direct empirical proof of the existence of dark matter. *The Astrophysical Journal*, 648(2):L109, 2006.

[3] Matthew D Schwartz. *Quantum field theory and the standard model*. Cambridge university press, 2014.

[4] P James E Peebles and Bharat Ratra. The cosmological constant and dark energy. *Reviews of modern physics*, 75(2):559, 2003.

[5] CL Reichardt, Peter AR Ade, JJ Bock, J Richard Bond, JA Brevik, CR Contaldi, MD Daub, JT Dempsey, JH Goldstein, WL Holzapfel, et al. High-resolution cmb power spectrum from the complete acbar data set. *The Astrophysical Journal*, 694(2):1200, 2009.

[6] Massimo Persic, Paolo Salucci, and Fulvio Stel. The universal rotation curve of spiral galaxies—i. the dark matter connection. *Monthly Notices of the Royal Astronomical Society*, 281(1):27–47, 1996.

[7] KG Begeman, AH Broeils, and RH Sanders. Extended rotation curves of spiral galaxies: Dark haloes and modified dynamics. *Monthly Notices of the Royal Astronomical Society*, 249(3):523–537, 1991.

[8] Stacy S McGaugh. A tale of two paradigms: the mutual incommensurability of λcdm and mond. *Canadian Journal of Physics*, 93(2):250–259, 2015.

[9] Nabila Aghanim, Yashar Akrami, Mark Ashdown, J Aumont, C Baccigalupi, M Ballardini, AJ Banday, RB Barreiro, N Bartolo, S Basak, et al. Planck 2018 results-vi. cosmological parameters. *Astronomy & Astrophysics*, 641:A6, 2020.

[10] Riccardo Catena and Piero Ullio. A novel determination of the local dark matter density. *Journal of Cosmology and Astroparticle Physics*, 2010(08):004, 2010.

[11] Jo Bovy and Scott Tremaine. On the local dark matter density. *The Astrophysical Journal*, 756(1):89, 2012.

[12] Michael Kuhlen, Neal Weiner, Jürg Diemand, Piero Madau, Ben Moore, Doug Potter, Joachim Stadel, and Marcel Zemp. Dark matter direct detection with non-maxwellian velocity structure. *Journal of Cosmology and Astroparticle Physics*, 2010(02):030, 2010.

[13] Vid Iršič, Matteo Viel, Martin G Haehnelt, James S Bolton, and George D Becker. First constraints on fuzzy dark matter from lyman-α forest data and hydrodynamical simulations. *Physical review letters*, 119(3):031302, 2017.

[14] Gordan Krnjaic and Kris Sigurdson. Big bang darkleosynthesis. *Physics Letters B*, 751:464–468, 2015.

[15] Edward Hardy, Robert Lasenby, John March-Russell, and Stephen M West. Signatures of large composite dark matter states. *Journal of High Energy Physics*, 2015(7):1–30, 2015.

[16] Yang Bai and Nicholas Orlofsky. Primordial extremal black holes as dark matter. *Physical Review D*, 101(5):055006, 2020.

[17] Marc Schumann. Direct detection of wimp dark matter: concepts and status. *Journal of Physics G: Nuclear and Particle Physics*, 46(10):103003, 2019.

[18] E Aprile, Jelle Aalbers, F Agostini, M Alfonsi, L Althueser, FD Amaro, Vasile C Antochi, E Angelino, JR Angevaare, F Arneodo, et al. Projected wimp sensitivity of the xenonnt dark matter experiment. *Journal of Cosmology and Astroparticle Physics*, 2020(11):031, 2020.

[19] Nick Du, N Force, R Khatiwada, E Lentz, R Ottens, LJ Rosenberg, Gray Rybka, G Carosi, N Woollett, D Bowring, et al. Search for invisible axion dark matter with the axion dark matter experiment. *Physical review letters*, 120(15):151301, 2018.

[20] L Zhong, S Al Kenany, KM Backes, BM Brubaker, SB Cahn, G Carosi, YV Gurevich, WF Kindel, SK Lamoreaux, KW Lehnert, et al. Results from phase 1 of the haystac microwave cavity axion experiment. *Physical Review D*, 97(9):092001, 2018.

[21] Daniel Carney, Sohitri Ghosh, Gordan Krnjaic, and Jacob M Taylor. Proposal for gravitational direct detection of dark matter. *Physical Review D*, 102(7):072003, 2020.

[22] Alaina Attanasio, Sunil A Bhave, Carlos Blanco, Daniel Carney, Marcel Demarteau, Bahaa Elshimy, Michael Febbraro, Matthew A Feldman, Sohitri Ghosh, Abby Hickin, et al. Snowmass 2021 white paper: The windchime project. *arXiv preprint arXiv:2203.07242*, 2022.

[23] Michael J Biercuk, Hermann Uys, Joe W Britton, Aaron P VanDevender, and John J Bollinger. Ultrasensitive detection of force and displacement using trapped ions. *Nature nanotechnology*, 5(9):646–650, 2010.

[24] David Mason, Junxin Chen, Massimiliano Rossi, Yeghishe Tsaturyan, and Albert Schliesser. Continuous force and displacement measurement below the standard quantum limit. *Nature Physics*, 15(8):745–749, 2019.

[25] HJ Mamin and D Rugar. Sub-attonewton force detection at millikelvin temperatures. *Applied Physics Letters*, 79(20):3358–3360, 2001.

[26] Fernando Monteiro, Wenqiang Li, Gadi Afek, Chang-ling Li, Michael Mossman, and David C Moore. Force and acceleration sensing with optically levitated nanogram masses at microkelvin temperatures. *Physical Review A*, 101(5):053835, 2020.

[27] Chris Timberlake, Giulio Gasbarri, Andrea Vinante, Ashley Setter, and Hendrik Ulbricht. Acceleration sensing with magnetically levitated oscillators above a superconductor. *Applied Physics Letters*, 115(22):224101, 2019.

[28] Carlton M Caves, Kip S Thorne, Ronald WP Drever, Vernon D Sandberg, and Mark Zimmermann. On the measurement of a weak classical force coupled to a quantum-mechanical oscillator. i. issues of principle. *Reviews of Modern Physics*, 52(2):341, 1980.

[29] Markus Aspelmeyer, Tobias J Kippenberg, and Florian Marquardt. Cavity optomechanics. *Reviews of Modern Physics*, 86(4):1391, 2014.

[30] Aashish A Clerk, Michel H Devoret, Steven M Girvin, Florian Marquardt, and Robert J Schoelkopf. Introduction to quantum noise, measurement, and amplification. *Reviews of Modern Physics*, 82(2):1155, 2010.

[31] Carlton M Caves. Quantum-mechanical radiation-pressure fluctuations in an interferometer. *Physical Review Letters*, 45(2):75, 1980.

[32] Carlton M Caves. Quantum-mechanical noise in an interferometer. *Physical Review D*, 23(8):1693, 1981.

[33] Kip S Thorne, Ronald WP Drever, Carlton M Caves, Mark Zimmermann, and Vernon D Sandberg. Quantum nondemolition measurements of harmonic oscillators. *Physical Review Letters*, 40(11):667, 1978.

[34] Henning Vahlbruch, Alexander Khalaidovski, Nico Lastzka, Christian Gräf, Karsten Danzmann, and Roman Schnabel. The geo 600 squeezed light source. *Classical and Quantum Gravity*, 27(8):084027, 2010.

[35] Junaid Aasi, Joan Abadie, BP Abbott, Richard Abbott, TD Abbott, MR Abernathy, Carl Adams, Thomas Adams, Paolo Addesso, RX Adhikari, et al. Enhanced sensitivity of the ligo gravitational wave detector by using squeezed states of light. *Nature Photonics*, 7(8):613–619, 2013.

[36] Sohitri Ghosh, Daniel Carney, Peter Shawhan, and Jacob M Taylor. Backaction-evading impulse measurement with mechanical quantum sensors. *Physical Review A*, 102(2):023525, 2020.

[37] A. A. Clerk, M. H. Devoret, S. M. Girvin, Florian Marquardt, and R. J. Schoelkopf. Introduction to quantum noise, measurement, and amplification. *Rev. Mod. Phys.*, 82:1155–1208, Apr 2010.

[38] CW Gardiner and MJ Collett. Input and output in damped quantum systems: Quantum stochastic differential equations and the master equation. *Physical Review A*, 31(6):3761, 1985.

[39] Vittorio Giovannetti, Seth Lloyd, and Lorenzo Maccone. Quantum-enhanced measurements: beating the standard quantum limit. *Science*, 306(5700):1330–1336, 2004.

[40] Vittorio Giovannetti, Seth Lloyd, and Lorenzo Maccone. Quantum metrology. *Physical review letters*, 96(1):010401, 2006.

[41] Luca Pezzé and Augusto Smerzi. Entanglement, nonlinear dynamics, and the heisenberg limit. *Physical review letters*, 102(10):100401, 2009.

[42] Daniel F Walls. Squeezed states of light. *nature*, 306(5939):141–146, 1983.

[43] J Gea-Banacloche and G Leuchs. Squeezed states for interferometric gravitational-wave detectors. *Journal of Modern Optics*, 34(6-7):793–811, 1987.

[44] VB Braginskii, Yu I Vorontsov, and F Ya Khalili. Optimal quantum measurements in detectors of gravitation radiation. *JETP Lett*, 27(5), 1978.

[45] Vladimir B Braginsky, Yuri I Vorontsov, and Kip S Thorne. Quantum nondemolition measurements. *Science*, 209(4456):547–557, 1980.

[46] VB Braginsky and F Ja Khalili. Gravitational wave antenna with qnd speed meter. *Physics Letters A*, 147(5-6):251–256, 1990.

[47] Peter W Graham, David E Kaplan, Jeremy Mardon, Surjeet Rajendran, and William A Terrano. Dark matter direct detection with accelerometers. *Physical Review D*, 93(7):075029, 2016.

[48] Aaron Pierce, Keith Riles, and Yue Zhao. Searching for dark photon dark matter with gravitational-wave detectors. *Physical review letters*, 121(6):061102, 2018.

[49] Daniel Carney, Gordan Krnjaic, David C Moore, Cindy A Regal, Gadi Afek, Sunil Bhave, Benjamin Brubaker, Thomas Corbitt, Jonathan Cripe, Nicole Crisosto, et al. Mechanical quantum sensing in the search for dark matter. *Quantum Science and Technology*, 6(2):024002, 2021.

[50] Daniel Carney, Anson Hook, Zhen Liu, Jacob M Taylor, and Yue Zhao. Ultralight dark matter detection with mechanical quantum sensors. *New Journal of Physics*, 23(2):023041, 2021.

[51] Fernando Monteiro, Gadi Afek, Daniel Carney, Gordan Krnjaic, Jiaxiang Wang, and David C Moore. Search for composite dark matter with optically levitated sensors. *Physical Review Letters*, 125(18):181102, 2020.

[52] Jack Manley, Mitul Dey Chowdhury, Daniel Grin, Swati Singh, and Dalziel J Wilson. Searching for vector dark matter with an optomechanical accelerometer. *Physical review letters*, 126(6):061301, 2021.

[53] Melville S Green. Brownian motion in a gas of noninteracting molecules. *The Journal of Chemical Physics*, 19(8):1036–1046, 1951.

[54] Vladimir B Braginsky, Mikhail L Gorodetsky, Farid Ya Khalili, and Kip S Thorne. Dual-resonator speed meter for a free test mass. *Physical Review D*, 61(4):044002, 2000.

[55] Patricia Purdue and Yanbei Chen. Practical speed meter designs for quantum nondemolition gravitational-wave interferometers. *Physical Review D*, 66(12):122004, 2002.

[56] Yanbei Chen. Sagnac interferometer as a speed-meter-type, quantum-nondemolition gravitational-wave detector. *Physical Review D*, 67(12):122004, 2003.

[57] SL Danilishin. Sensitivity limitations in optical speed meter topology of gravitational-wave antennas. *Physical Review D*, 69(10):102003, 2004.

[58] Stefan L Danilishin, Eugene Knyazev, Nikita V Voronchev, Farid Ya Khalili, Christian Gräf, Sebastian Steinlechner, Jan-Simon Hennig, and Stefan Hild. A new quantum speed-meter interferometer: measuring speed to search for intermediate mass black holes. *Light: Science & Applications*, 7(1):11, 2018.

[59] Stefan L Danilishin, Farid Ya Khalili, and Haixing Miao. Advanced quantum techniques for future gravitational-wave detectors. *Living Reviews in Relativity*, 22(1):2, 2019.

[60] Christian Gräf, BW Barr, AS Bell, F Campbell, AV Cumming, SL Danilishin, NA Gordon, GD Hammond, J Hennig, EA Houston, et al. Design of a speed meter interferometer proof-of-principle experiment. *Classical and Quantum Gravity*, 31(21):215009, 2014.

[61] Kiran E Khosla, George A Brawley, Michael R Vanner, and Warwick P Bowen. Quantum optomechanics beyond the quantum coherent oscillation regime. *Optica*, 4(11):1382–1387, 2017.

[62] SF Pereira, ZY Ou, and HJ Kimble. Backaction evading measurements for quantum nondemolition detection and quantum optical tapping. *Physical review letters*, 72(2):214, 1994.

[63] Aashish A Clerk, Florian Marquardt, and K Jacobs. Back-action evasion and squeezing of a mechanical resonator using a cavity detector. *New Journal of Physics*, 10(9):095010, 2008.

[64] JB Hertzberg, T Rocheleau, T Ndukum, M Savva, Aashish A Clerk, and KC Schwab. Back-action-evading measurements of nanomechanical motion. *Nature Physics*, 6(3):213–217, 2010.

[65] MJ Woolley and AA Clerk. Two-mode back-action-evading measurements in cavity optomechanics. *Physical Review A*, 87(6):063846, 2013.

[66] Georgios Vasilakis, Heng Shen, Kasper Jensen, Misha Balabas, Daniel Salart, Bing Chen, and Eugene Simon Polzik. Generation of a squeezed state of an oscillator by stroboscopic back-action-evading measurement. *Nature Physics*, 11(5):389, 2015.

[67] JK Fremerey. Spinning rotor vacuum gauges. *Vacuum*, 32(10-11):685–690, 1982.

[68] J Patrick Looney, Joel E Harrington, Kermit C Smyth, Thomas R O'Brian, and Thomas B Lucatorto. Measurement of co pressures in the ultrahigh vacuum regime using resonance-enhanced multiphoton-ionization time-of-flight mass spectroscopy. *Journal of Vacuum Science & Technology A: Vacuum, Surfaces, and Films*, 11(6):3111–3120, 1993.

[69] Joseph T Hodges, J Patrick Looney, and Roger D van Zee. Laser bandwidth effects in quantitative cavity ring-down spectroscopy. *Applied optics*, 35(21):4112–4116, 1996.

[70] T Arpornthip, CA Sackett, and KJ Hughes. Vacuum-pressure measurement using a magneto-optical trap. *Physical Review A*, 85(3):033420, 2012.

[71] VB Makhalov, KA Martiyanov, and AV Turlapov. Primary vacuometer based on an ultracold gas in a shallow optical dipole trap. *Metrologia*, 53(6):1287, 2016.

[72] Stephen Eckel, Daniel S Barker, James A Fedchak, Nikolai N Klimov, Eric Norrgard, Julia Scherschligt, Constantinos Makrides, and Eite Tiesinga. Challenges to miniaturizing cold atom technology for deployable vacuum metrology. *Metrologia*, 55(5):S182, 2018.

[73] Mankei Tsang and Carlton M Caves. Coherent quantum-noise cancellation for optomechanical sensors. *Physical review letters*, 105(12):123601, 2010.

[74] John Melcher, Julian Stirling, Felipe Guzmán Cervantes, Jon R Pratt, and Gordon A Shaw. A self-calibrating optomechanical force sensor with femtonewton resolution. *Applied Physics Letters*, 105(23):233109, 2014.

[75] Xunnong Xu and Jacob M Taylor. Squeezing in a coupled two-mode optomechanical system for force sensing below the standard quantum limit. *Physical Review A*, 90(4):043848, 2014.

[76] Maximilian H Wimmer, Daniel Steinmeyer, Klemens Hammerer, and Michèle Heurs. Coherent cancellation of backaction noise in optomechanical force measurements. *Physical Review A*, 89(5):053836, 2014.

[77] Ali Motazedifard, F Bemani, MH Naderi, R Roknizadeh, and D Vitali. Force sensing based on coherent quantum noise cancellation in a hybrid optomechanical cavity with squeezed-vacuum injection. *New Journal of Physics*, 18(7):073040, 2016.

[78] Rouven Essig, Marivi Fernandez-Serra, Jeremy Mardon, Adrian Soto, Tomer Volansky, and Tien-Tien Yu. Direct detection of sub-gev dark matter with semiconductor targets. *Journal of High Energy Physics*, 2016(5):1–54, 2016.

[79] Katelin Schutz and Kathryn M Zurek. Detectability of light dark matter with superfluid helium. *Physical review letters*, 117(12):121302, 2016.

[80] Rouven Essig, Jeremy Mardon, Oren Slone, and Tomer Volansky. Detection of sub-gev dark matter and solar neutrinos via chemical-bond breaking. *Physical Review D*, 95(5):056011, 2017.

[81] Simon Knapen, Tongyan Lin, Matt Pyle, and Kathryn M Zurek. Detection of light dark matter with optical phonons in polar materials. *Physics Letters B*, 785:386–390, 2018.

[82] Lawrence M Krauss. Low-energy neutrino detection and precision tests of the standard model. *Physics Letters B*, 269(3-4):407–411, 1991.

[83] DN McKinsey and JM Doyle. Liquid helium and liquid neon-sensitive, low background scintillation media for the detection of low energy neutrinos. *Journal of Low Temperature Physics*, 118(3):153–165, 2000.

[84] Gianpaolo Bellini, J Benziger, D Bick, G Bonfini, D Bravo, M Buizza Avanzini, B Caccianiga, L Cadonati, Frank Calaprice, P Cavalcante, et al. Final results of borexino phase-i on low-energy solar neutrino spectroscopy. *Physical Review D*, 89(11):112007, 2014.

[85] Gioacchino Ranucci. Techniques and methods for the low-energy neutrino detection. *The European Physical Journal A*, 52(4):1–10, 2016.

[86] Vladimir B Braginsky and Braginskiĭ. *Quantum measurement*.

[87] Roberto Brunelli and T Poggiot. Template matching: Matched spatial filters and beyond. *Pattern recognition*, 30(5):751–768, 1997.

[88] MD LaHaye, Olivier Buu, Benedetta Camarota, and KC Schwab. Approaching the quantum limit of a nanomechanical resonator. *Science*, 304(5667):74–77, 2004.

[89] Xiankai Sun, Jiangjun Zheng, Menno Poot, Chee Wei Wong, and Hong X Tang. Femtogram doubly clamped nanomechanical resonators embedded in a high-q two-dimensional photonic crystal nanocavity. *Nano letters*, 12(5):2299–2305, 2012.

[90] Laure Mercier de Lépinay, Benjamin Pigeau, Benjamin Besga, Pascal Vincent, Philippe Poncharal, and Olivier Arcizet. A universal and ultrasensitive vectorial nanomechanical sensor for imaging 2d force fields. *Nature nanotechnology*, 12(2):156, 2017.

[91] Evan D Hall, Rana X Adhikari, Valery V Frolov, Holger Müller, and Maxim Pospelov. Laser interferometers as dark matter detectors. *Physical Review D*, 98(8):083019, 2018.

[92] Gordan Krnjaic and Kris Sigurdson. Big Bang Darkleosynthesis. *Phys. Lett.*, B751:464–468, 2015.

[93] Moira I. Gresham, Hou Keong Lou, and Kathryn M. Zurek. Nuclear Structure of Bound States of Asymmetric Dark Matter. *Phys. Rev.*, D96(9):096012, 2017.

[94] Ahmet Coskuner, Dorota M Grabowska, Simon Knapen, and Kathryn M Zurek. Direct detection of bound states of asymmetric dark matter. *Physical Review D*, 100(3):035025, 2019.

[95] Robert V Wagoner, Clifford M Will, and Ho Jung Paik. Tunable free-mass gravitational-wave detector. *Physical Review D*, 19(8):2325, 1979.

[96] Sohitri Ghosh, Matthew A Feldman, Seongjin Hong, Claire Marvinney, Raphael Pooser, and Jacob M Taylor. Combining quantum noise reduction resources: a practical approach. *arXiv preprint arXiv:2211.14460*, 2022.

[97] SP Vyatchanin and EA Zubova. Quantum variation measurement of a force. *Physics letters A*, 201(4):269–274, 1995.

[98] Vladimir B Braginsky, Mikhail L Gorodetsky, Farid Ya Khalili, Andrey B Matsko, Kip S Thorne, and Sergey P Vyatchanin. Noise in gravitational-wave detectors and other classical-force measurements is not influenced by test-mass quantization. *Physical Review D*, 67(8):082001, 2003.

[99] Sydney Schreppler, Nicolas Spethmann, Nathan Brahms, Thierry Botter, Maryrose Barrios, and Dan M Stamper-Kurn. Optically measuring force near the standard quantum limit. *Science*, 344(6191):1486–1489, 2014.

[100] LF Buchmann, S Schreppler, J Kohler, N Spethmann, and DM Stamper-Kurn. Complex squeezing and force measurement beyond the standard quantum limit. *Physical review letters*, 117(3):030801, 2016.

[101] Xunnong Xu and Jacob M. Taylor. Squeezing in a coupled two-mode optomechanical system for force sensing below the standard quantum limit. *Phys. Rev. A*, 90:043848, Oct 2014.

[102] RC Pooser, Nicholas Savino, Emma Batson, JL Beckey, J Garcia, and BJ Lawrie. Truncated nonlinear interferometry for quantum-enhanced atomic force microscopy. *Physical Review Letters*, 124(23):230504, 2020.

[103] Raphael C Pooser and Benjamin Lawrie. Ultrasensitive measurement of microcantilever displacement below the shot-noise limit. *Optica*, 2(5):393–399, 2015.

[104] M Tse, Haocun Yu, Nutsinee Kijbunchoo, A Fernandez-Galiana, P Dupej, L Barsotti, CD Blair, DD Brown, SE Dwyer, A Effler, et al. Quantum-enhanced Advanced LIGO detectors in the era of gravitational-wave astronomy. *Physical Review Letters*, 123(23):231107, 2019.

[105] Chang-Woo Lee, Jae Hoon Lee, and Hyojun Seok. Squeezed-light-driven force detection with an optomechanical cavity in a Mach–Zehnder interferometer. *Scientific Reports*, 10(1):1–16, 2020.

[106] Philippe Grangier, Juan Ariel Levenson, and Jean-Philippe Poizat. Quantum non-demolition measurements in optics. *Nature*, 396(6711):537–542, 1998.

[107] MD Levenson, RM Shelby, M Reid, and DF Walls. Quantum nondemolition detection of optical quadrature amplitudes. *Physical review letters*, 57(20):2473, 1986.

[108] A La Porta, RE Slusher, and B Yurke. Back-action evading measurements of an optical field using parametric down conversion. *Physical review letters*, 62(1):28, 1989.

[109] MR Vanner, J Hofer, GD Cole, and M Aspelmeyer. Cooling-by-measurement and mechanical state tomography via pulsed optomechanics. *Nature communications*, 4(1):1–8, 2013.

[110] Itay Shomroni, Liu Qiu, Daniel Malz, Andreas Nunnenkamp, and Tobias J Kippenberg. Optical backaction-evading measurement of a mechanical oscillator. *Nature communications*, 10(1):1–7, 2019.

[111] Yulong Liu, Jingwei Zhou, Laure Mercier de Lépinay, and Mika A Sillanpää. Quantum backaction evading measurements of a silicon nitride membrane resonator. *arXiv preprint arXiv:2201.11041*, 2022.

[112] Sergey P Vyatchanin and Andrey B Matsko. Broadband quantum back action evading measurements of a resonant force. *Physics Letters A*, 424:127849, 2022.

[113] Jonathan Cripe, Torrey Cullen, Yanbei Chen, Paula Heu, David Follman, Garrett D Cole, and Thomas Corbitt. Quantum backaction cancellation in the audio band. *Physical Review X*, 10(3):031065, 2020.

[114] Min Jet Yap, Jonathan Cripe, Georgia L Mansell, Terry G McRae, Robert L Ward, Bram JJ Slagmolen, Paula Heu, David Follman, Garrett D Cole, Thomas Corbitt, et al. Broadband reduction of quantum radiation pressure noise via squeezed light injection. *Nature Photonics*, 14(1):19–23, 2020.

[115] Chuming Wang, Chunnong Zhao, Xiang Li, Enping Zhou, Haixing Miao, Yanbei Chen, and Yiqiu Ma. Boosting the sensitivity of high frequency gravitational wave detectors by pt-symmetry. *arXiv preprint arXiv:2206.13224*, 2022.

[116] Xiang Li, Maxim Goryachev, Yiqiu Ma, Michael E Tobar, Chunnong Zhao, Rana X Adhikari, and Yanbei Chen. Broadband sensitivity improvement via coherent quantum feedback with pt symmetry. *arXiv preprint arXiv:2012.00836*, 2020.

[117] Tuvia Gefen, Rajashik Tarafder, Rana X Adhikari, and Yanbei Chen. Quantum precision limits of displacement noise free interferometers. *arXiv preprint arXiv:2209.02998*, 2022.

[118] Huaixiu Zheng, Matti Silveri, RT Brierley, SM Girvin, and KW Lehnert. Accelerating dark-matter axion searches with quantum measurement technology. *arXiv preprint arXiv:1607.02529*, 2016.

[119] M Malnou, DA Palken, BM Brubaker, Leila R Vale, Gene C Hilton, and KW Lehnert. Squeezed vacuum used to accelerate the search for a weak classical signal. *Physical Review X*, 9(2):021023, 2019.

[120] Akash V Dixit, Srivatsan Chakram, Kevin He, Ankur Agrawal, Ravi K Naik, David I Schuster, and Aaron Chou. Searching for dark matter with a superconducting qubit. *Physical review letters*, 126(14):141302, 2021.

[121] Anthony J Brady, Christina Gao, Roni Harnik, Zhen Liu, Zheshen Zhang, and Quntao Zhuang. Entangled sensor-networks for dark-matter searches. *arXiv preprint arXiv:2203.05375*, 2022.

[122] Rodney Loudon and Peter L Knight. Squeezed light. *Journal of modern optics*, 34(6-7):709–759, 1987.

[123] Florent Lecocq, Jeremy B Clark, Raymond W Simmonds, Jose Aumentado, and John D Teufel. Mechanically mediated microwave frequency conversion in the quantum regime. *Physical review letters*, 116(4):043601, 2016.

[124] TA Palomaki, JW Harlow, JD Teufel, RW Simmonds, and Konrad W Lehnert. Coherent state transfer between itinerant microwave fields and a mechanical oscillator. *Nature*, 495(7440):210–214, 2013.

[125] John D Teufel, Tobias Donner, Dale Li, Jennifer W Harlow, MS Allman, Katarina Cicak, Adam J Sirois, Jed D Whittaker, Konrad W Lehnert, and Raymond W Simmonds. Sideband cooling of micromechanical motion to the quantum ground state. *Nature*, 475(7356):359–363, 2011.

[126] CA Regal, JD Teufel, and KW Lehnert. Measuring nanomechanical motion with a microwave cavity interferometer. *Nature Physics*, 4(7):555–560, 2008.

[127] Emil Zeuthen, Albert Schliesser, Jacob M Taylor, and Anders S Sørensen. Electrooptomechanical equivalent circuits for quantum transduction. *Physical Review Applied*, 10(4):044036, 2018.

[128] M. H. Devoret. Quantum Fluctuations in Electrical Circuits. In S. Reynaud, E. Giacobino, and J. Zinn-Justin, editors, *Quantum Fluctuations (Les Houches Session LXIII)*, pages 351–386. Elsevier, January 1997.

[129] X. Ma, J. J. Viennot, S. Kotler, J. D. Teufel, and K. W. Lehnert. Non-classical energy squeezing of a macroscopic mechanical oscillator. *Nature Physics*, 17(3):322–326, Mar 2021.

[130] Joachim Hofer, Gerard Higgins, Hans Huebl, Oliver F. Kieler, Reinhold Kleiner, Dieter Koelle, Philip Schmidt, Joshua A. Slater, Michael Trupke, Kevin Uhl, Thomas Weimann, Witlef Wieczorek, Friedrich Wulschner, and Markus Aspelmeyer. High-q magnetic levitation and control of superconducting microspheres at millikelvin temperatures, 2022.

[131] Warwick P. Bowen and G. J. Milburn. *Quantum Optomechanics*. CRC Press, Taylor & Francis Group, Boca Raton. FL, 2016.

[132] A. A. Clerk, M. H. Devoret, S. M. Girvin, Florian Marquardt, and R. J. Schoelkopf. Introduction to quantum noise, measurement, and amplification. *Rev. Mod. Phys.*, 82:1155–1208, Apr 2010.

[133] Markus Aspelmeyer, Tobias J. Kippenberg, and Florian Marquardt. Cavity optomechanics. *Rev. Mod. Phys.*, 86:1391–1452, Dec 2014.

[134] C. W. Gardiner and M. J. Collett. Input and output in damped quantum systems: Quantum stochastic differential equations and the master equation. *Phys. Rev. A*, 31:3761–3774, Jun 1985.

[135] Sohitri Ghosh, Daniel Carney, Peter Shawhan, and Jacob M. Taylor. Backaction-evading impulse measurement with mechanical quantum sensors. *Phys. Rev. A*, 102:023525, Aug 2020.